

Lithium Niobate-based High-Electromechanical-Coupling RF-MicroElectroMechanical Resonators for Wideband Filtering

Submitted in partial fulfillment of the requirements for the
Degree of Doctor of Philosophy

in
Electrical and Computer Engineering

Lisha Shi

B.S., Electrical Engineering, Politecnico di Torino

M.S., Electrical Engineering, University of Pennsylvania

Carnegie Mellon University
Pittsburgh, PA

February, 2016

Acknowledgement

First and foremost I would like to express my utmost and sincere gratitude to my advisor, mentor and friend Prof. Gianluca Piazza who professionally guided me and taught me his technical and managerial skills, showing me a brilliant example of what a dynamic and truly innovative engineer and professor should be. I am ever affected by his great passion about MEMS and inspired by the altitude he shows for research. I am very grateful to Professors Gary Fedder, Tamal Mukherjee and Dr. Kushal Bhattacharjee who served as members of my dissertation committee and offered very valuable technical and professional feedbacks. I also wish to thank Professor Jimmy Zhu and Professor Yi Luo who offered invaluable advice for my life and career.

I would like to thank my colleagues in the Piazza Micro and Nano Systems (PMaNS) Lab. I am particularly grateful to my friend Augusto Tazzoli, for all the encouragement and help provided. I also fondly acknowledge Nai Kuei-Kuo, Cristian Cassella, Chengjie Zuo, Chiara Zuniga, Matteo Rinaldi, Jeronimo Segovia, Enes Calayır and Mohamed Mahmoud for the times we spent at work and at play.

I also extend my sincere thanks to my friends Eric Guo and Pengfei Li with whom I have shared the living experience in the United States and continue to share the passion for career.

I am obliged to my family: my dearest mother and father who always supported me, offered invaluable help and advice in facing professional and personal issues and to whom I owe most of what I am today. Thank you all for a lifetime of loving support.

This work was supported by National Science Foundation (NSF) and Defense Advanced Research Projects Agency (DARPA) under Radio Frequency- Field Programmable Gate Array (RF-FPGA) programs. I also offer special thanks to Dr. Matthew Moneck, Suresh Santhanam, Norman Gottron and Gregory Slovin for their assistance with fabrication and tool installation and the rest of the Carnegie Mellon University Nanofabrication Laboratory staff for their support.

Dedication

— *to my parents.*

Abstract

The demand for highly-integrated analog filtering and frequency reference elements has spurred rapid innovation in the area of vibrating radio frequency (RF) MEMS. To date, however, no single technology has emerged that can simultaneously deliver monolithic, CMOS-compatible integration of intermediate frequency (IF) and RF components that can readily interface with 50 Ω , enable multi-frequency per single chip, permit the synthesis of reconfigurable receivers capable of adapting their frequencies and bandwidths to variations in the spectrum, and possess good temperature stability (first order Temperature coefficient of frequency(TCF) controlled to be within ± 20 ppm/ $^{\circ}\text{C}$).

This dissertation presents analytical and experimental results on a new class of piezoelectric devices based on monolithic piezoelectric thin-film Lithium Niobate (LN) contour mode plate resonators. The high quality factor (Q) and electromechanical coupling coefficient (k_t^2) (conversion of electrical into mechanical energy expected to exceed 20% and 10 % respectively for standalone LN and LN/SiO₂ laterally vibrating resonators (LVRs) of the new LN resonator geometry will permit to expand the range of applicability of static acoustic filtering solutions, enabling the deployment of reconfigurable wide band (fractional bandwidth greater than 4%) filters that are not possible to date.

Three separate process flows for fabricating standalone LN and LN/SiO₂ LVRs microstructures were developed at Carnegie Mellon University for the first time. Fabrication has evolved from single die processing to 4" wafer processing to improve the fabrication accuracy and efficiency. All developed processes are low temperature ($T_{\text{MAX}} < 400$ $^{\circ}\text{C}$) and use standard CMOS-based fabrication steps, therefore offering the option for a heterogeneous integration with CMOS electronics.

Further efforts have been put into device design for improving the performance of LN LVRs in terms of k_t^2 , Q and spurious mode suppression as well as robustness to process variations. In this work, LN substrate orientation, metal coverage of the resonator fingers and the resonator edges have been explored and designed to achieve maximum k_t^2 . 2D FEM (Finite Element Method) has been implemented

to guide the design and verify the effect of these efforts for k_t^2 enhancement. We also firstly investigated some of the main sources of damping that set the Q of LN and LN on SiO₂ LVRs. In the Very High Frequency (VHF) range, our experiments confirm that Q is mainly affected (at ambient conditions) by anchor losses (Q_{anc}) and an additional damping mechanism of thermodynamic nature likely related to thermoelastic dissipation (TED) (Q_{ted}). In the case of anchor losses, perfectly matched layer (PML) technique has been employed to accurately predict Q_{anc} . For the first time, a systematic analysis of the resonator geometry (including anchor width and length, metalized bus width, gap width and effective finger length) has been explored and optimized to obtain maximum Q for LN LVR at 500 MHz. Besides, due to the high k_t^2 of LN, it is extremely complicated to control the various modes of vibration and ensure that a single mode is excited. In order to effectively confine energy in a single mode, 3D device dimension and boundaries have been varied for the purpose of suppressing spurious modes.

Finally, in order to address the issue of a large negative TCF value associated with LN, generally in the order of -80 ppm/°C, a technology platform formed by LN on SiO₂ suspended membranes has been developed to engineer the TCF of the high electromechanical coupling resonators. For the first time, analysis of the temperature coefficient of frequency (TCF) for the main acoustic mode excited in ion-sliced LN thin films integrated with and without a SiO₂ layer for temperature compensation has been demonstrated. Although the device demonstration was not done on optimized geometries, the measured TCF for LN of X-cut (0.5 μ m) on SiO₂ (0.8 μ m) devices operating in the main S0 mode around 510.47 MHz and 449.16 MHz orientated at +30° to the +z axis and at -60° to the +z axis exhibit TCFs of -3.9 ppm/°C and -4.68 ppm/°C, drastically reduced with respect to the uncompensated case.

Table of Contents

Acknowledgement.....	2
1. Introduction.....	9
1.1 Outline of Dissertation.....	10
2. Background	12
2.1 Principle of Operation of Piezoelectric Resonators in LN.....	12
2.1.1 Device modeling	16
2.1.2 Modeling of electromechanical coupling for different LN Cuts.....	18
3. Development of micromachining process for LN Resonant MEMS	24
3.1 Substrate selection & technology development	26
3.2 1st generation standalone LN and LN/SiO ₂ LVRs	32
3.3 2nd generation LN alone LVRs	37
3.4 3rd generation LN alone LVRs	43
4. Design of high k_t^2 LN LVRs	46
4.1 Active reflectors for high performance LN LVRs.....	47
4.2 Electrode coverage optimization in terms of k_t^2	51
4.3 Experimental Results	52
5. Investigation of Q in LN LVRs	55
5.1 Background work.....	57
5.2 Anchor loss	60
5.2.1 Analysis and 3D FEM simulations	61

5.2.2	Analysis of anchor losses as a function of resonator geometry.....	63
5.2.3	Non-ideality	77
5.3	Design of experiment and experimental verification of impact of resonator geometry on Q.....	80
5.3.1	Experimental results.....	88
6.	Spurious mode suppression and robustness to processing.....	101
6.1	Active reflectors for high performance LN LVRs.....	101
6.2	Experimental Results.....	104
6.2.1	Fully covered active reflector design.....	104
7.	Engineering the Temperature Coefficient of Frequency (TCF) of high electromechanical coupling LN LVRs.....	109
7.1	Definition and analytical model.....	109
7.2	2D FEM modeling	111
7.3	Design of TCF compensated LN LVRs	114
7.4	Experimental results	115
7.4.1	Characterization of electromechanical coupling (k_t^2) and quality factor (Q) ...	117
7.4.2	TCF from measurement.....	119
7.4.3	Non-linearity analysis and TCF extraction from non-linear model.....	123
8.	Conclusions.....	126
8.1	Summary.....	126
8.2	Future Research Directions.....	127

Appendix A: Lithium Niobate piezoelectric matrices of different in-plane-orientations and cuts MATLAB computation code.....	129
Appendix B: Lithium Niobate laterally vibrating resonator MATLAB fitting code.....	131
Appendix C: Lithium Niobate Laterally Vibrating Resonator Fabrication Process.....	135
REFERENCES:	143

1. Introduction

The rapidly growing demand for multi-functional wireless communication systems is driving the development of monolithic frequency-agile RF front-ends. The envisioned RF transceivers require miniature filtering modules that can cover the current commercial operating bands and potentially offer adaptation to future standards. Therefore, research activities on high frequency MEMS resonators have focused on the development of devices for programmable RF front-ends with a particular attention to reconfigurable filters [1-3].

Acoustic resonators and filters, such as surface acoustic wave (SAW) devices and thin film bulk acoustic resonators (FBARs), are used extensively in commercial wireless communications as well as military radios, satellite communications, and millimeter wave circuits. SAW devices have been widely used in IF and RF filters in wireless transmission systems for several decades and offer the advantage of small size, low cost, capability of having multiple frequencies on the single substrate and low TCF (after passive compensation). However, there are severe limitations to SAW devices. The obtained Q is lower compared to the counterpart of FBAR because of the unavoidable energy loss into the substrate. Moreover, they can hardly achieve frequencies above 2.5 GHz. SAW phase velocities of common piezoelectric substrates, such as quartz, LiNbO_3 (LN), and LiTaO_3 (LT), are below 4,000 m/s. As the operational frequency goes up, the dimension of the IDT fingers feasibly shrink to sub-micron dimensions which renders not economically viable the use of high-end lithography equipment for the making of these devices. Besides, even when the frequency approaches 2GHz, the shrinkage of the IDT comb-fingers makes SAW resonators vulnerable to electrostatic discharge. Besides, the k_t^2 of common SAW devices are well below 10%. FBARs, on the other hand, have been widely implemented in RF filters for 4G and LTE frequency bands by achieving high k_t^2 (approaching 7%) and Q on silicon substrates fulfilling many wireless communication standards. Nonetheless, they cannot attain multiple frequencies on a single chip.

The AlN Contour-Mode Resonators (CMRs) [1] previously demonstrated by our research group have shown applicability up to 10 GHz and have introduced a paradigm shift over prior resonator technology because of the ability to devise multi-frequency filters and oscillators on the same substrate. However, they are limited by the moderate material electromechanical coupling, k_t^2 ($\sim 2\%$ in AlN), to operate in systems that require fractional BWs $< 3\%$. These devices also exhibit an uncompensated first order TCF of about -28 ppm/ $^{\circ}\text{C}$, which is not adequate for accurate timing or frequency reference applications. The use of SiO_2 in the AlN CMR stack [2] [3] has achieved a low first-order TCF, but the moderate k_t^2 limits the applicability of these devices to narrowband systems and requires higher power consumption in oscillators [4].

Besides, these components are all static and do not yet permit the synthesis of reconfigurable receivers capable of adapting their frequencies and bandwidths to variations in the available spectrum. The need to meet the requirements dictated by wireless standards and simultaneously achieve reconfiguration has, therefore, pushed researchers to look at devices and materials with higher electromechanical coupling, k_t^2 . In particular, a high electromechanical coupling coefficient (k_t^2) is an essential characteristic of the resonator as only values of k_t^2 above 10% would enable tuning and reconfiguration through external electromagnetic components when used for existing wireless standards.

1.1 Outline of Dissertation

The overarching theme of this dissertation is the development of a new class of Lithium Niobate (LN) laterally vibrating resonators (LVRs) with high k_t^2 , Q and low first order TCF (controlled to be within ± 20 ppm/ $^{\circ}\text{C}$) and capability of having multi-frequencies on the same substrate.

Ever since the development of the first generation of LN LVRs [5], the primary challenges faced in the realization and application of these devices have been the delicate and low-yield microfabrication process, poor quality factors (Q), the presence of spurious modes of vibration, significant performance dependence on process variations (misalignment and over/under-etching), and large TCF. However, these

issues are not insurmountable and this dissertation charts a clear path on how to address them. In summary, the main contributions made by this dissertation work are:

- Development of methods of micro-machining LN and process flow engineered for the making of LN and LN/SiO₂ LVRs.
- Device design optimization to improve the k_t^2 of LN LVRs
- Investigation of various sources of damping in LN LVRs and device design optimization to improve the Q of LN LVRs
- Device design optimization to improve spurious mode suppression, and robustness to process variations of LN LVRs.
- Analysis of the temperature coefficient of frequency and modeling of the device TCF and electromechanical coupling for the main acoustic mode excited in ion-sliced LN thin films integrated with a SiO₂ layer for temperature compensation.

These contributions will be of some scientific interest, such as the study of what impacts Q in these resonators. However, the major benefit of this work will be in enabling a new class of piezoelectric devices and especially an RF filtering platform with reconfigurability. The high Q and electromechanical coupling coefficient (conversion of electrical into mechanical energy expected to exceed 20% and 10 % respectively for standalone LN and LN/SiO₂ LVRs) of the new LN resonator geometry will permit to expand the range of applicability of static acoustic filtering solutions, enabling the deployment of reconfigurable wide band (fractional bandwidth greater than 4%) filters that are not possible to date.

2. Background

2.1 Principle of Operation of Piezoelectric Resonators in LN

Piezoelectricity is a physical phenomenon that was discovered in 1880 by the Curie brothers. The physical origin of piezoelectricity comes from the charge asymmetry within the primitive unit cell of a material which results in the formation of a net electric dipole. When an external mechanical stress is applied to a piezoelectric crystal, electric charge accumulates in response. The converse effect, whereby a piezoelectric crystal becomes strained when an electric field is applied to it, also exists and shows the reversibility of such phenomenon.

Depending on what kind of independent variables are chosen (stress or strain; electric field or electric displacement) the fundamental equations of piezoelectricity relating mechanical and electrical variables can be described, for example, using the IEEE standard notation (ANSI/IEEE Std 176-1987) by the material's constitutive equations as the following:

$$\begin{aligned} \mathbf{T} &= \mathbf{c}\mathbf{S} - \mathbf{e}^T \mathbf{E} \\ \mathbf{D} &= \boldsymbol{\varepsilon} \mathbf{E} + \mathbf{e} \mathbf{S} \end{aligned} \quad (2.1)$$

where \mathbf{T} represents piezoelectric material's stress (6 by 1 matrix), \mathbf{S} strain (6 by 1 matrix), \mathbf{D} electric displacement (3 by 1 matrix), \mathbf{E} electric field (3 by 1 matrix), \mathbf{c} represents the stiffness matrix (6 by 6 matrix), \mathbf{e} piezoelectric stress matrix (6 by 3 matrix), \mathbf{e}^T the transpose of the piezoelectric matrix and $\boldsymbol{\varepsilon}$ the permittivity matrix (3 by 3 matrix).

Equation (2.1) is known as the e-form and renders in a matrix form the complex description of piezoelectricity. The e-form is widely used because more suitable to solve problems that involve the dynamics of elastic bodies and will be used and referenced throughout this dissertation. The values of coefficient of stiffness matrix (\mathbf{c}), piezoelectric stress (\mathbf{e}) matrix, 1st order temperature dependence of stiffness matrix, dielectric matrix, thermal expansion matrix and density of the Z-cut LN and SiO₂ used in calculation in this dissertation are listed in Table 1.1.

Table.2. 1. Material properties of lithium niobate and silicon dioxide used in the simulation

Quantity	LiNbO ₃ [6][7]	SiO ₂ (thermally grown)[8]
Stiffness coefficients[10 ¹¹ N/m ²]		
c_{11}^E	1.9886	0.785
c_{12}^E	0.5467	0.161
c_{13}^E	0.6799	0.161
c_{33}^E	0.0783	-
c_{44}^E	2.3418	0.785
c_{66}^E	0.0783	0.312
	0.7209	0.312
1st order temperature dependence of stiffness coefficient[10 ⁻⁶ /K]		
Tc_{11}^E	-174	239
Tc_{12}^E	-252	584
Tc_{13}^E	-159	584
Tc_{14}^E	-214	-
Tc_{33}^E	-153	239
Tc_{44}^E	-203	151
Tc_{66}^E	-143	151
Piezoelectric stress coefficients[C/m]		
e_{15}	3.83	
e_{16}	3.83	
e_{22}	2.37	
e_{24}	3.83	
e_{31}	0.23	
e_{33}	1.8	
Dielectric coefficients		
ϵ_{11}^s	45	3.9
ϵ_{33}^s	26.2	3.9
Thermal expansion coefficients [10 ⁻⁶ /K]		
α_{11}	14.4	0.5
α_{22}	15.9	0.5
α_{33}	7.5	0.5
Density(kg/m ³)		
ρ	4640	2200

Another very effective way of describing the piezoelectric phenomenon into equations (in strain-charge form) is:

$$\mathbf{S} = \mathbf{s}\mathbf{T} + \mathbf{d}\mathbf{E}$$

$$\mathbf{D} = \mathbf{d}^T\mathbf{T} + \epsilon\mathbf{E} \quad (2.2)$$

This equation is known as the d-form, being now \mathbf{d} the piezoelectric matrix (6 by 3 matrix), \mathbf{d}^T the transpose of piezoelectric matrix and \mathbf{s} the compliance matrix.

According to crystallographic classification, LN belongs to the point group 3m and the values of the coefficients in the d-matrix are dependent on the particular cut. Generally, they are reported for Z-cut at 20° C as:

$$d_{ij} = \begin{bmatrix} 0 & 0 & 0 & 0 & 74.27 & -21.14 \\ -21.14 & 21.14 & 0 & 74.27 & 0 & 0 \\ -0.87 & -0.87 & 16.29 & 0 & 0 & 0 \end{bmatrix} [pC/N]$$

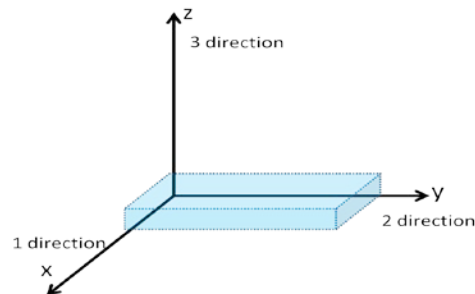
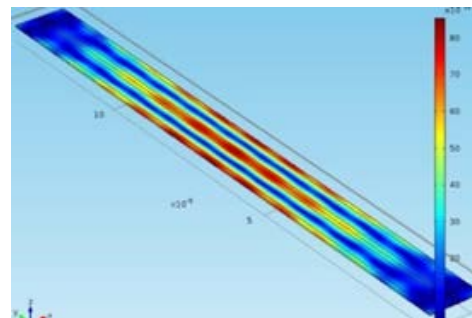
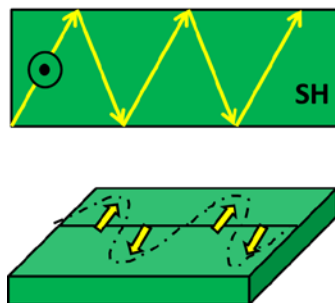


Fig.2.1 Schematic representation of the thin film in LN. The main x (1), y (2) and z (3) directions are indicated.



(a)

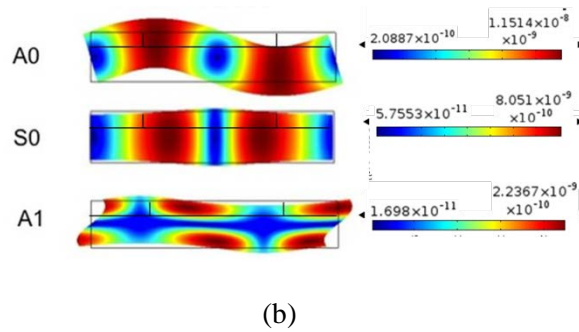


Fig.2. 2. (a) Schematic views and 3D displacement view of SH0 mode and (b) 2D displacement view of A0, S0 and A1 mode

The discussion presented so far is valid for bulk crystals, but can be extended directly to single crystalline LN thin-film technology. According to piezoelectricity relation, an elastic body could be excited in thickness modes with d_{33} coefficient, shear modes with d_{15} coefficient and in contour modes with d_{31} (thickness field excitation, TFE) and d_{11} (lateral field excitation, LFE) coefficient. We target to excite high frequency modes with high electromechanical coupling (k_t^2) and be capable of devising multiple frequencies on the same chip. Hence, we need to firstly identify a vibration mode satisfying these specifications and then optimize the k_t^2 of target mode by choosing the cut and in-plane orientation of the LN film.

Thickness mode is currently exploited in FBAR resonators with AlN film. The film thickness sets the resonance frequency of the structure and therefore we can only achieve one single frequency per wafer. Of course, various etching methods may be used to vary the frequencies of the FBARs, but this approach is slow and uneconomical. Two promising candidates considered for LN films are shear modes (SH0) (Fig.2.2 (a)) and contour modes (S0 mode) (Fig.2.2 (b)) due to their intrinsic high coupling and limited dispersion with wavelength (hence enabling multiple frequencies on the same substrate).

Shear modes are generally difficult to excite in thin-film technology, such as AlN, because they require placing the electrodes in an odd configuration to apply sufficient electric field in 1(x) direction or have electrodes directly in the 1 direction. However, it was enabled for LN thanks to the availability of

different wafer cuts and the use of an advanced fabrication technology that is based on layer transfer of single crystalline substrates.

Contour modes, previously demonstrated by our group are the mode of interest because high k_t^2 up to 20 % and Q up to 2000 have been reported for the LVRs built with X-cut LN indicating the possibility of building reconfigurable filters. Besides, the phase velocity of S0 is much larger (1.5x) than that of SH0 mode, hence favoring the use of S0 modes for high frequency applications. Thus, the work described in this dissertation focuses on LN resonators vibrating in the S0 mode.

Different cuts of LN have been explored to maximize the coupling of S0 mode so as to maximize the lateral strain through application of electric fields oriented either across the thickness or the lateral dimensions of the films. The electric fields can be applied along different directions by means of interdigitated electrodes and thanks to the availability of different wafer cuts and the use of smart cut technique [9]. Based on the results of k_t^2 modeling for different wafer cuts, both X and Y-cut LN are selected for the development and study of LN LVRs (see 3.1.1 for details). .

Fig.2.2 shows the displacement fields of different Lamb wave modes observed from COMSOL simulated frequency response of X-cut LN LVRs. The fundamental symmetric mode referred to as contour mode (S0 mode), antisymmetric mode referred to as flexural mode (A0 mode), higher order antisymmetric mode (A1 mode) and shear mode (SH0 mode) appear in the response. Among all these modes, SH0 and S0 mode are recorded and studied due to their intrinsic high electromechanical coupling.

2.1.1 Device modeling

To excite contour modes of vibration in LN, two excitation methods can be utilized, one being lateral field excitation (LFE), the other method being thickness field excitation (TFE) (Fig2.3). LFE consists of suspended plates covered on the top surface by metal interdigital fingers. Electric field is induced by the interdigital fingers that are alternatively connected to ground and signal on the top surface and excites lateral expansion and compression in adjacent fingers (mode known as S0 lamb wave) mainly

through the equivalent d_{11} piezoelectric coefficient re-defined for the selected oriented LN crystal (so as to generate the lateral strain through application of electric fields oriented across the lateral dimensions of the films). TFE is implemented by sandwiching suspended plates between two patterned metal layers that are employed to create an electric field across the thickness of the piezoelectric film (h). The electric field applied in the thickness direction generates S0 mode of vibration in the LN plate mainly through the equivalent d_{31} piezoelectric coefficient re-defined for the selected oriented LN crystal (so as to generate the lateral strain through application of electric fields oriented across the thickness of the films.). Note that the equivalent d_{ij} coefficients are defined in the dissertation for X-cut LN and Y-cut LN substrate placed in Cartesian coordinates respectively and the mapping of the corresponding axes in 1,2,3 directions from X and Y-cut crystal to original axes defined for Z-cut crystal are listed in table 2.2.

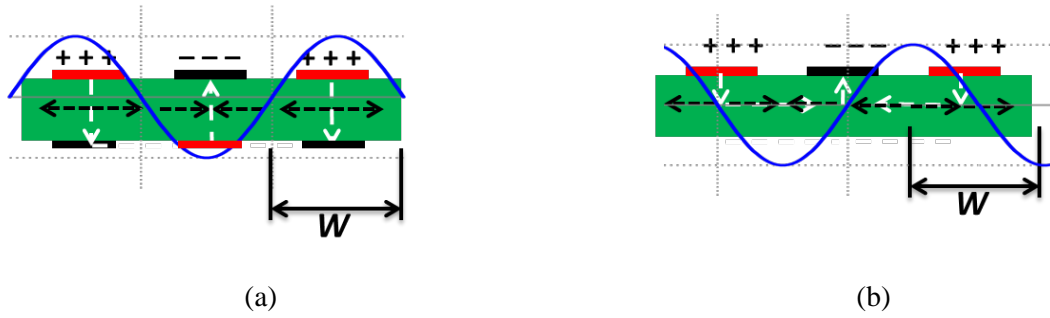


Fig.2. 3. Block view of (a) thickness field excitation and (b) lateral field excitation. White arrows represents the electric field and black arrow the lateral displacement. Blue sinewave represents the strain.

Table.2. 2. Axis mapping from X and Y-cut crystal to Z-cut crystal in Cartesian coordinates

	Z-cut	Y-cut	X-cut
1 direction	X	Z	Y
2 direction	Y	X	Z
3 direction	Z	Y	X

The mechanical resonance of such a device is set by the lateral dimension of the excitation electrode and can be formulated as,

$$f = \frac{1}{\lambda} \sqrt{\frac{E_p}{\rho}} = \frac{1}{2w} \sqrt{\frac{E_p}{\rho}} \quad (2.3)$$

where w is the pitch of the IDTs, E_p the equivalent Young's modulus, and ρ the equivalent mass density of the resonator stack. Therefore, multiple frequency devices can be demonstrated on the same substrate.

The resonator equivalent electrical circuit is described by the Modified Butterworth-Van Dyke (MBVD) model (Fig.3). The values of the motional parameters of the MBVD model are given by the following expressions [1]:

$$R_m = \frac{\pi^2}{8} \frac{1}{\omega_s C_0} \frac{1}{k_t^2 Q} \quad (2.4)$$

$$L_m = \frac{\pi^2}{8} \frac{1}{\omega_s^2 C_0} \frac{1}{k_t^2} \quad (2.5)$$

$$C_m = \frac{8}{\pi^2} C_0 k_t^2 \quad (2.6)$$

where C_0 (static capacitance) is a function of finger pitch (w), length (L), and spacing between electrodes (w_s). k_t^2 refers to the effective electromechanical coupling, and Q is the quality factor of the series resonance frequency. In Figure 4, R_s and R_o represent parasitic series and parallel resistances coming from the electrodes and the LN film.

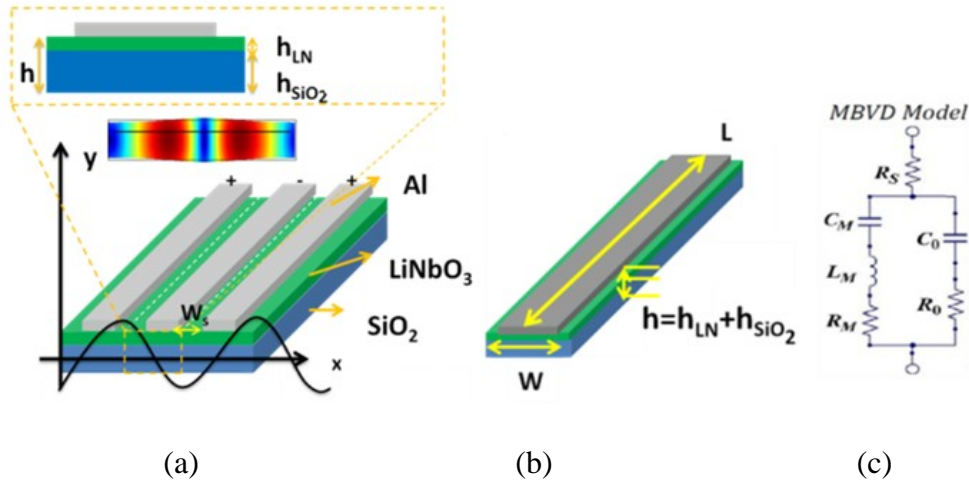


Fig.2. 4. (a) Mock-up view of the LN on SiO₂ LVR. At the top, a zoomed in view of the cross section of one finger and the SO mode of vibration of a full wavelength (2 fingers) are shown. (b) a 3D representation of single finger with its characteristic dimensions is also shown. (c) The equivalent MBVD model of the resonator.

2.1.2 Modeling of electromechanical coupling for different LN Cuts

The electromechanical coupling is directly related to the piezoelectric material properties. Depending on different communities and different applications, different definitions/evaluation of electromechanical coupling are given and listed in Table 2.3. Note that it is hard to apply the definition of

quasi-static k_t^2 to a vibrating plate as it will depend on the specific geometry, mode of vibration and frequency. For small values of k_t^2 ($< 10\%$), various definitions coincide, while as k_t^2 value increases, discrepancies occur and K_t^2 can be readily estimated by $k_t^2/(1 - k_t^2)$. In this dissertation, among the various definitions, definition#1 is employed in COMSOL 2D and 3D frequency response simulation to quickly estimate the impact of device design on the electromechanical coupling, definition#4 is used in numerical fitting of measured device response and definition#5 is utilized in COMSOL Eigen frequency simulation to reveal the impact of LN crystalline orientations on electromechanical coupling.

Table.2. 3. Definitions of Electromechanical Coupling

#	Definition of electromechanical coupling	Annotation
1	$k_{eff}^2 = \frac{(f_p^2 - f_s^2)}{f_p^2}$	As defined by IEEE Standard 176-1987. Extracted by measuring series, f_s , and parallel resonance, f_p . Does not directly describe resonator parameters, but relates to filter BW
2	$k_t^2 = \frac{\text{Output Mechanical Energy}}{\text{Input Electrical Energy}}$	Quasi-static definition of electromechanical coupling
3	$k_t^2 = \frac{\pi f_s}{2 f_p} \tan \frac{\pi \Delta f}{2 f_p}$	As defined by IEEE Standard 176-1987. Extracted by measuring series, f_s , and parallel resonance, f_p .
4	$K_t^2 = \frac{\pi^2 C_m}{8 C_o}$	As defined by the acoustic community [10]. Extracted by fitting series and parallel capacitance. Directly affects equivalent parameters of a resonator. This is related to the Γ discussed in the IEEE Standard 176-1987. It is approximately equivalent to $k_t^2/(1 - k_t^2)$. It better relates to the quasi-static definition.
5	$K^2 \sim K_t^2$	As defined in the acoustic community [11] for a longitudinal wave. It can be calculated via FEM in COMSOL by extracting the difference in phase velocity of a plate with open and shorted top surface.

In the case of definition#5, the electromechanical coupling is directly related to the piezoelectric material properties:

$$K_{ij}^2 \propto \frac{e_{ij}^2}{\epsilon_{ij} C_{ij}} \quad (2.7)$$

where the indices i and j refer to the direction along which the electric field is applied and the corresponding direction of motion, respectively; e_{ij} is the corresponding piezoelectric coefficient; C_{ij} is the corresponding compliance value; and ϵ_{ij} is the relative permittivity associated with the particular mode of

vibration. The K_{ij}^2 of LN devices vibrating in the S0 mode can be readily estimated by comparing the phase velocities of the same acoustic mode in a thin LN plate with and without metalized boundary conditions on the top surface [12]. This estimation method is valid as long as the plate thickness h is smaller than the wavelength λ , which is the case for all the resonator designs in this dissertation.

As reported in [13], computation data for various LN wafer cuts and different in-plane orientations (see Fig.2.5) suggested that maximum coupling ($K^2 \sim 30\%$) for the S0 mode is achieved via X-cut LN with an in plane CW rotation of 60° with respect to Z axis. A secondary maximum coupling for the S0 mode is achieved via Y-cut LN ($K^2 \sim 14\%$) with an in plane CW and CCW rotation of 50° with respect to Z axis, both for small h/λ ratios (h =film thickness, λ = acoustic wavelength). While maximum coupling ($K^2 \sim 38\%$) for the SH0 mode is achieved via X-cut LN with an in plane CCW rotation of 80° with respect to Z axis (170° with respect to Y axis) (See Fig.2.6). A secondary maximum coupling for the SH0 mode is achieved via Y-cut LN ($K^2 \sim 35\%$) with the wave propagating along X axis, both for small h/λ ratios (h =film thickness, λ = acoustic wavelength).

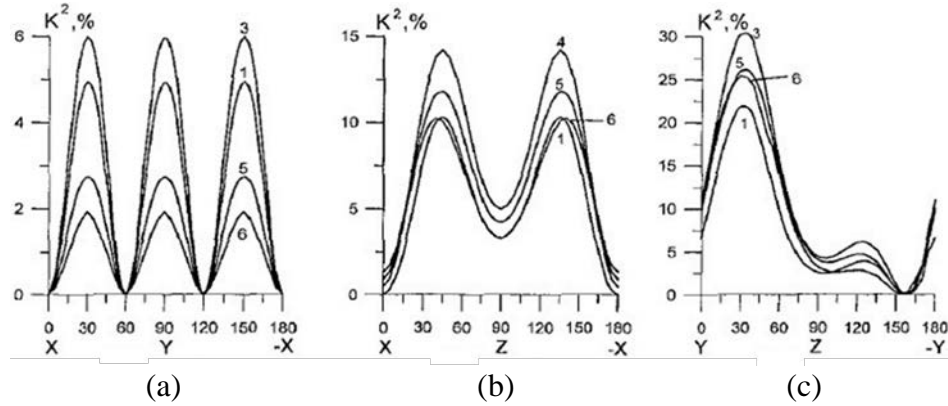


Fig.2. 5. Simulated K^2 for various cut of LN vs. wave propagation direction from [13]. h is the thickness of LN thin film, and λ is the acoustic wavelength. (a) K^2 of S0 mode for Z-cut. (b) K^2 of S0 mode for Y-cut. (c) K^2 of S0 mode for X-cut. $h/\lambda = 1$) 0.01, 2) 0.025, 3) 0.05, 4) 0.1, 5) 0.25, 6) 0.35, and 7) 0.5.

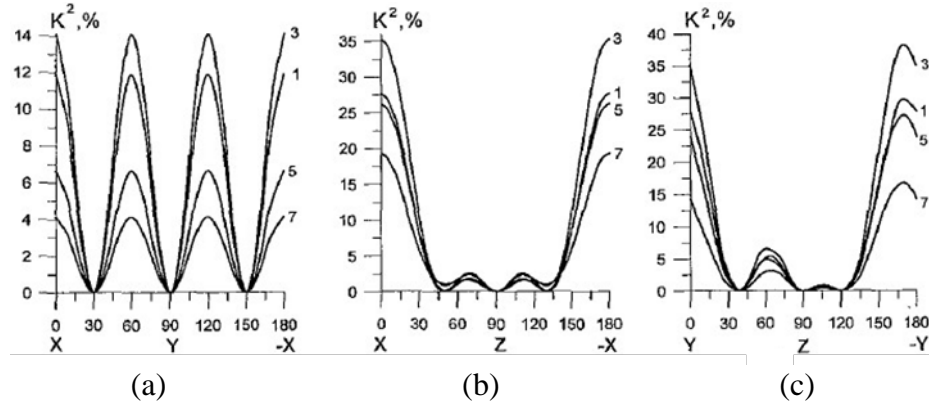


Fig.2. 6. Simulated K^2 for various cut of LN vs. wave propagation direction from [13]. h is the thickness of LN thin film, λ and is the acoustic wavelength. (a) K^2 of SH0 mode for Z-cut. (b) K^2 of SH0 mode for Y-cut. (c) K^2 of SH0 mode for X-cut. $h/\lambda = 1$ 0.01, 2) 0.025, 3) 0.05, 4) 0.1, 5) 0.25, 6) 0.35, and 7) 0.5.

Finite element analysis was used to derive the electromechanical coupling factor as a function of both LN thickness ($h=h_{LN}$ for LN alone LVRs) and the LN/SiO₂ composite plate thickness ($h=h_{LN}+h_{SiO_2}$ for LN/SiO₂ LVRs) over acoustic wavelength ratio (h/λ) (see Fig.2.7), in plane orientation of LN films, relative thickness of the composite layers for LN/SiO₂ LVRs, and metal coverage of resonator fingers, respectively. As for the LFE S0 mode of vibration, the coupling coefficient of the laterally vibrating devices is derived by comparing the phase velocity, v_m , of the thin film stack having electrodes patterned on the top surface (ground boundary condition) with the phase velocity, v_0 , of an unmetallized surface (free boundary condition). Note that what make a difference here and hence allow the computation of the coupling coefficient is the different boundary conditions (BC) set for the LN thin film (metallized surface indicates a short BC and unmetallized surface an open BC). The basic idea being explored is that the efficiency of coupling can be related to a change in phase velocity of a piezoelectric acoustic wave which occurs when an ideal, infinitely thin conductor is placed on the surface supporting the acoustic wave propagation, altering the electric field distribution in the piezoelectric material. When the wave propagation direction on the cut is such that the velocity difference is large, the tangential electric field is large at the surface of the crystal, and strong interaction with an electrode transducer would be expected with the consequence of increased coupling efficiency. The 2D FEA of the film stack is performed by

imposing periodic boundary conditions at the two ends of the film stack cross section having a width equal to the wavelength. The k_t^2 can then be expressed as [13],

$$K^2 \approx \frac{v_0^2 - v_m^2}{v_0^2} \quad (2.8)$$

$$k_t^2 = \frac{K^2}{1 + K^2} \quad (2.9)$$

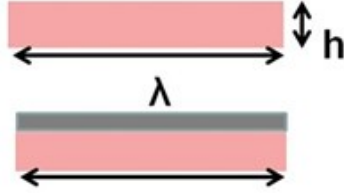


Fig.2. 7. Mock-up view of for both metalized and non-metalized LiNbO₃ plate with its characteristic dimensions shown.(Note that the metal is not physically present as a mechanical element with defined ρ , E and geometric dimesions but sets an electrical boundary condition)

where K^2 is the intrinsic electromechanical coupling, and k_t^2 the effective electromechanical coupling. Note that such estimation cannot reveal the impact of the actual finite geometry of resonators (edges), metal coverage on k_t^2 . The ultimate electrode location and boundary conditions will affect the k_t^2 value in the actual device. The FEA, though, permits us to rapidly evaluate different material orientations and select the most appropriate one for obtaining maximum coupling and hence filter bandwidth.

As for the TFE S0 mode, equivalent d_{31} re-defined for the selected cut of LN substrate is utilized (so as to generate lateral strain through application of electric fields oriented across the thickness of the films.). LN substrate cut and in plane orientation was selected in order to maximizing the equivalent d_{31} coefficient utilized and hence maximizing k_t^2 . The maximization of equivalent d_{31} was conducted by properly rotating the LN crystal in Cartesian coordinate in 3D space implemented with Matlab (see appendix A for the code). Calculation indicated that maximum d_{31} and hence maximum coupling ($k_t^2 \sim 12\%$) for the TFE S0 mode is achieved via Y-cut LN with an in plane CW rotation of 90° with respect to Z axis. FEA was employed to guide the design and verify the performance of the designed TFE resonator.

Derivation of the electromechanical coupling factor as a function of the LN/SiO₂ composite plate thickness ($h=h_{\text{LN}}+h_{\text{SiO}_2}$ for LN/SiO₂ LVRs) over acoustic wavelength ratio (h/λ), in plane orientation of LN films, relative thickness of the composite layers for LN/SiO₂ LVRs, and metal coverage of resonator fingers was conducted in a similar manner and is reported in section 4.2 for X-cut and Y-cut respectively.

3. Development of micromachining process for LN Resonant MEMS

Because of its extraordinary electromechanical and electro-optical properties, thin film LN is of great interest for both acoustic and optical applications. Nonetheless, it remains a great challenge to attain high quality suspended films of single crystalline LN. Various methods have been explored to obtain thin films of LN. Amongst the most interesting there are physical vapor and chemical vapor deposition, sol-gel process, and thin film transfer.

Thin film deposition methods, including sputtering [14], [15], [16], chemical vapor deposition (CVD) [17], epitaxial growth [18], [19] and pulsed laser deposition [20] have been attempted. However, the LN thin film obtained from sputtering is either amorphous or polycrystalline and displays very high losses. In the case of CVD, the LN had twined crystals which affect the piezoelectric response of the film. Epitaxially grown LN is generally single crystalline but exhibits some defects in the domain orientation, and generally grows only in the z-direction. Lastly, the pulsed laser deposited LN has been reported to be polycrystalline.

Sol-gel processing [21] renders highly textured but polycrystalline films of LN. As for epitaxy, the sol-gel process is inherently limited to growing c-axis (equivalent to Z-cut) films. Z cut LN is proven to have great optical properties [22] but is not ideal for acoustic application given the poor electromechanical coupling coefficient associated with lateral in-plane vibrations

Overall, these thin film deposition techniques either results in poor material quality (crystallinity) or do not permit to gain access to all film orientations.

Instead, thin film transfer techniques based on laser irradiation or ion implantation [9][23][24] have achieved single crystalline thin film quality over large areas for different orientations. LN films of thickness ranging from fraction of a micron up to 10 μm can be transferred via crystal ion slicing over a large area (3 inch ~ 4 inch wafers) on either a silicon or LN carrier substrate. The limitation here is that

the cost of the laser irradiation or ion implantation is relatively high when processed by external vendor which can be greatly reduced if conducted in-house for large scale industrial production. For our work, we have decided to use ion-sliced samples of Y-cut and X-cut LN, which have achieved single crystalline thin film quality over large areas for different orientations. An alternative technique based on layer transfer uses grinding and polishing instead of slicing. In this case a LN wafer is directly bonded to a carrier substrate and polished to the desired thickness. Although it produces films with lower uniformity than ion-slicing, it is an interesting approach that yields high crystalline films and that will also be explored in this thesis.

In this section, substrate selection for devices is firstly presented. Successively, the details of the fabrication process based on the ion-sliced samples of Y-cut and X-cut LN thin film bonded on both Si and LN substrates acquired from external vendors are presented. An overview of the process used to fabricate the devices of 1st generation (based on LN/SiO₂/Si sample) is followed by a detailed explanation of the process for the realization of the devices of the 2nd generation (based on LN/SiO₂/LN sample) and the devices of the 3rd generation (based on LN/Si sample). The new platforms are developed to address the large parasitic capacitance introduced by the use of thermally grown oxide on the high resistivity silicon substrate. By adopting the LN/SiO₂/LN and LN/Si samples and introducing some modifications in the 1st generation process respectively, it was possible to reveal the high coupling factor of the fabricated resonators without doing parasitic de-embedding. Furthermore, the acquisition of the samples through Nano-LN and NGK enabled us to fabricate the devices directly on 4" substrates. As shown by the experimental results, the direct processing of 4" wafers instead of small samples permitted us to showcase the ultimate capabilities of the LN technology.

3.1 Substrate selection & technology development

As described in section 2.1, the main focus of this dissertation is the study of LN resonators vibrating in the S0 mode because of the capability of having multiple frequencies on the same substrate, intrinsic high k_t^2 , high Q and higher phase velocity over corresponding SH0 mode.

As for the TFE S0 mode in LN, a metal layer below the LN thin film is required. At the time of this dissertation, this is considered to be a significant challenge from a manufacturing standpoint, given the difficulty of finding vendors capable of providing such initial substrate. Therefore, this dissertation mainly focuses on the demonstration and optimization of LFE resonators made out of LN thin films and vibrating in the main S0 mode. As discussed in 2.1.2, for targeted LFE S0 mode, both X and Y-cut LN are selected for the development and study of LN LVRs.

The samples considered to build both standalone LN and LN/SiO₂ LVRs in this work are: (a) ion-sliced LN thin film bonded on high resistance (HR) Si substrate through thermally grown SiO₂ layer, (b) LN thin film bonded on quartz substrate, (c) LN thin film bonded on (HR) Si substrate and (d) LN thin film bonded on LN substrate through a plasma enhanced chemical vapor deposited (PECVD) SiO₂ layer.

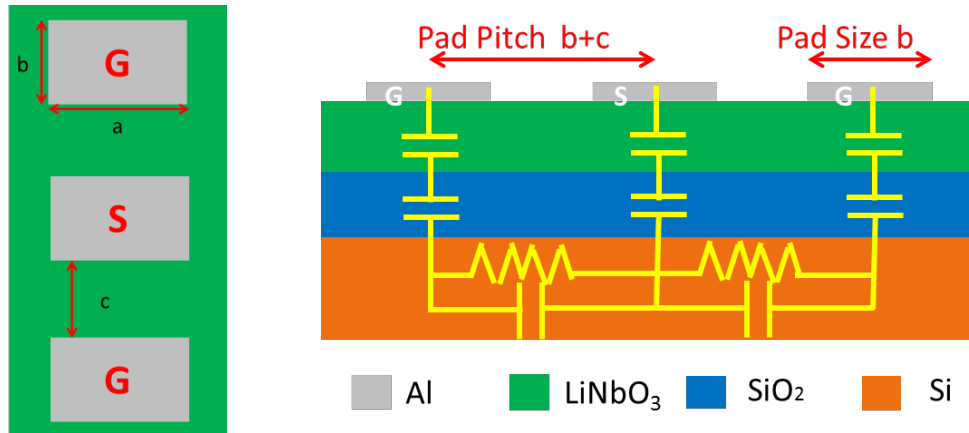


Fig.3.1 (a)Top view of the pad layout and (b) the cross section view overlapped with lumped electronic component of the LN/SiO₂/Si composite stack aquired from Partow technologies. The pad dimension a is 90 μ m, b 50 μ m and c 100 μ m.

Among these various substrates, substrates of type (a) provide the flexibility to fabricate both standalone LN and LN/SiO₂ LVRs by including/not an additional release step (see section 3.2 for details), which selectively etches the SiO₂ layer under the resonator using vapor HF. Type (a) samples composed of both X-cut and Y-cut LN thin film were available from Partow technologies, hence labeled as PT1 and PT2 as shown in Table 3.1. In either case, the LN film had thicknesses of 500 nm and 420 nm respectively and were transferred and bonded to a silicon substrate through an intermediate layer of SiO₂ being 800 nm and 1600 nm thick respectively. The sliced surface of the LN thin film was polished by chemical mechanical polishing (CMP) and exhibited an rms surface roughness around 0.16 nm. However, a relatively large parasitic capacitance (~150fF) was observed from the measurements of devices built on these substrates. To investigate the origin of the parasitics, same pad layout structures (see Fig.3.1) were built on top of PT2 (LN/SiO₂/Si composite stack acquired from Partow technologies), PT2-Ta (SiO₂/Si stack, LN film stripped from LN/SiO₂/Si stack from Partow technologies), PT2-Tb (Si, SiO₂ layer stripped from LN/SiO₂/Si stack from Partow technologies), and PT2-Tc (Si processed with KOH etching). Test samples (Table 3.1 PT2-Ta, PT2-Tb, and PT2-Tc) were prepared from LN/SiO₂/Si stack from Partow technologies (PT2) and served as reference/comparison to identify the source of the parasitic capacitance. KOH was employed to partially etch the Si from the interface bonded with SiO₂ to remove the possible charges trapped in Si layer. RF measurements were conducted for the same pads layout on all the substrates.

A large parasitic mitigation has been observed from PT2-Tb, the LN/SiO₂/Si stack from Partow technologies after SiO₂ stripping. And the capacitance value further decreased on PT2-Tc, sample of the same as PT2-Tb after KOH processing, indicating that charges were likely trapped between the thermally grown oxide and the high resistivity silicon substrate, as reported in [25]. Such charges accumulated in the oxide layer short together with the Si layer and end up generating a larger parasitic feed through. These parasitics end up having a deleterious effect on the effective coupling of the resonators and render extremely difficulty the demonstration of filters with very low loss.

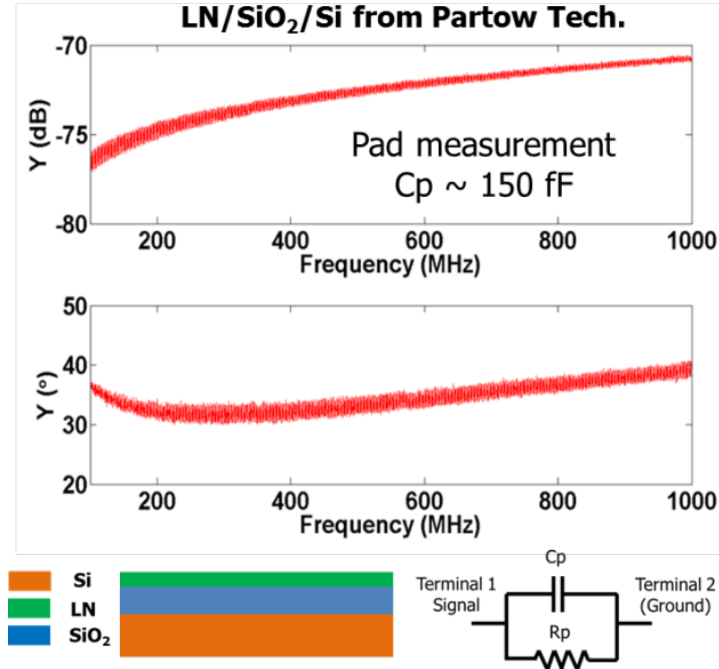
Table.3. 1. List of samples available for test

Type	Sample ID	Sample Composition	Vendor
(a)	PT1	Y-cut LN(4200nm)/SiO ₂ (1600nm)/Si (0.5 mm)	Partow Tech
	PT2	X-cut LN(500nm)/SiO ₂ (800nm)/Si (0.5 mm)	Partow Tech
(b)	PT2_Ta	SiO ₂ (800 nm)/Si (0.5 mm)	Partow Tech
	PT2_Tb	Si (0.5 mm) after oxide stripping	Partow Tech
	PT2_Tc	Si (0.5 mm) after oxide stripping and KOH etching	Partow Tech
(c)	NGK	LN (1 μ m)/Si (0.5 mm)	NGK
(d)	NANO_LN	LN (650nm)/SiO ₂ (2 μ m)/LN (0.5 mm)	Nano-LN

Substrate of type (b), (c) and (d) described in Table 3.1 were proposed to address this parasitic issue. As for the substrate of type (b), (c) and (d), the large parasitic should all be greatly mitigated due to the removal or replacement of intermediate thermally grown SiO₂ layer, nonetheless, it's considered a significant challenge to release the LN thin film by selectively etching the quartz from fabrication standpoint for (b) substrates. Therefore, substrate of type(c) and (d) turned out to be the ideal candidate to build LN LVRs in this work, but only render standalone LN LVRs. The same pad layout structures were built on top of NGK sample of type(c) and Nano_LN samples of (d) as listed in Table 3.1. A pad parasitic capacitance of 26 fF and 35 fF were demonstrated respectively, which compares favorably with the 150 fF recorded in the case of LN on silicon through SiO₂ (see Fig.3.2). An equivalent circuit with the capacitive component lumped as C_p and resistive component lumped as R_p in parallel was developed to fit the measured admittance response. This model rather than the more realistic one shown in Fig.3.1 (b) is adopted. R_p is ignored in Fig.3.2 (b) and (c) since the pad layout structures built on top of Nano_LN samples demonstrated a quasi-purely capacitive response with lumped R_p value well below 25 Ω .

For the purpose of demonstrating and studying both standalone LN and LN/SiO₂ LVRs, both option (a) (c) and (d) are adopted. Since substrates of type (a) became available before type (c) and (d), hence a full fabrication process has been firstly developed based on LN/SiO₂/Si composite stack and

implemented leading to the 1st generation of LN and LN/SiO₂ LVRs. Although the LVRs built with LN/SiO₂/Si composite stack demonstrated high figure of merit (high Q and electromechanical coupling, k_t^2), de-embedding of the parasitic capacitance coming from the pad layout have to be implemented to reveal the “true” performance of the devices.



(a)

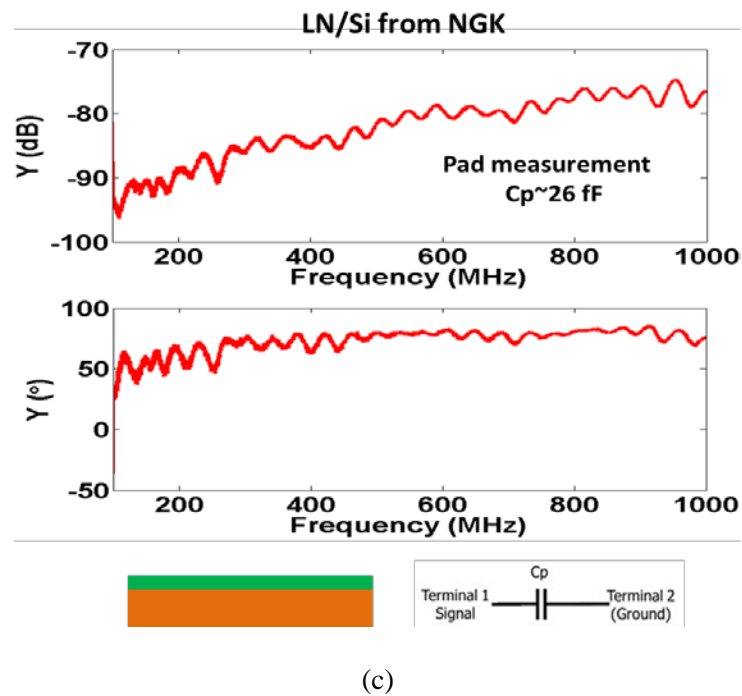
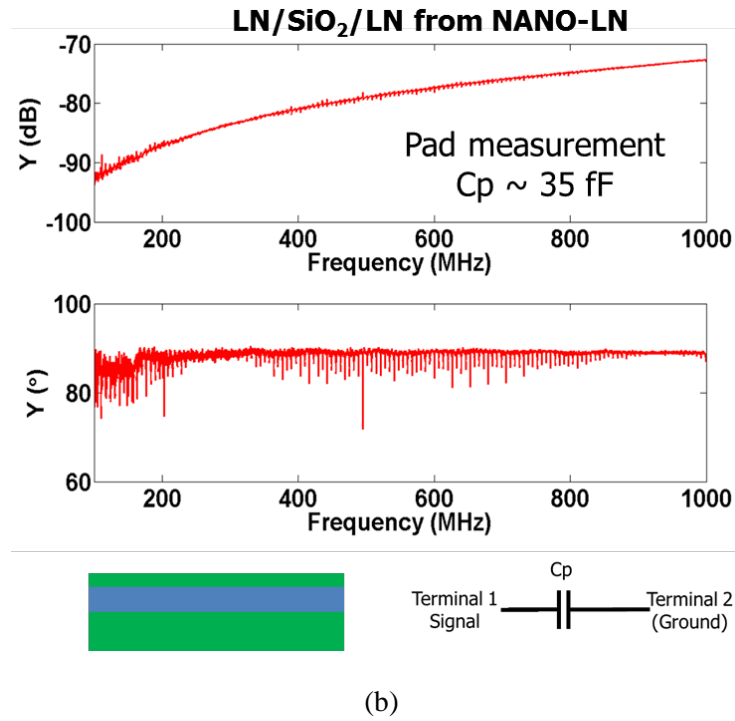
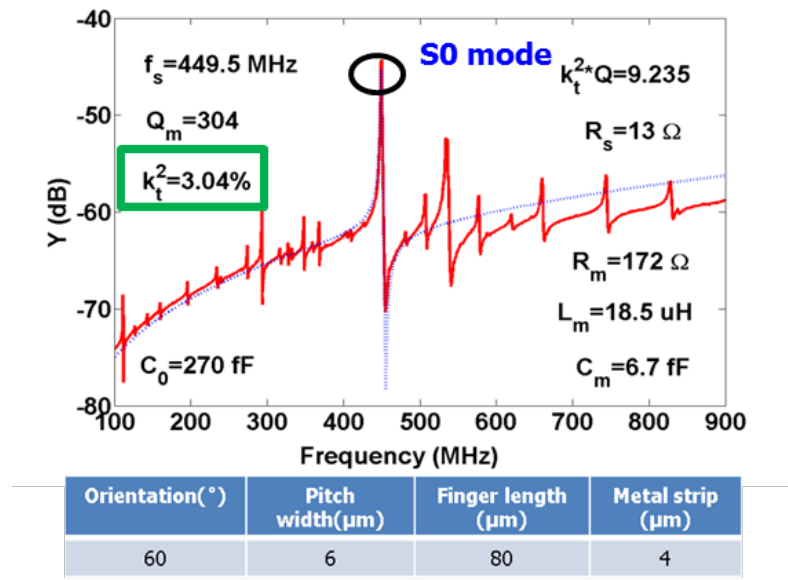
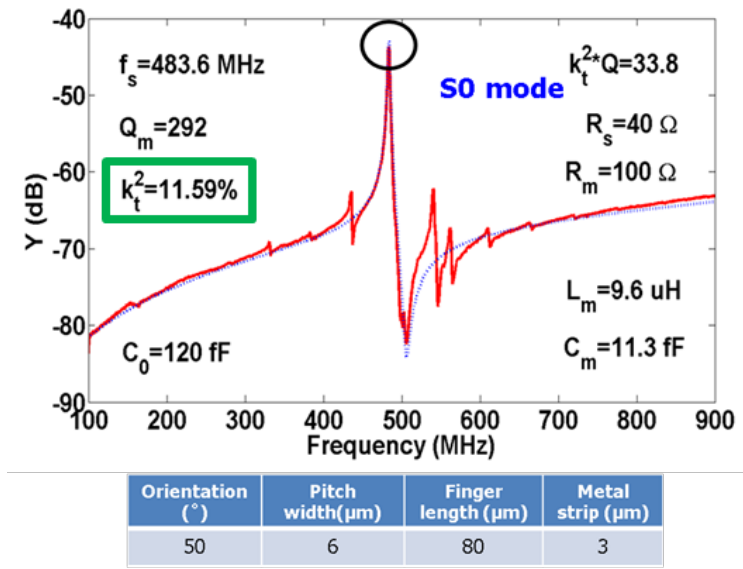


Fig.3.2. RF measured response, cross section block view and lumped electronic circuits of pad layout structures (approximate model that closely approximate pads around 500 MHz, the frequency at which the majority of the devices of this thesis are designed and fabricated) built on the top of (a) PT2, LN/SiO₂/Si composite stack acquired from Partow technologies and (b) NANO_LN, LN/SiO₂/LN stacking samples acquired from NanoLN (c) NGK, LN/Si stacking samples acquired from NGK

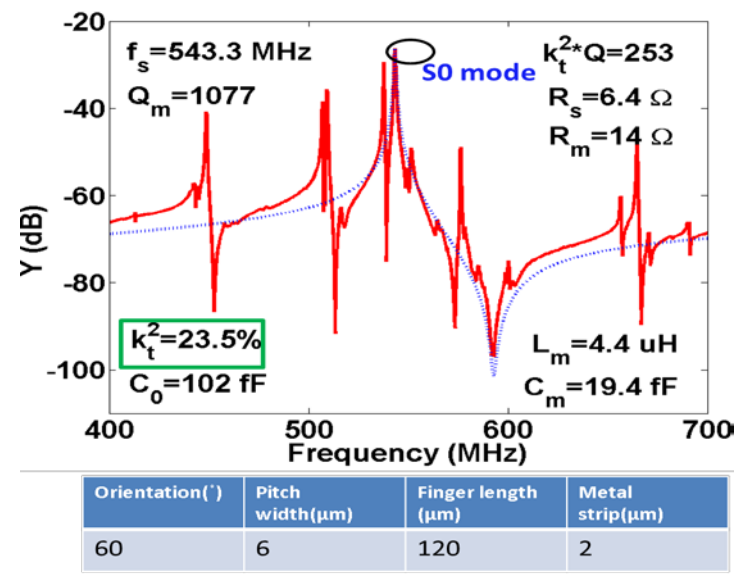
The use of LN/SiO₂/LN and LN/Si samples requires development of new fabrication process flow and can only lead to standalone LN devices. The typical response of LN LVRs (raw data from measurement without de-embedding) built with LN/SiO₂/Si composite stack acquired from Partow technologies, LN/SiO₂/LN stack acquired from NanoLN and LN/Si stack acquired from NGK are shown in Fig.3.3, demonstrating a great parasitic mitigation with the LN/SiO₂/LN and LN/Si sample. The fabrication process developed for all 3 platforms are explained in detail in the following chapter.



(a)



(b)



(c)

Fig.3.3. response of LN LVRs (raw data from measurement without de-embedding) built with LN/SiO₂/Si composite stack acquired from Partow technologies, LN/SiO₂/LN composite stack acquired from NanoLN and LN/Si stack acquired from NGK

3.2 1st generation standalone LN and LN/SiO₂ LVRs

As described in the previous section, it remains a great challenge to attain high quality suspended films of single crystalline LN. Such difficulties are exacerbated by the integration of a SiO₂ layer with LN on silicon given the considerable lattice constant and coefficient of temperature expansion (CTE) mismatch between these materials. Because of these various issues, in most cases, the suspended films defined even in this work show significant residual stresses that impact the overall device yield.

The film transfer and polishing for the sample used in the 1st generation standalone LN and LN/SiO₂ LVRs are done by an external vendor, Partow technologies. A fabrication approach that is applicable for both LN and LN/SiO₂ LVRs has been developed (Fig.3.4). Inter-digitated fingers (10 nm Cr/100 nm AlSiCu) are patterned by lift-off on top of the LN thin film, and pads and anchors area are covered by a sputtered deposited Au layer for acoustic mismatch enhancement, followed by a plasma enhanced chemical vapor deposition (PECVD) of SiO₂ (1.5 μ m). This SiO₂ layer is used as the etch mask to define the acoustic boundaries for the LN resonator. The Cl₂-based RIE etch of LN is optimized to yield straight sidewall. Any remaining SiO₂ masking layer on the top surface is removed by dry etching. After the RIE of LN, XeF₂ gas is used to remove the Si layer under the resonant structure, yielding the LN/SiO₂ LVRs. The standalone LN LVRs require an additional release step, which selectively etches the SiO₂ layer under the resonator using vapor HF.

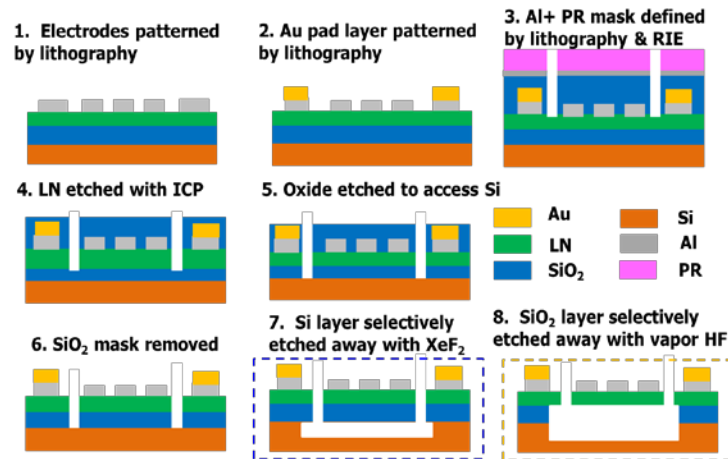


Fig.3.4. Process flow for LN/SiO₂ LVRs (boxed in dashed blue) and LN alone LVRs(boxed in dash orange).

The critical steps and challenges that were identified and tackled in this work are:

- small feature electrode definition with Karl Süss MA6 Contact Aligner (MA6)
- definition of thick SiO_2 ($1.5\ \mu\text{m}$) mask by RIE with straight sidewall and clean surface
- anisotropic etching of LN by RIE with straight sidewall and clean smooth surface

As electrode pattern dimensions get smaller, it became challenging for the MA6 to resolve features smaller than $1.0\ \mu\text{m}$, especially when dealing with small samples. The lithography was constrained to the utilization of the mask aligner because samples were in the size of $12\ \text{mm} \times 10\ \text{mm}$, which are not compatible with higher resolution tools such as a stepper. This challenge was exacerbated by variations in the photoresist (PR) height across the die. The height variations were observed after PR development in IDT area of electrodes exclusively when feature size was below $1.5\ \mu\text{m}$, which led to failure of IDT definition. Such PR change in thickness is a result of the poor quality of the exposure (imposed by the equipment), which can be addressed by making the PR thicker so that pattern definition become insensitive to thickness variations. PR of different families and thicknesses (adjusted by spinning speed) were, thereafter, characterized to optimize the definition of tiny electrodes ($\sim 1\ \mu\text{m}$). Experiments indicated that PR of AZ4210 span at 5000 rpm would enable the definition of electrodes with small features down to $1\ \mu\text{m}$ and thickness up to 300nm for either Al or Au.

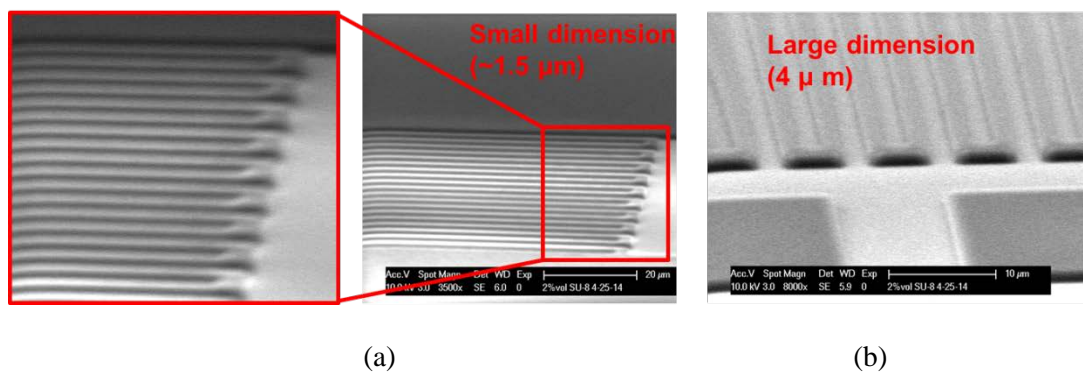


Fig.3.5. SEM images of lithographically defined PR of (a) shrunk thickness for small features ($\sim 1.5\ \mu\text{m}$) and (b) normal height for large features ($\sim 4\ \mu\text{m}$) due to poor quality of the exposure

As for anisotropic etching of LN, LN ICP etch recipe based on Cl_2/BCl_3 chemistry has been (developed for Y-cut LN) optimized and re-qualified for X-cut LN. Ar is removed from the previously developed recipe [5] to reduce the physical bombardment of the LN surface. The ratio of ICP power to RIE power is increased to improve the side wall angle. A higher ICP power together with a higher flow rate of Cl_2 and BCl_3 is applied to achieve a higher etch rate.

During the etching procedure, SiO_2 serving as the RIE mask for LN displayed a good selectivity being 1:2. An Al mask (thickness of $0.3\ \mu\text{m}$) was used to pattern the SiO_2 layer for the etching of the LN and oxide layer underneath LN film such that a significant sidewall improvement ($\sim 90^\circ$ with respect to 60° from trials without Al masking) and high selectivity of Al to SiO_2 (1:10) improvement were attained. However, oxide etching could not proceed through till desired thickness ($1.5\ \mu\text{m}$) during the actual device fabrication due significant Al redeposition and grass formation at the bottom of the etched trenches. A milling step was required to complete etch. To address this issue, a thick PR ($\sim 4\ \mu\text{m}$) was used on top of Al during SiO_2 etching to obtain a clean etch and straight SiO_2 sidewall angles (see Fig.3.6 (a)). Such SiO_2 mask with smooth surface free from Al polymer contamination yield smooth LN surfaces and straight sidewalls ($\sim 80^\circ$) while preserving a high etch rate ($\sim 200\text{nm}/\text{min}$) (see Fig.3.6 (b)).

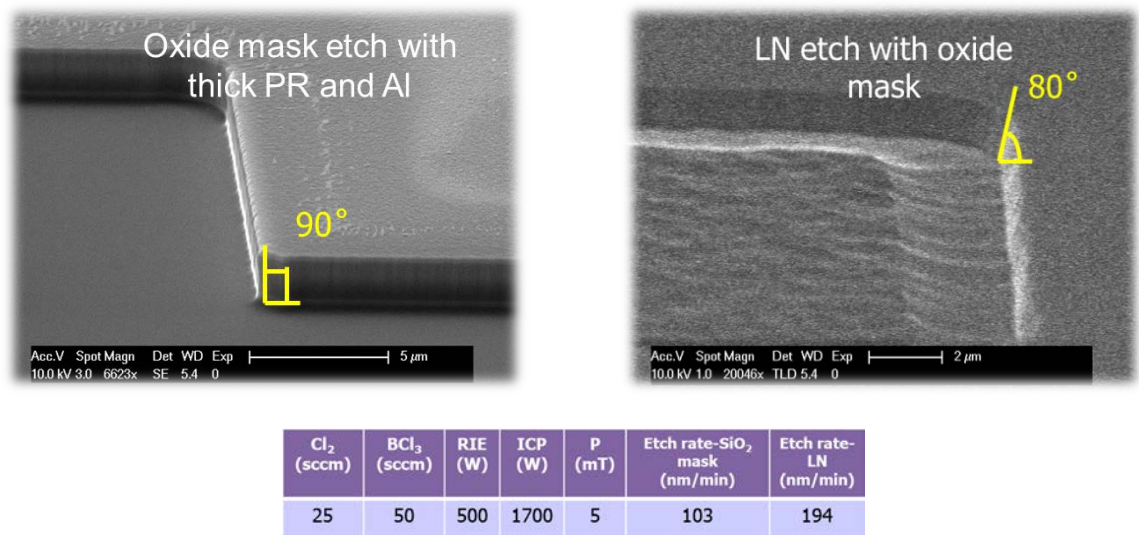


Fig.3.6. SEM image of SiO_2 patterned with thick PR/Al masking(left) and LN etched with the patterned SiO_2 mask(right) and the optimized chlorine-based RIE recipe for X-cut LN films obtained from Partow Tech.

Note that the SiO_2 etching with vapor HF has been characterized for the 1st generation devices to render standalone LN devices as illustrated in Fig.3.4 step 8, but was not problematic as it was a short step.

Furthermore, development of an in-house adaptor (Fig. 14) for adapting the die size sample based on LN/ SiO_2 /Si to 4" wafer processing on stepper to scale the devices into higher frequencies and improve the resolution of lithographical definition of features was attempted. Single die size sample was mounted onto the center of a 4-inch carrier wafer, and the rest of the carrier was planarized with Si tiles of equal thickness as the sample with kapton tapes. A new PECVD SiO_2 process was developed at 150°C, and used to deposit SiO_2 as the etch mask for LN to fit the kapton tapes temperatures limitation up to 220 °C.

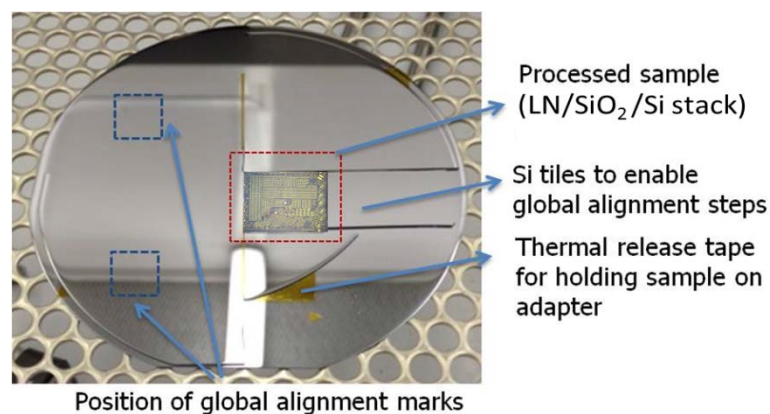


Fig.3.7. An in-house adapter for using a stepper to achieve smaller feature size and better alignment accuracy. The new processing capability is explained in the inset table.

Although devices with smaller feature size (scaled to higher frequency) were successfully fabricated with the tile adaptation method, the fabricated devices' performance were well below expectation due to the fabrication challenge associated with tile taping and mask alignment recognition associated with stepper. Manually taped tiles frequently encountered problems including height deviation from piece to piece, tiny cracks or taping edge stretching into alignment mark area, contamination induced by out gas/liquid from kapton tape which led to failure of mask alignment with stepper or

considerable misalignment error ($>0.6 \mu\text{m}$) comparable to MA6. Moreover, the developed low temperature (150°C) PECVD SiO_2 process rendered a lower quality SiO_2 which demonstrated a much faster etch rate with the previously optimized LN etching recipe applied. Such degradation of selectivity required an additional increase of SiO_2 masking layer thickness for LN etching.

3.3 2nd generation LN alone LVRs

As discussed in 3.1, the remaining challenge associated with the 1st generation LN LVRs based on LN/ SiO_2 /Si substrate were: 1) limited alignment accuracy imposed by either using MA6 or stepper with tile-taping method which introduced spurious modes in device response, and 2) the presence of a large parasitic capacitance introduced by the use of thermally grown oxide on the high resistivity silicon substrate which ended up having a deleterious effect on the effective coupling of the resonators and rendered extremely difficult the demonstration of filters with very low loss.

The 2nd generation of devices discussed in this section addressed the reported issues by utilizing samples made out of LN/ SiO_2 /LN in order to reduce parasitic capacitance and electrical losses and successfully evolved into 4" wafer processing with a stepper achieving higher resolution and better alignment accuracy. We acquired full wafer substrates with $1 \mu\text{m}$ LN thin film (3" dimension) bonded to a LN carrier wafer (4" dimension) through $2 \mu\text{m}$ SiO_2 from NANO-LN (see Chapter 2 for evaluation of substrate parasitics).

The use of such LN/ SiO_2 /LN samples required development of a new fabrication process flow (Fig.3.8) and can only lead to standalone LN devices.

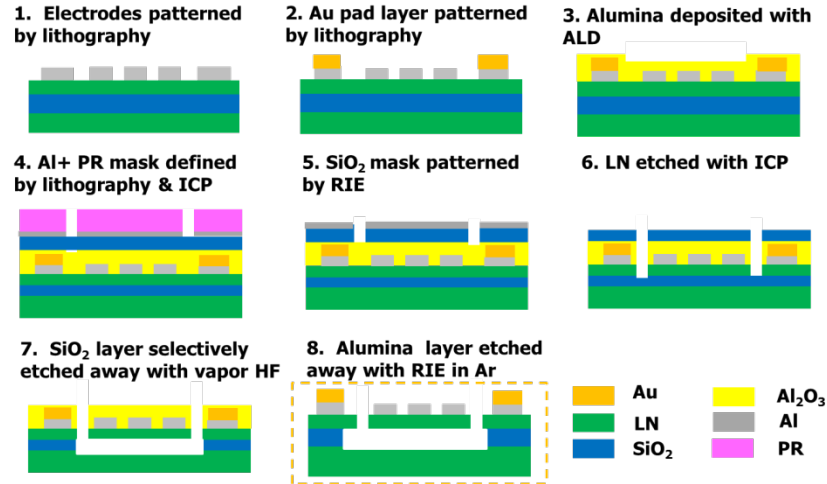
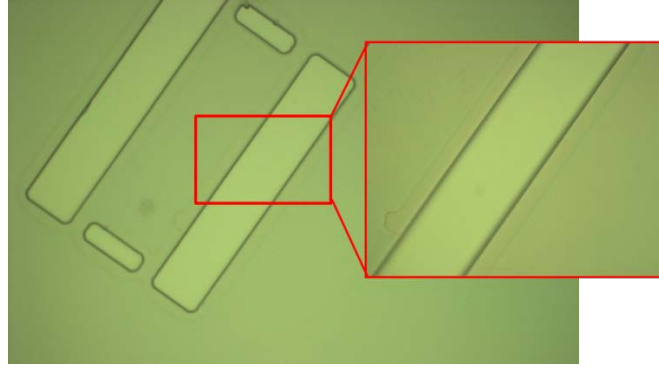


Fig.3.8. Updated fabrication process flow for the making of LN devices based on LN/SiO₂/LN composite stack

We characterized the critical fabrication steps required to demonstrate resonators in this new material stack including re-characterizing the etching of LN films from the new vendor and characterizing the selectivity between LN and SiO₂ during vapor HF (VHF) etch, which needed to be used to release the resonator from the LN substrate.

Fast LN ICP etch recipe based on Cl₂/BCl₃ chemistry was re-qualified for X-cut LN from the new vendor. SiO₂ is used as mask (1: 2.4 selectivity) and patterned via thick PR/Al mask. Smooth surface free from re-deposition was obtained. (Fig.3.9). To quickly demonstrate device prototypes, we decided to dice the 4" LN/SiO₂/LN composite stack into dies (15 mm x 15mm dimension) after the SiO₂ mask patterning (step 5 in Fig.3.8) and etch the LN film using the same recipe we had previously identified to work. Note that the etching is the very last step and no additional lithographic steps are required. Moreover, to remove the Alumina protective layer on the top of LN thin film, an etching recipe based on RIE in Ar was developed.



Cl ₂ (sccm)	BCl ₃ (sccm)	RIE (W)	ICP (W)	P (mT)	Etch rate-SiO ₂ mask (nm/min)	Etch rate-LN (nm/min)
25	50	500	1700	5	81.5	192.7

Fig.3.9. Optical image of LN with thick PR/Al masking etching and the re-qualified chlorine-based RIE recipe for X-cut LN films obtained from Nano-LN.

Table.3. 2. Alumina Trion etching recipe developed

Etched	Masking	Ar flow	RF Power	Pressure	Rate
Alumina	PR	20 sccm	50W	20 Torr	~25A/min

We used both previously fabricated LN/SiO₂ LVRs and LN/SiO₂/LN samples to test the VHF etch step. VHF etching recipe was developed and shown in Table 3.3. Fig. 3.10 shows that regular crystals were formed and attached to the LN top surface after 3.5 hours (time required to complete release for samples from Partow technology) of VHF processing. Energy-dispersive X-ray (EDX) spectroscopy analysis was conducted to analyze the composition of these particles and confirmed that they are formed by Nb and F element (Fig.3.10 (b)). These by-products are likely due to etching of LN along specific orientations. The reaction appears to be self-limiting to few surface monolayers of the LN film as the LN thickness change is less than few nanometers. Masking layers of different material types and thicknesses (200-800 nm thick amorphous silicon and 30-50 nm thick Alumina) (see Table 3.4) were tested to protect the LN surface from being attacked by VHF and successive re-deposition of by-products. We verified experimentally that we can address this issue by utilizing at least 30 nm of Alumina layer. 30nm Alumina

was selected because we can optionally do direct probing without removing alumina from pads (eliminate step 8 in Fig. 3.8).

Table.3. 3. VHF etching recipe developed

Etched	VHF flow	Pressure	Rate
SiO ₂	20 sccm	5 mTorr	~5 μm/min

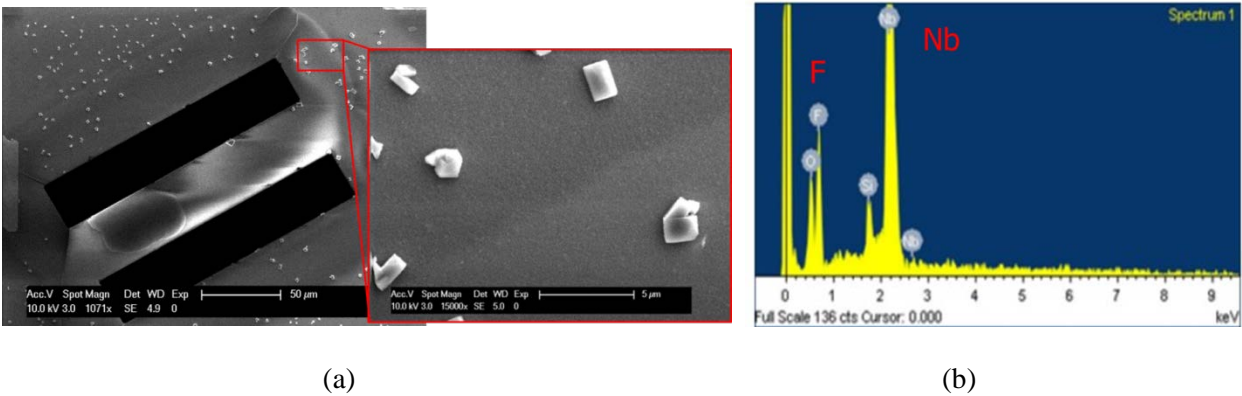

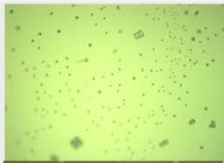
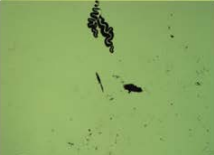
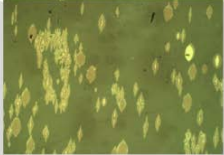

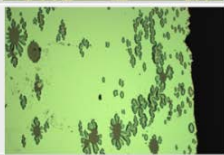

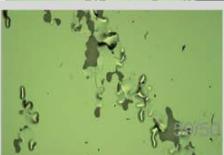






Fig.3.10. (a) SEM image of patterned LN processing with VHF for 3.5h with zoomed in.view showing regular crystalline particles attached to the top LN surface. (b) EDX spectrum report on the element composition of the particles

Table.3. 4. Comparison of LN covered with different material types and thicknesses (200-800 nm thick amorphous silicon and 30-50 nm thick alumina) as protection layer before and after VHF etching using the same developed VHF etching recipe for 3.5 hours

Test sample	Masking material	Masking layer thickness (nm)	Performance	
			Before VHF etch	After VHF etch
O	Blank LN without masking	NA		
A	Amorphous Si (from 8L sputtering system) on LN	220		
B	Amorphous Si (from 5 targets sputtering system) on LN	500		
C	Amorphous Si (from 5 targets sputtering system) on LN	800		
D	Alumina (from ALD) on LN	30		
E	Alumina (from ALD) on LN	50		

After the characterization of the associated critical steps, the fabrication process shown in Fig.3.8 has been validated on an X-cut NANOLN sample (15 mm X 15 mm) formed by 495 nm LN bonded to LN through 2084 nm SiO₂ and demonstrated resonators of frequency around 500 MHz. Au pad layer deposition and removal of Al₂O₃ were not performed in this implementation.

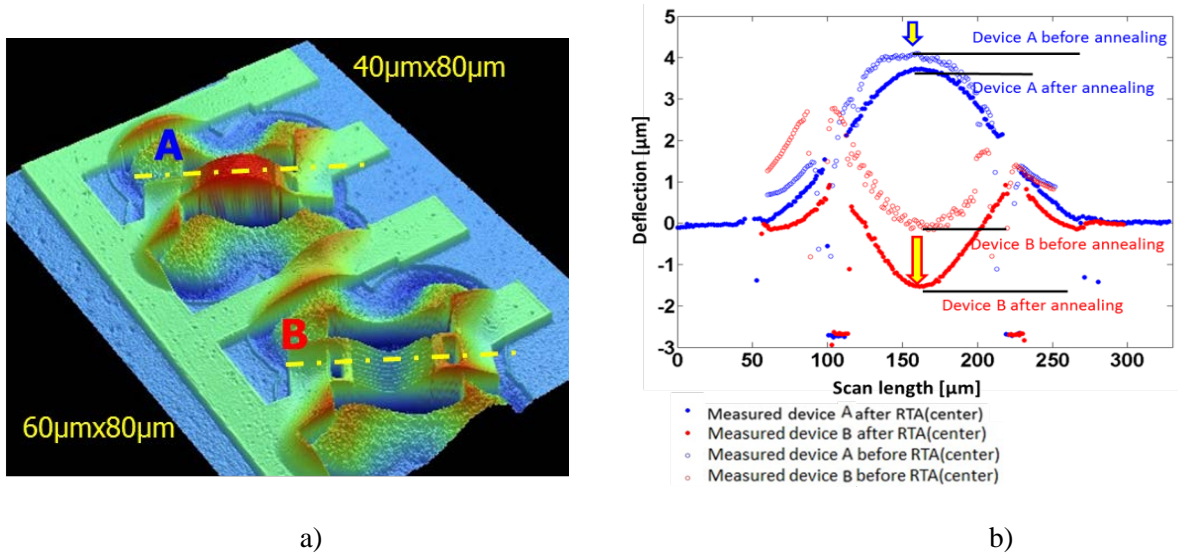


Fig.3.11. (a) Wyco 3D image of fabricated LN LVRs from LN/SiO₂/LN die. (b) plot of deflection profiles of device A and B (as shown in (a)) before and after 1st annealing step

Wyco optical scans were conducted for the fabricated devices, revealing that there are large residual stresses and some devices were touching the substrate. An annealing test was performed on the released sample to characterize whether it had any impact on the device Q . The first fabricated die containing the LN LVRs was placed in an Rapid Thermal Annealing (RTA) system and subjected to 3 different annealing steps (1 – 300°C for 5 min, ramp time of 50s, cool down of 5 min, 2 – 300°C for 5 min, ramp time of 50s, cool down of 5 min, 3 – 400°C for 5 min, ramp time of 90s, cool down of 5min). A subset of devices was tested after each annealing step to verify its impact on the device performance. Plot of deflection profiles of the same devices before and after the 1st annealing step are illustrated in Fig.3.11 (b), indicating minor change in deflection profile. A considerable Q improvement was achieved after the first annealing step, ensuring that all the working devices have Q s ranging from 100 to 500 (see examples in Fig.3.12). Such Q improvement is likely due to the reduction of defects in the LN film during the annealing process as described in [26] as no significant changes were observed in the deflection profile of the devices. However, as the annealing time was extended and higher annealing temperatures were applied, we observed a slight decrease in Q . The changes in Q were accompanied by <5 % fluctuations in resonant frequency and static capacitance (see Table 3.5).

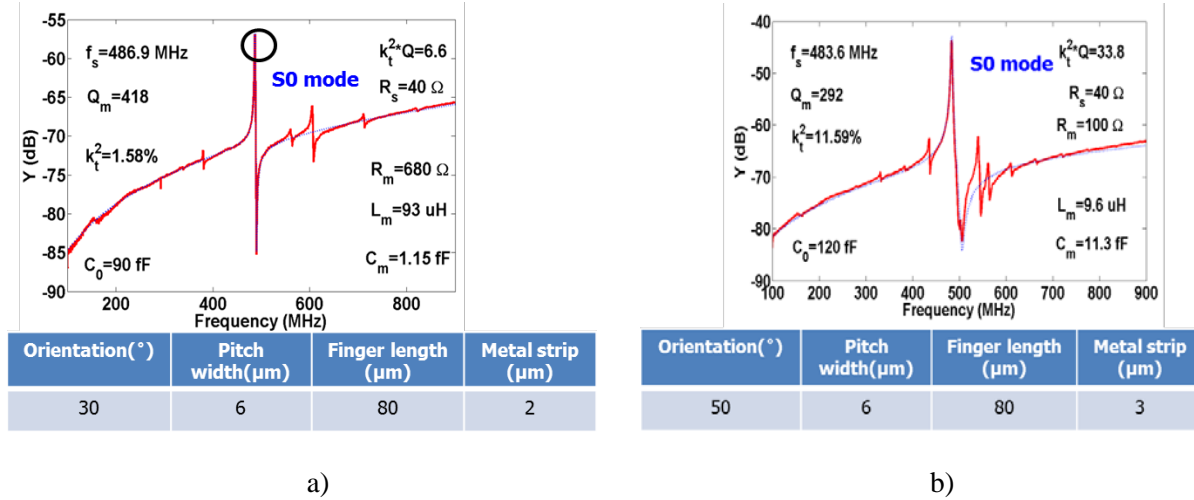


Fig.3.12. The measured and fitted admittance response of stand alone LN LVRs (10 80 μm long electrodes and, 6 μm pitch) with: (a) with 2 μm metal strip, placed at 30° to the z axis in X-cut plane) (b) with 3 μm metal strip, placed at 50° to the z axis in X-cut plane)

Table.3. 5. LN LVRs' performances evolution over annealing processing

Device #1: mode of vibration: SH0 mode; orientation: 70° to the +z axis; electrode pitch: 6 μm; electrode width: 4 μm; electrode length: 80 μm.

Device #2: mode of vibration: SH0 mode; orientation: 90° to the +z axis; electrode pitch: 6 μm; electrode width: 2 μm; electrode length: 80 μm.

Device #3: mode of vibration: S0 mode; orientation: 50° to the +z axis; electrode pitch: 6 μm; electrode width: 2 μm; electrode length: 120 μm.

Sample status	Device #1			Device #2			Device #3		
	C_0 (fF)	k_t^2 (%)	Q	C_0	k_t^2	Q	C_0	k_t^2	Q
0 annealing	129	13.22	39	119	15.76	30	155	11.67	32
1 st annealing	121	14.19	220	115	15.54	133	155	10.33	140
2 nd annealing	140	11.14	187	140	12.81	102	165	7.64	134
3 rd annealing	153	11.09	140	155	13.08	83	190	8.91	57

Apart from the low Q , the devices fabricated with LN/SiO₂/LN stack acquired from Nano-LN demonstrated inconsistent values of k_t^2 between different fabrication runs (which will be detailed in Chapter 5). It is suspected that these variations originate from the LN film being attacked by VHF during the release step. Further studies on different methods to release the device are required in order to finally assess whether this LN film on LN platform can be used for the making of RF MEMS devices.

3.4 3rd generation LN alone LVRs

As discussed in section 3.3, the 2nd generation of devices addressed the reported issues by utilizing samples made out of LN/SiO₂/LN in order to reduce parasitic capacitance but yielded devices

with low Q and inconsistent k_t^2 . To address these challenges and simultaneously ensure low parasitics from the substrate, we acquired full wafer substrates with 1 μm LN thin film (4" wafer) bonded to a Si carrier wafer (4") from NGK.

The use of such LN/Si samples required development of a new fabrication process flow (Fig.3.13) which can only lead to standalone LN devices.

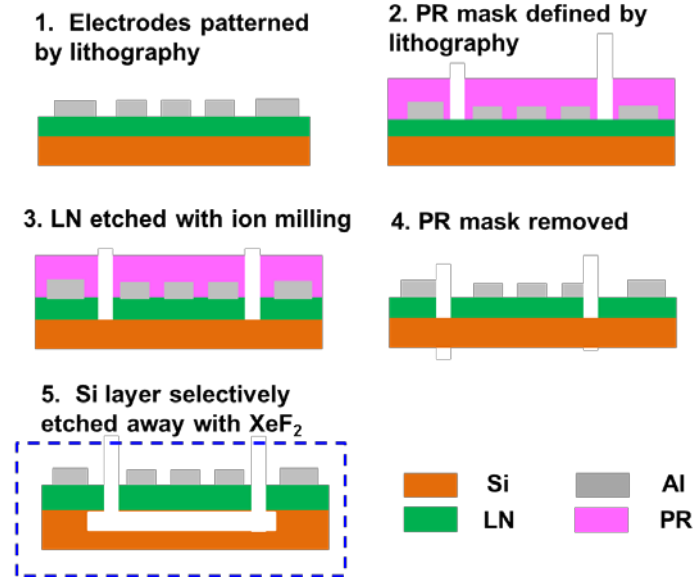


Fig.3.13. Updated fabrication process flow for the making of LN devices based on LN/Si composite stack

Although the previously developed LN ICP etch recipe based on Cl_2/BCl_3 chemistry can be exported to this process flow, issues with the ICP etcher forced us to look at an alternative way of etching LN using ion milling. A thick PR ($\sim 5 \mu\text{m}$) was used as mask and patterned via lithography. Smooth surface free from re-deposition with side wall angle approaching 90° was obtained. (Fig.3.14).

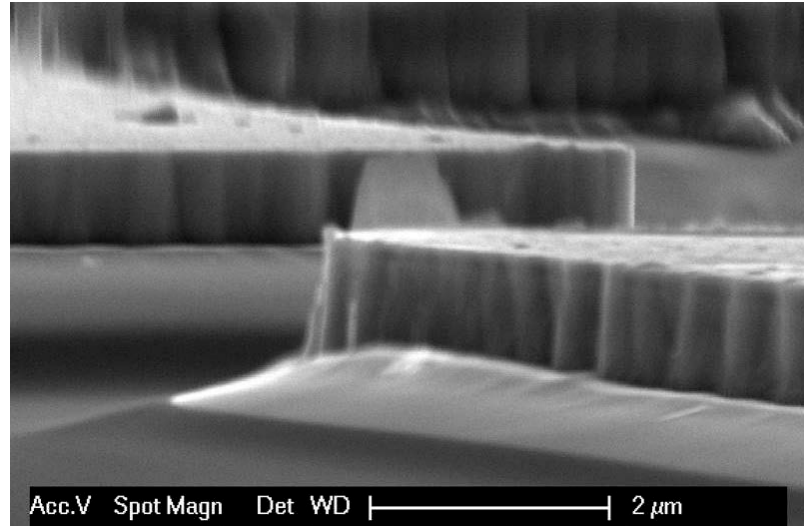


Fig.3.14. SEM image of LN with thick PR masking ion milling

After the characterization of the etch step, the fabrication process shown in Fig.3.14 was validated on an X-cut NGK sample (4" wafer) formed by 1 μm LN thin film (4" dimension) bonded to a Si carrier wafer and demonstrated resonators of frequency around 500 MHz. The performance of these devices will be detailed in Chapter 5, where important findings about the device Q versus key resonator geometrical parameters are reported.

4. Design of high k_t^2 LN LVRs

The rapidly growing demand from customers for multifunctional wireless communication systems is driving the development of monolithic frequency-agile RF front ends. Such RF front-ends require miniature filtering modules that can cover the current commercial operating bands and potentially offer adaptation to future standards. Piezoelectric-based acoustic resonators and filters, such as thin film bulk acoustic wave resonators (FBARs) and surface acoustic wave (SAW) devices, have been the key enabling technologies for RF filtering in mobile phones. Although SAWs and FBARs meet existing requirements, they are limited in producing multiple frequency filters on the same chip. Laterally vibrating MEMS resonators [5] [27] [28] have recently emerged as a compelling solution for the implementation of multi-frequency resonators on the same substrate. Nonetheless, the electromechanical coupling (k_t^2) of these devices, which dictates the achievable bandwidth and insertion loss for acoustic-based RF filters, remains very limited and insufficient to construct wideband filters (>3% bandwidth).

This chapter describes the efforts that were made on the design and demonstration of active reflectors (Fig.4.1) for enhancing the electromechanical coupling (k_t^2) of LVRs based on X-cut ion-sliced LN thin film. By adding electroded quarter wavelength ($\lambda/4$) regions at the two ends of the resonant plate, active reflectors (since an electrical signal is applied to them) are formed to improve the device performance. Ak_t^2 of ~13 % was demonstrated for the LN/SiO₂ resonators– the highest ever recorded for temperature compensated laterally vibrating resonators (temperature compensation will be describe in Chapter 7). The k_t^2 demonstrated herein surpasses commercially available Aluminum Nitride (AlN) FBARs (k_t^2 =6.5%) [29] as well as SAW devices (k_t^2 =10%) [30]. Differently from the AlN CMR, these resonators attain k_t^2 that meet the bandwidth requirements (3%~6%) of existing commercial bands. Therefore, the high k_t^2 and multi-frequency LN thin film resonators of this work can be used to form filters covering all the existing communication standards and potentially offer unprecedented adaptive frequency response at the chip scale.

4.1 Active reflectors for high performance LN LVRs

Previously, LN resonator design that consisted of a number of evenly spaced IDT metal fingers with identical width (Fig. 4.1(a)), referred as conventional design afterwards) were demonstrated and studied [5]. Although this type of electrode configuration is proven to be effective for AlN CMRs [31], it introduces unwanted spurious modes and overtone resonances for LN resonators due to the material's high intrinsic k_t^2 . It is also inefficient and does not maximize the k_t^2 by dispersing the energy in various modes. In this dissertation, an active reflector design was introduced as a method to achieve high k_t^2 for LN LVRs. Demonstration and complete study has been conducted for LN LVRs operating at 500 MHz since this frequency is of interest for some telecommunication system and the corresponding electrode pitch width of $6\ \mu\text{m}$ ($\lambda=12\ \mu\text{m}$) is readily obtained with a mask aligner (Karl Suss MA6), the lithographic equipment adopted in 1st generation devices' fabrication. By adding electroded quarter wavelength ($\lambda/4=3\ \mu\text{m}$) regions at the two ends of the conventional resonant plate (see Fig.4.1), active reflectors were formed to enable a two-fold improvement in k_t^2 in the same device footprint.

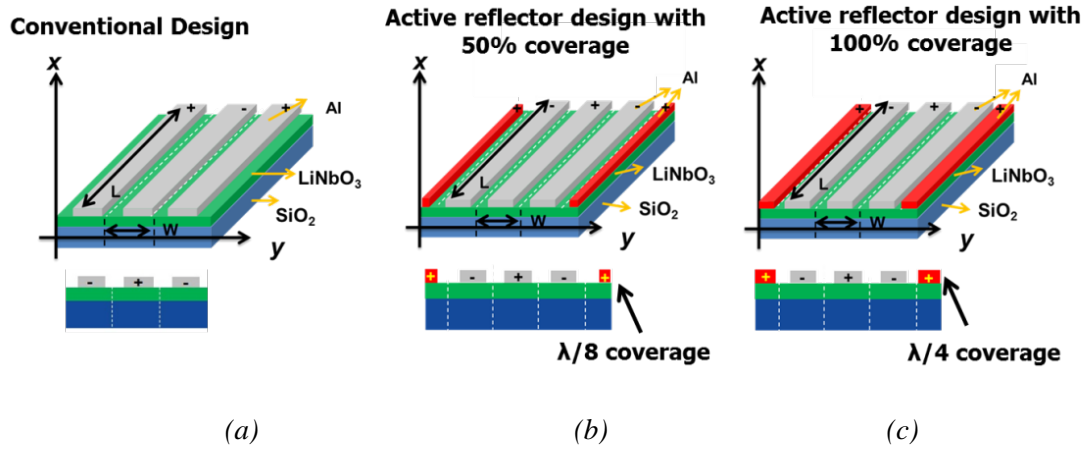


Fig.4.1 Mock-up view of the LN on SiO₂ LVR of: (a) conventional design without active reflectors, (b) 50% covered active reflector, and (c) 100% covered active reflector

Furthermore, the new design is demonstrated in a LN on SiO₂ technology platform (on a silicon substrate) that simultaneously addresses the issue of large temperature coefficient of frequency exhibited by stand-alone LN devices (see chapter 7 for TCF compensation). LN and SiO₂ thicknesses were selected to be 500 nm and 800 nm respectively to minimize TCF.

Finite element method (eigenfrequency analysis) described in section 2.1.2 was used to derive the electromechanical coupling factor for S0 mode of vibration as a function of in plane orientation in the designed LN(X-cut) /SiO₂ composite plate. Periodic boundary conditions were imposed at the two ends of the film stack cross section having a width equal to the wavelength ($\lambda=12\text{ }\mu\text{m}$). Triangle elements were selected to mesh the cross section due to their better accuracy (compared to quadrangles) and flexibility to mesh small features. Default extra fine meshing was set such that the maximum element size was below $1/7.5\lambda$ ($1.6\text{ }\mu\text{m}$) and hence the number of degrees of freedom (DOF) was set to be at least 15 times larger than λ . The direction of wave propagation in the X-cut LN plane were varied from -90° to 90° in increments of 10° with respect to the Z-axis. The direction of wave propagation was optimized based on the goal of maximizing k_t^2 . The FEM data suggests that a maximum coupling for the S0 mode that exceeds 10 % is found for an in-plane rotation of 60° with respect to the +z axis (see Fig.4.2).

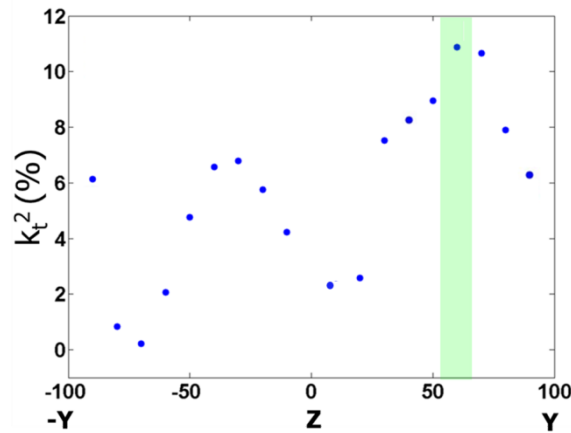


Fig.4.2. The simulated k_t^2 for LN on SiO₂ LVRs for various orientations.

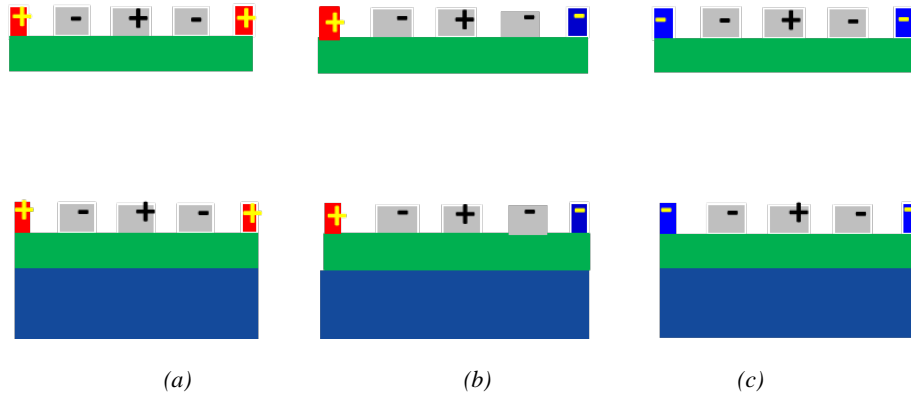


Fig.4.3. Mock up view of LN alone(top) and LN/SiO₂ LVR of active reflector design with polarity (signal or ground) of $\lambda/4$ active reflectors at the two edges of the resonators varied as (a) opposite-opposite from adjacent main finger, (b) opposite-same and (c) same - same as adjacent main finger

Metal coverage and polarity (signal or ground) of $\lambda/4$ active reflectors were also designed via FEA (frequency response analysis) to attain maximum k_t^2 . Note that in these cases frequency response analysis were conducted in order to take into account the impact of the edges and metal coverage of the resonant plate. The actual film stack cross section including the electrode was constructed. The top electrodes covering the main fingers were set to terminal and ground alternatively. Terminal type was set to voltage with electric potential setting to 1V. The direction of wave propagation is oriented for an in-plane rotation of 60° with respect to the +z axis based on the goal of maximizing k_t^2 . The same triangle elements were selected to mesh the cross section. Default extra fine meshing was set such that the maximum element size was below $1/7.5 \lambda$ ($1.6 \mu\text{m}$) and hence the number of degrees of freedom (DOF) was set to be at least 15 times larger than λ . Polarity (signal or ground) of $\lambda/4$ active reflectors at the two edges of the resonators were varied as –opposite-opposite from adjacent main finger, –opposite-same and same - same as adjacent main finger (see Fig. 4.3). The BC of the main fingers on the resonators were kept unchanged in all the different configurations. Simulation indicated that active reflector designs with all various BC setting combination achieve larger k_t^2 compared to corresponding conventional design and the –opposite-opposite polarity configuration rendered the maximum k_t^2 . Metal coverage of $\lambda/4$ active reflectors was swept from $0.25 \mu\text{m}$ (8.3% coverage) to $3 \mu\text{m}$ (100% coverage) in increments of $0.25 \mu\text{m}$ (8.3% coverage increment) with both polarities setting to be different from adjacent main fingers. The k_t^2 was extracted from the simulated admittance response of each configuration according to a simplified equation that expresses k_t^2 as a function of C_m/C_o as in definition #4 in table 2.3:

$$k_t^2 = \frac{\pi^2}{8} \frac{f_p^2 - f_s^2}{f_p^2} \quad (4.1)$$

where f_p and f_s are the resonator series and parallel resonances. As shown in Fig.4.4, the FEA suggested that 33% covered active reflector renders the maximum k_t^2 (13.6%), 50% covered active reflector renders the secondary maximum k_t^2 (13.1%), both surpassing by 2X the k_t^2 (6.6%) of conventional design and 100% covered active reflector yield a slightly smaller value (11.5%) (see Fig.4.5). Since the 33% covered active reflector design for LN on SiO₂ LVRs vibrating at 500 MHz requires 1 μm wide metal strips at the resonator edge which is challenging to resolve with a mask aligner, 50% covered active reflector design (1.5 μm wide metal strip) are adopted for validation of this analysis.

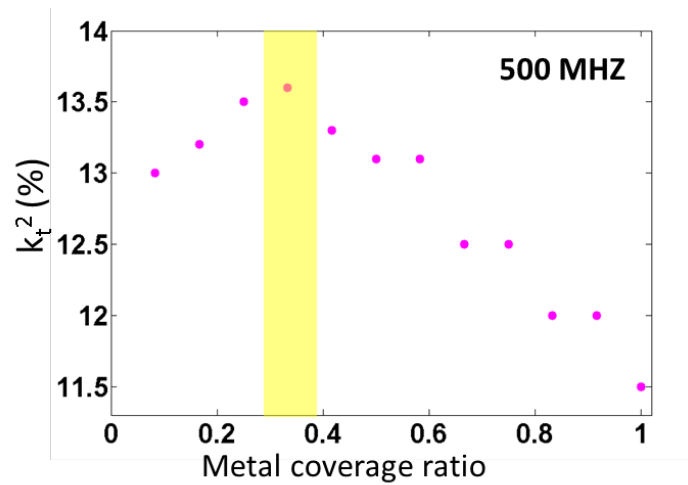


Fig.4.4. simulated k_t^2 for LN on SiO₂ LVRs vibrating at 500 MHz for various metal coverage ratio for $\lambda/4$ resonator fingers

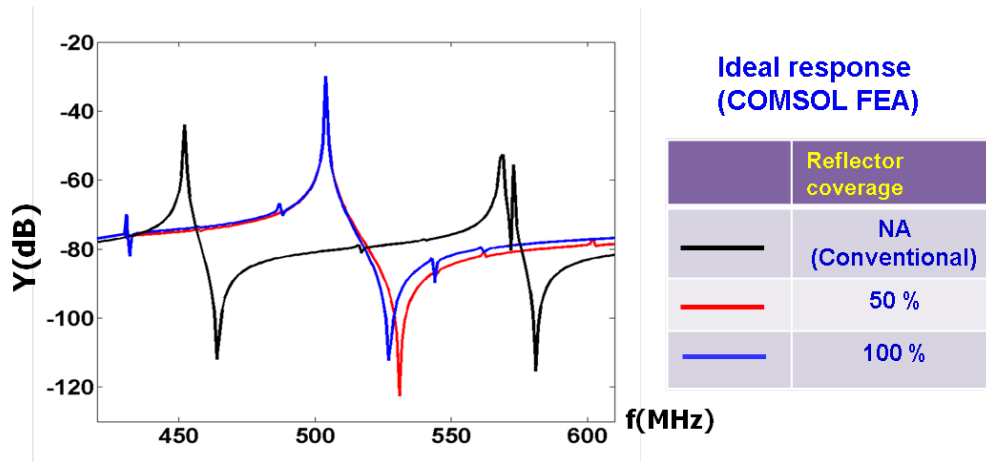


Fig.4.5. The simulated frequency response and extracted k_t^2 for LN on SiO₂ LVRs for conventional design and active reflector design with metal coverage ratio for $\lambda/4$ resonator fingers being 100% and 50%

4.2 Electrode coverage optimization in terms of k_t^2

With the goal of further maximizing the coupling coefficient, the k_t^2 of the S0 mode in both LN only and LN/SiO₂ composite plate, FEM (frequency response analysis) was also used to optimize the metal coverage ratio for $\lambda/2$ resonator fingers to attain maximum k_t^2 . In this case, X-cut LN plates with in plane orientation set to give maximum coupling were modeled. 500 nm X-cut ion-sliced LN thin film on 800 nm SiO₂ was used in the simulations.

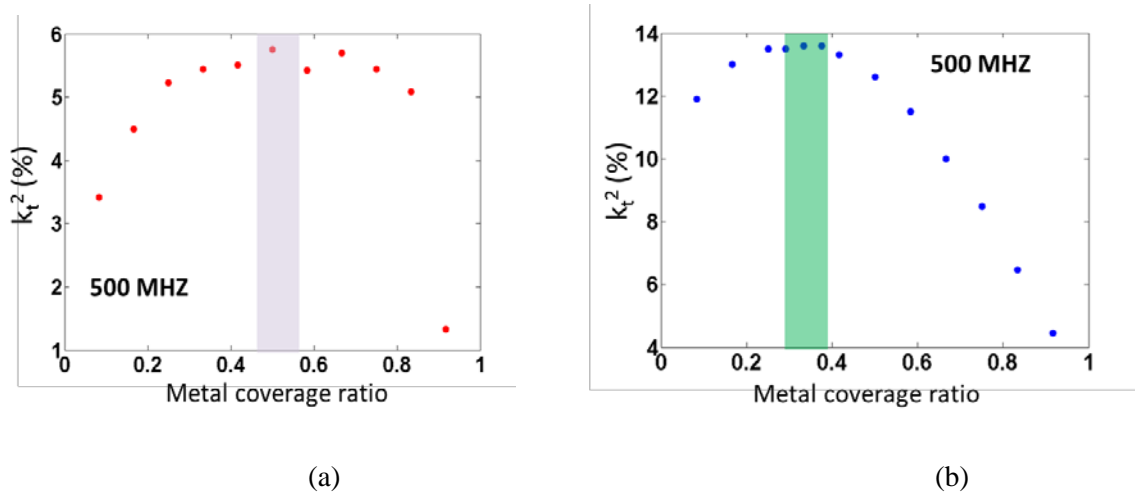


Fig.4.6. The comparison of the averaged measured and simulated k_t^2 for LN on SiO₂ LVRs for various coverage ratios for (a) conventional design and (b) active reflector design respectively

The simulated k_t^2 for the S0 mode for various electrode coverages are plot in Fig. 4.6. The plots suggest that maximum k_t^2 can be achieved for electrode coverage set to 50 % for conventional design and 30% with active reflectors. The same maximum electrode coverage gives peak k_t^2 for different frequency (observed from simulations for 250MHz and 750MHz) as well. The COMSOL FEA shows that a maximum k_t^2 of $\sim 13\%$ can be obtained from designed LN/SiO₂ devices. The simulation results were validated experimentally by building a matrix of devices with different parameters as listed in Table 4.1.

Table.4. 1. Characteristic geometrical parameters of the main LN/SiO₂ LVRs studied in this work. type A, B and C refer to active reflector design with 100%, 50% (shown in fig. 4.1 (b) and (c)) and no metal coverage (0%) respectively for resonator vibrating around 500MHz. Type D refers to the corresponding conventional design (fig. 4.1(a)).

Device type	Electrode pitch [μm]	Metal strip width on main finger [μm]	Metal strip width on active reflector [μm]	Electrode aperture [μm]	Electrode coverage of main finger [%]	Electrode coverage of active reflector [%]
A1	6	2	3	80,120	30%	100%
A2	6	3	3	80,120	50%	100%
A3	6	4	3	80,120	67%	100%
B1	6	2	1.5	80,120	30%	50%
B2	6	3	1.5	80,120	50%	50%
B3	6	4	1.5	80,120	67%	50%
C1	6	2	0	80,120	30%	0%
C2	6	3	0	80,120	50%	0%
C3	6	4	0	80,120	67%	0%
D1	6	2	NA	80,120	30%	NA
D2	6	3	NA	80,120	50%	NA
D3	6	4	NA	80,120	67%	NA

4.3 Experimental Results

The designed LN on SiO_2 devices were fabricated following the first generation devices' fabrication flow shown in Fig.3.4 and described in Chapter 3. The fabricated devices were tested in an RF probe station via an Agilent (N5230A) Network Analyzer. Q was extracted from the admittance plot by measuring the 3dB bandwidth of the resonance peak. The six equivalent circuit parameters were determined by fitting the measured results to the MBVD equivalent circuit model after de-embedding of the parasitic capacitance coming from the pad layout.

The designed S0 mode is present in the admittance response of devices placed at all orientations, and is dominant (highest Q) when the devices are placed at all orientations except from -50° , -60° and -70° to $+z$ axis. As shown in Fig. 4.6(b), a k_t^2 of 10.6% was measured for a resonator of 50% covered active reflector design and 30% main finger coverage resonating at a frequency of 483.5 MHz placed 60° to the $+z$ axis, which is around 2X the k_t^2 demonstrated with the corresponding conventional design (Fig.4.7.(a)).

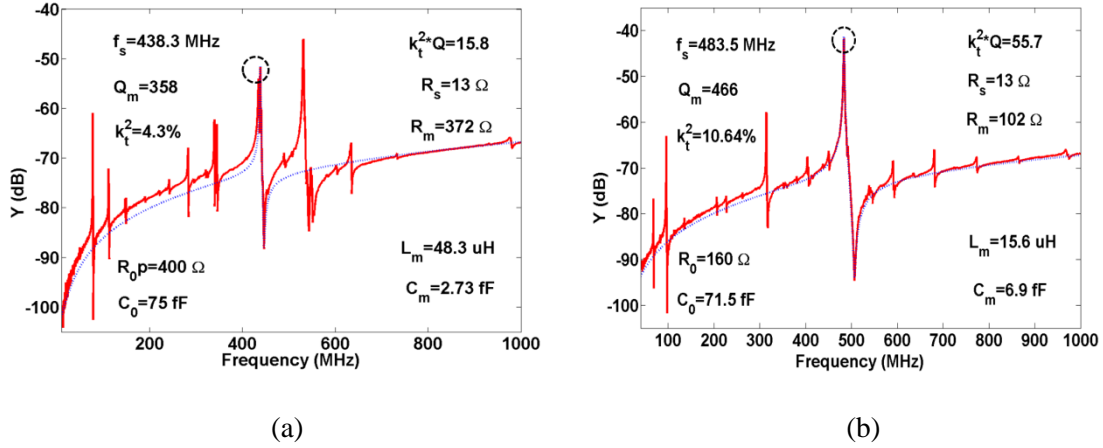


Fig.4.7. The measured and fitted admittance response of a LN on SiO₂ LVR vibrating at 500 MHz(10 80 μm long electrodes and, 6 μm pitch with 4 μm metal strip, placed at -60° to the z axis in X-cut plane)) of: (a) conventional design (b) active reflector design with 50% coverage

The average value of the measured k_t^2 displayed the same trend of the simulated results, but showed values that deviated up to 50% from the predicted ones for certain orientations. The reason of this discrepancy might be that k_t^2 is affected by processing as x-y misalignment errors have a different impact on devices with different orientations. Experimental data also confirms that a maximum coupling for the S0 mode that exceeds 10 % is obtained for devices with active reflector placed in X-cut plane rotated 60° with respect to the $+z$ axis. (See Fig. 4.2) It is interesting to note that simulated k_t^2 value matches the experiment only when active reflectors are presented. This is likely because the 2D eigenfrequency simulation assumed an infinite piezoelectric plane by imposing periodic BC on both ends of cross section and the presence of active reflectors approaches such condition by mitigating the effect of the edges instead relevant in finite size LN plates., .

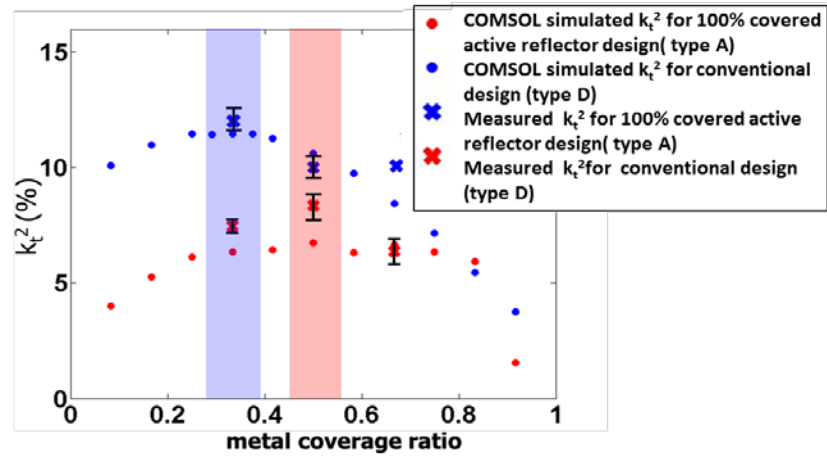


Fig.4.8. Average experimental measurements validated COMSOL simulation on metal coverage ratio for $\lambda/2$ resonator fingers for conventional design (type D) and active reflector (type A).

The frequency-temperature characteristic of the LN/SiO₂ LVRs was also monitored and is presented in Chapter 7.

5. Investigation of Q in LN LVRs

Laterally Vibrating Resonators (LVRs) based on Lithium Niobate (LN) thin films introduced in this dissertation have shown great potentials for enabling wide bandwidth, reconfigurable, and temperature stable RF filtering platforms [28]. Despite the promising features of the technology, there is no understanding of what affects the quality factor (Q) of these devices. To guarantee low noise in local oscillators or obtain a low insertion loss in filters for wireless communications, a high Q is required. Therefore, it is of paramount importance to study the energy loss mechanisms that affect the Q of the developed LN LVRs.

This section presents the studies that have been conducted to understand the energy loss mechanisms that affect the Q of the LVRs based on ion sliced X-cut LN and the methodology to enhance the Q of these LVRs..

The Q of a resonator is defined as the ratio of the energy stored in a resonator to the energy dissipated per vibration cycle,

$$Q = 2\pi \frac{\text{Average energy stored}}{\text{Energy lost per cycle}} \quad (5.1)$$

The most commonly encountered energy loss mechanisms in micromechanical resonators are [32]: air damping (Q_{air}), which refers to energy loss due to viscous damping between the moving structure and a gas (generally air); thermoelastic dissipation (TED) (Q_{TED}), which represents the energy lost due to irreversible heat transfer between regions of the resonator plate (including the metal electrodes) having different temperature when the plate flexes (such as asymmetrical, A0 mode), compresses or stretches (such as symmetric, S0 modes); Akhieser loss ($Q_{Akhieser}$), which relates to the energy dissipated through phonon-phonon interactions occurring because of the propagating elastic wave; electron-phonon coupling loss in metals ($Q_{Electron-phonon}$), which represents the energy dissipated through the collisions between thermal phonons and electrons distorted by the propagating elastic wave; piezoelectric–semiconductor

loss ($Q_{piezoelectric}$), which refers to the energy lost in acoustoelectric current generated by the interaction of time-varying electric fields with an ultrasonic wave; interfacial loss ($Q_{interfacial}$), which is introduced by the presence of a stress jump at the interface between dissimilar materials; and anchor loss (Q_{anc}), which depends on the acoustic energy transferred from the vibrating resonator into the substrate through the supports [33][34] [35]. Note that recent work [36] on CMRs based on AlN indicated that interfacial dissipation might not be attributed to the acoustic velocity jump between dissimilar materials and more experiments are needed to clarify this dissipation mechanism, if at all present.

The overall Q can be estimated by adding the impact of each specific energy loss mechanism:

$$\frac{1}{Q} = \frac{1}{Q_{air}} + \frac{1}{Q_{TED}} + \frac{1}{Q_{anc}} + \frac{1}{Q_{Akhieser}} + \frac{1}{Q_{Electron-phonon}} + \frac{1}{Q_{piezoelectric}} + \frac{1}{Q_{interfacial}} \quad (5.2)$$

Table.5. 1. List of commonly encountered energy loss mechanisms in micromechanical resonators Where m mass, ω angular frequency, e the electric charge, ρ the mass density, E_F the Fermi energy, σ the electronic conductivity, ω_c the angular dielectric relaxation frequency, ω_D the angular diffusion frequency, k^2 the electromechanical coupling coefficient, v the longitudinal acoustic wave velocity, ρ_a the density of air and η_a , the viscosity of air. D is a nonlinearity constant determined by an average over Gruneisen numbers, K the thermal conductivity, T the temperature, β the thermal expansion coefficient, C the specific heat per unit volume, C_{11} & C_{12} are the stiffness coefficients. Note that the TED estimate also include the impact of the electrodes.

Damping Mechanism	Equation for evaluation	Expected Q range at 500 MHz	Parameter to Study
Electron-Phonon Dissipation[37]	$\alpha = \frac{4m\omega^2 E_F}{15\rho e^2 v^3} \sigma \left[\frac{dB}{cm} \right]$	$10^5 - 10^6$	NA
Piezoelectric-Semiconductor Loss [38]	$\alpha = \frac{k^2}{2v} \frac{\omega_c}{1 + (\frac{\omega_c}{\omega} + \frac{\omega}{\omega_D})^2} \left[\frac{dB}{cm} \right]$	$10^5 - 10^6$	NA
Air Damping[39]	$\alpha = \frac{\pi}{5 \ln 10 * \lambda \rho T} \sqrt{\frac{\rho_a \eta_a}{\pi f}} \left[\frac{dB}{cm} \right]$	$\sim 10^5$	Pressure, frequency
Akhieser Damping (AKE) [40]	$\alpha = \frac{\omega^2 E_0 D \tau}{6\rho v^3} \left[\frac{dB}{cm} \right]$	$\sim 10^5$	Temperature
Thermo-Elastic Damping (TED) [41]	$\alpha = \frac{8.68\omega^2 \beta^2 K T' (c_{11} + 2c_{12})^2}{2\rho^2 C^2 c_{11} v l^3} \left[\frac{dB}{cm} \right]$	$\sim 10^3 - 10^4$	Electrode material, location and coverage/ Temperature

To identify the dominant loss mechanism determining the Q for devices resonating at 500 MHz, the theoretically predicted Q values imposed by all the loss mechanisms described except from anchor loss were analyzed based on the equations described and listed in table 5.1. α is the attenuation coefficient, which can be converted to Q through the following equation:

$$Q = \frac{10\pi}{|\alpha| \ln 10 * \lambda} \quad (5.3)$$

where λ is the wave length of the propagating wave and α is the attenuation coefficient in dB/m.

Anchor loss were instead analyzed via FEM. Based on the theoretical calculations, the dominant mechanisms that would possibly explain the Q s exhibited by these LN resonators are air damping, TED, AKE damping and anchor losses. All other loss mechanisms would yield $Q > 10^5$ and hence are considered negligible.

This chapter focuses on analyzing anchor losses (Q_{anc}). Perfectly matched layer (PML) is used as a boundary condition in the COMSOL FEA to obtain a description of Q_{anc} as a function of the device and support geometry. The FEA results are verified experimentally by fabricating and measuring standalone LN LVRs working at 500 MHz. Since all other loss mechanisms (air damping, AKE and TED) that could impact the device Q are drastically reduced by operating at low temperature and pressure, measurement of the same devices at cryogenic temperature was performed to validate the trends obtained via FEA.

5.1 Background work

To experimentally validate theoretical prediction and better identify dominant damping mechanisms, 1st generation devices based on Y-cut LN thin film on SiO₂ operating between 500 MHz and 1.5 GHz were designed and fabricated. Specifically, we targeted investigating the dependence of Q on: (i) electrode coverage and location, (i) air damping, (ii) frequency, and (iii) vibration mode. Frequency is considered as a variable since air damping is inversely proportional to the square root of

resonant frequency for laterally vibrating resonators (S0 mode) and has an impact on Akhieser damping and TED as well. The geometry of the resonators studied in this work is specified in Table 5.2. The devices were tested at different pressures at room temperature to separately monitor the impact of air damping on Q . Q was extracted from the admittance plot by measuring the 3dB bandwidth of the resonance peak. Measurement data were compared with theoretical values of Q imposed by all the described loss mechanisms in an attempt to identify the dominant loss mechanism that limits Q in these resonators.

Table.5. 2. Characteristic geometrical parameters of the main LN/SiO₂ LVRs studied in this work. Type a refers to segmented electrodes and the metal strip width refers to the size of a single electrode forming the pair. Type B and C correspond to the devices shown in Fig. 29b and c.

Quantity	Type a		Type b	Type c			
Top electrode finger number	10 , 20		10 , 20	10, 20			
Electrode pitch [μm]	4	6	6	2	3	4	6
Metal strip width [μm]	1	1.5	4	1	1.5	2	3
Electrode aperture [μm]	40, 80		40, 80	40, 80			
Electrode coverage[%]	50		67	50			
Top Al electrode thickness[nm]	100		100	100			

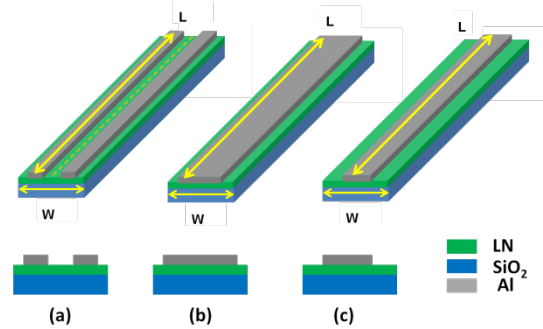


Fig.5.1 3D and cross-sectional views of a single finger of the three different types of resonator designs studied in this work: (a) segmented finger configuration, (b) conventional configuration with 67% electrode coverage and (c) conventional configuration with 50% electrode coverage.

Please notice that the LN/SiO₂ LVRs studied in this section are based on the conventional design (no active reflectors), as active reflectors had not yet been introduced at the time of this study. Therefore, most resonators exhibited a weak resonance for the main lateral vibration (known as S0 mode) set by the electrode pitch, and higher Q s for the undertone and overtone of the same mode. Despite these

limitations, we believe that the information gathered by this study can provide some general understanding and guidance of damping in these resonators.

The fabricated LVRs were tested at 298 K under vacuum ($P \sim 5.9 \times 10^{-8}$ Torr). As reported in Fig.5.2, the Q values measured under vacuum and ambient air are compared to explore the impact of pressure on Q at 298 K for resonators operating at different frequencies and different modes (labeled as: asymmetrical, A0, symmetric, S0, and its overtone). At 298 K, the Q of the devices vibrating in the S0 mode or overtone of S0 mode (50MHz to 1.5GHz) show minimal changes with pressure and ranges from 8.3% to almost no changes with frequency. For resonators vibrating in the A0 mode between 100 and 550 MHz, Q increases at low pressure, but the increment drops from 57.5% to 2% with frequency, indicating that flexural vibrations tend to have higher sensitivity to air damping than in-plane extensional vibrations.

The results confirm that air damping plays a significant role in setting the Q of flexural-like A0 modes, whereas it has a secondary role for symmetric S0 mode vibrations. It is also interesting to note that the impact of air damping weakens as the resonant frequency increases in both cases. These data further confirm that air damping is inversely proportional to the square root of resonant frequency for laterally vibrating resonators (S0 mode) [42]. These experiments set the foundations for our detailed studies of damping in LN LVRs.

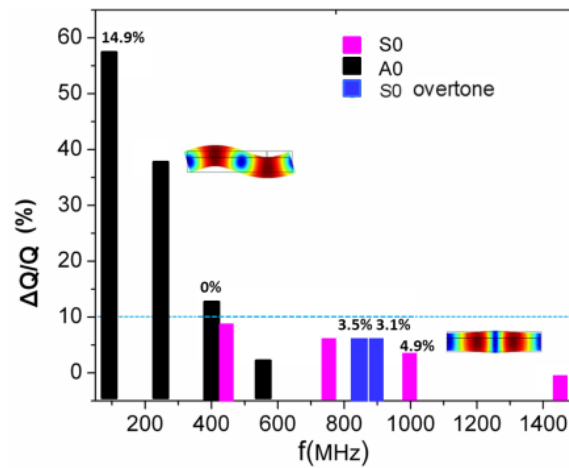


Fig.5.2. The relative Q shift with pressure (atmospheric pressure vs. vacuum) for different modes of vibration. A0 and S0 modes were found in the same devices. The frequency of A0 and S0 mode scales proportionally, so the lowest A0 frequency is recorded in the same device with the lowest frequency S0 mode. The two S0 overtones were measured in the devices with the two lower fundamental S0 modes. Each relative Q

shift value is the average obtained from measurement of 1-7 devices in the same frequency range (Please, note that the devices did not all exhibit the same exact frequency, but they were boxed in the same group as long as the frequency change was $< \pm 25$ MHz of the selected value). The standard deviation of the measured fractional change in Q is listed on the top of each bar in the plot. When only one device measurement was possible the standard deviation is not reported.

Based on these data, we believe that air damping is not the dominant loss mechanism limiting the Q for devices vibrating in the S0 mode below 1.5 GHz.

5.2 Anchor loss

Anchor loss represents the acoustic energy leakage via the support tethers into the substrates [43][44][45]. Since the substrate is generally much larger than the MEMS resonator body, it is assumed that all the elastic waves reaching the substrate are dispersed and, eventually, dissipated.

Previous studies on AlN Contour Mode Resonators (CMRs) indicated that anchor loss is an important source of energy dissipation limiting the Q in the very high frequency (VHF) range. In this section, anchor loss's effect on the performance of LN LVR is investigated via FEA. Perfectly matched layers (PML) are used to model absorption in the regions surrounding the LN LVRs.

The vibrating body of the LVR used in the FEA is formed by a 1 μ m-thick LN plate with 100nm-thick Al electrodes (top only). The devices exhibited a series resonance frequency of 500 MHz corresponding to the S0 mode of vibration displayed by a LN plate of 60 μ m width ($\lambda=12$ μ m) and 120 μ m length. The LN plate dimension is chosen as a compromise between fabrication challenges associated with suspended film cracking (due to residual stress) and obtaining large static capacitance (C_0) values that favor impedance match. The electrode pitch width is set to be 6 μ m corresponding to $\lambda/2$ of the designed frequency, 500 MHz. Active reflectors that resort to 100% metal coverage of the $\lambda/4$ extensions are selected to achieve a considerable improvement of k_t^2 , spurious mode suppression, and robustness to processing including misalignment and over/under-etching. Fixed the plate size, the impact of critical geometrical parameters on anchor losses (see Fig. 5.4) was analyzed via FEA Non-ideality such as misalignment, over-etching and sloped side wall angle of resonant plate were also considered. The

simulation results were experimentally validated through measurement of 318 LN LVRs CMRs operating around 500 MHz and having the same resonator body but different anchor and bus dimensions.

5.2.1 Analysis and 3D FEM simulations

To predict the impact of device geometry on Q_{anc} , a numerical approach based on FEA was used. PML boundary conditions are readily available in COMSOL FEM and have been previously shown to be helpful in modeling trends of Q vs. device geometry [36]. A PML is such that any incident wave reaching such boundary is completely absorbed with zero reflection.

In COMSOL Multiphysics, the use of a PML boundary condition forces the following coordinate transformation to the general coordinate variable t [46]:

$$t' = \left(\frac{t}{\Delta_w} \right)^n (1-i) \lambda_{PML} F \quad (5.6)$$

where Δ_w , λ_{PML} , F and n represent the width, wavelength, scaling factor, and order of the PML region, respectively. Both t and Δ_w are geometrical parameters that are automatically extracted for each simulated region by COMSOL. Instead, λ_{PML} , F and n can be manually adjusted as a PML parameter. We set λ_{PML} and n , as the default values, to be equal to the acoustic wavelength of vibration (λ) (the absolute value changes with the device frequency) and 1, respectively. F was set equal to 1 (the default value) [36]. The PML was defined as an additional layer attached to the edges of the released substrate. Assuming rounded corners at the end of the released regions, we split the PML into domains with two different orientations (Fig.5.3 (a)). Straight lateral sidewall angle is adopted in all the simulations, hence labeled as an ideal condition (the side wall angle cannot be perfectly 90° in general and hence referred to as ideal situation). The impact of sloped sidewall angle is separately analyzed in a section that deals with non-ideality.

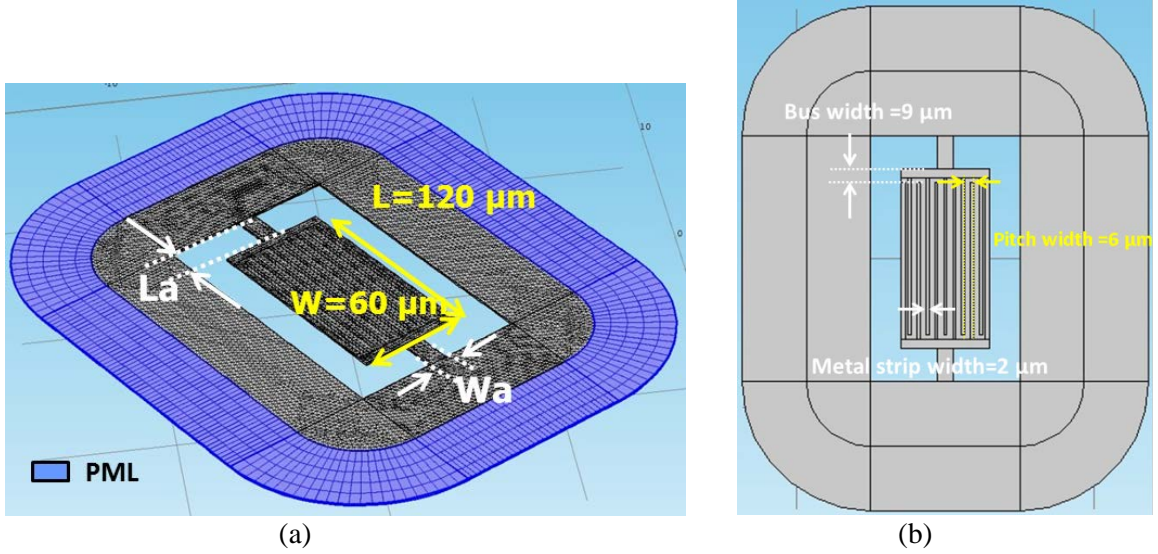


Fig.5.3. 3D COMSOL simulation with PML layer highlighted (a) and top view of the geometry (b)

To finely mesh the resonator geometry, triangle elements were selected for the whole resonant body and the released LN film due to a better accuracy (compared to quadrangles) and flexibility in meshing small features. An equally-distributed mapped surface swept across the device thickness was used in all the simulations. The maximum element size was set to be at least 5 times lower than λ and the number of degrees of freedom (DOF) was set to be at least 10 times larger than λ . Figure 5.3(a) shows the meshing distribution of a 500 MHz LN LVR using PML. The typical meshing for simulating LN LVRs at that frequency consists of more than 333,000 elements.

All simulations were conducted in COMSOL Multiphysics with standard settings for the solver. A frequency domain analysis was run to simulate the LN LVR admittance response assuming PML conditions and Q was computed using the following expression.

$$Q|_{f_s} = 0.5 f_s \left| \partial \Phi / \partial f \right|_{f_s} \quad (5.7)$$

Although the LN LVRs have a high k_t^2 and operate over a broad frequency range, note that only the Q at the resonance frequency has been extracted. It is believed that this is sufficient to describe the

impact of anchor losses on the resonator as they will not change significantly over the frequency range of interest.

5.2.2 Analysis of anchor losses as a function of resonator geometry

The anchor loss of the MEMS resonators can be minimized by many strategies, such as positioning the tethers at the nodal points of the vibration mode, using different materials for the supports and vibrating body (ensuring acoustic impedance mismatch), designing the tether length as an odd number of quarter-wavelength ($\lambda/4$) [47], reflecting the acoustic waves leaking via the tethers back into the resonant structure [48], [49], [50] or by confining the acoustic wave displacement far from the anchoring point [51].

In this section, the impact of the LN LVR geometry on support losses is analyzed via FEA. In particular, the following parameters have been considered for a fixed plate length and width: metalized bus width (W_b), gap width (W_g), anchor length (L_a) and width (W_a) (see Fig.5.4). The analysis shows that the gap width has a primary impact on Q_{anc} .

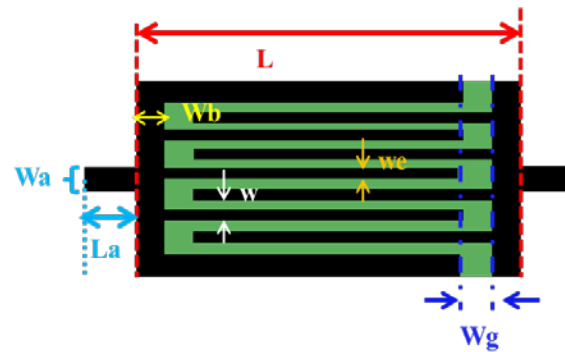


Fig.5.4. Top view of the LN LVRs' with geometric dimensions studied labeled

5.2.2.1 Impact of device geometry on support losses

According to wave propagation theory, acoustic waves travel in the cavity and are reflected at the boundaries. As shown in Fig. 5.3 (b), the left and right boundaries of the LN LVRs are free, so that the

traveling acoustic waves can be totally reflected back, whereas due to the bus electrodes and the tethers, the top and bottom boundaries are anchored to the substrate, hence letting energy escape through it and be dissipated in the substrate.

a) Support losses as a function of gap width

LN LVRs are piezoelectric resonators that excite lateral vibrations in LN plates. They are formed by a central active region and two inactive regions. The active region corresponds to the area where the electric field generates a mechanical strain through the equivalent d_{11} and d_{31} coefficient of the LN film. This region is composed of a center area of LN thin film covered by the top IDT electrodes which are alternatively connected to opposite voltage polarities and two gap regions of LN thin film activated by the fringing field introduced by the metalized bus portion and the tip of the IDT finger. Each inactive region corresponds to the area placed between one edge of the active region and the closest edge of the resonant plate. In this work we analyze the dependence of support losses on the size of the gap width, which is the active portion that is included between the metalized bus and the tips of the IDT fingers (Fig. 5.5). As shown in Figure 5.5, each gap region has no coverage of top metal.

Differently from the model for bus width optimization for AlN CMRs [47], the gap regions of LN LVRs are not considered to be inactive anymore since they are activated by the fringing field introduced by the metalized bus and the tips of the IDT fingers. Such electric field generates a mechanical strain through the equivalent d_{11} and d_{31} coefficient of the LN film which cannot be ignored due to their relative large magnitude (compared to the AlN film). Similarly to AlN, changing the gap width for a fixed plate dimension, modifies the length of the active area, hence also slightly modifying the main mode of vibration. We believe that these two physical mechanisms play a key role on the trends exhibited by the support losses as a function of W_g .

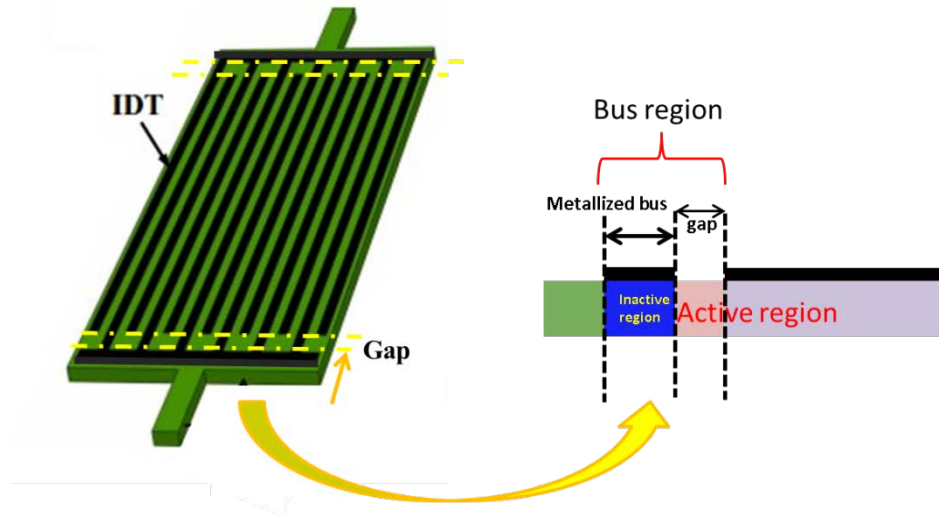


Fig.5.5. Schematic representation of the 500 MHz LN LVRs analyzed in this work (left), and the cross-sectional schematic(right) of the cross sectional view of the area indicated with the yellow dashed lines. The bus is formed by two different sections, each one colored differently, metallized bus(blue) and gap(pink). Blue and light purple sections are characterized by same mechanical properties as they are formed by LN and top metal layer. The green and pink sections are formed by standalone LN. Metal layers are made by aluminum. Metal thickness is about $0.1\mu\text{m}$. LN thickness is equal to $1\mu\text{m}$.

Different gap dimensions for a fixed vibrating plate size were modeled with PML. Anchors' width ($W_a=21\mu\text{m}$ and length ($L_a=22.5\mu\text{m}$) were also kept fixed were used as previously optimized for a gap value that showed a larger dependence on anchor dimensions (see 5.3.2.2 for $3\mu\text{m}$ gap size). The metallized bus width (W_b) was kept fixed at $1/2\lambda$, in this initial analysis (see table 5.3 for details on resonator geometry)

Table.5. 3. Dimensions of the LN LVRs adopted in COMSOL simulation for initial exploration

Quantity	Value
Full plate length (L)	$120\mu\text{m}$
Full plate width (W)	$60\mu\text{m}$
Electrode Pitch	$6\mu\text{m}$
Electrode width (W_e)	$2\mu\text{m}$
Gap width (W_g)	$3\mu\text{m}$
Top Al electrode thickness	100nm
Anchor width(W_a)	$21\mu\text{m}$
Anchor length(L_a)	$22.5\mu\text{m}$

The metallized gap's width (W_g) was varied as a function of the acoustic wavelength (λ) from $1/4\lambda$ to $13/8\lambda$. $\lambda/8$ increments were used (Fig.5.6). The range for W_g was identified based on the goal of eliminating spurious vibrations and minimizing fabrication challenges associated with very small features. We found out that the resonator Q (due to support loss) has a significant dependence on the the metallized gap's width (W_g). The Q values extracted from COMSOL FEA fluctuate from 490 to 20,698 depending on the gap's width. A plot of the Q value extracted from the simulation vs. gap width is shown in Fig.5.6. As illustrated in Fig.5.6, the Q due to anchor losses vs. W_g exhibits a peak for a very specific range of values of W_g . According to the FEM analysis, Q shows a peak for W_g in the range of $3/4\lambda$ and λ and then decays sharply for larger values of W_g . Simulation indicated that anchor losses can be dramatically minimized by properly sizing the gap region, which effectively determines the amount of energy flowing from the active region towards the anchors.

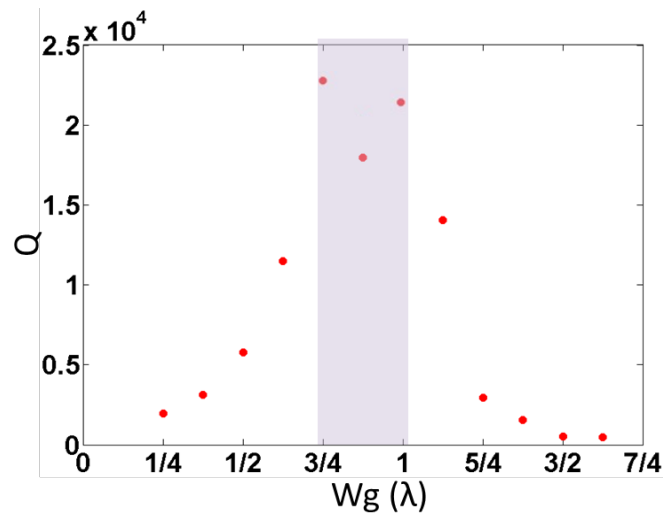
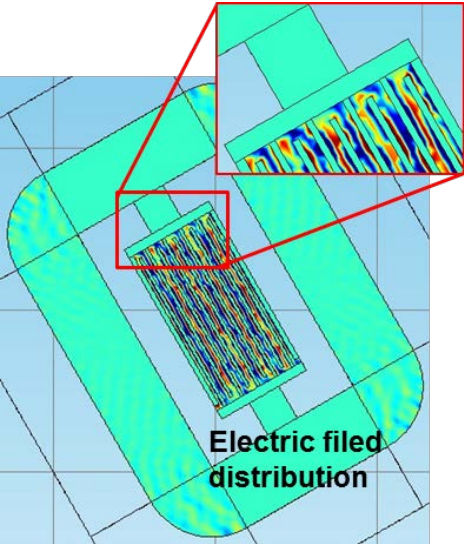


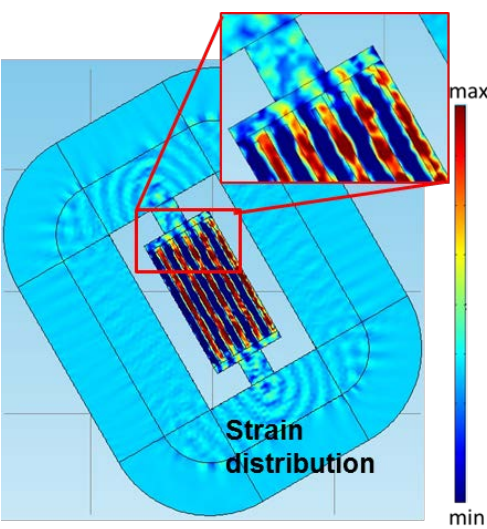
Fig.5.6. Scatter plot of Q due to anchor losses vs. gap width (W_g). Maximum value range is highlighted in light purple.

The electric field and strain distribution in the LN LVR has been modeled for different gap widths of $3\ \mu\text{m}$ ($1/4\lambda$), $9\ \mu\text{m}$ ($3/4\lambda$) and $18\ \mu\text{m}$ ($3/2\lambda$) and reported in Fig.5.7. The plots indicate that

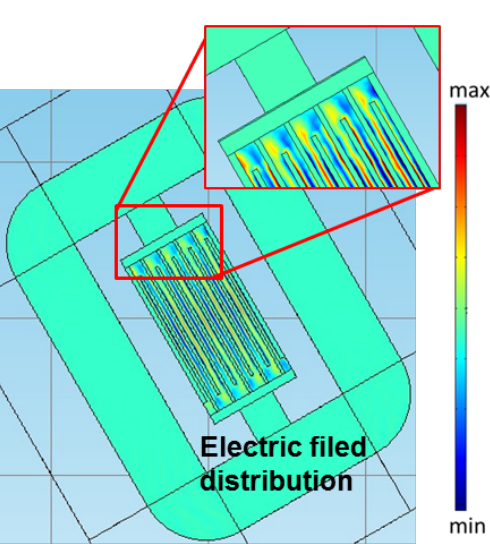
energy is coupled in the gap region and this activated region is directly connected with the metalized bus and anchor through which the energy is leaking.



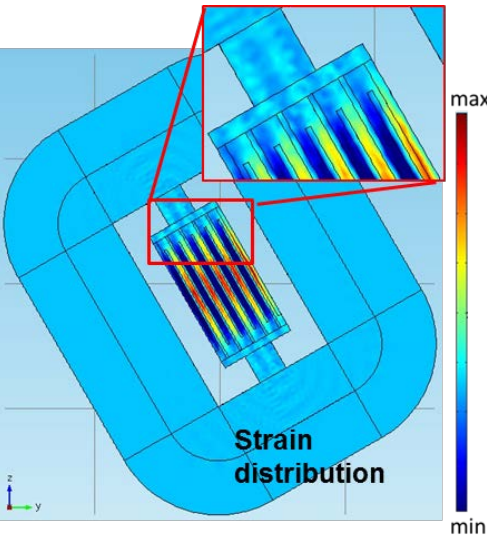
(a1)



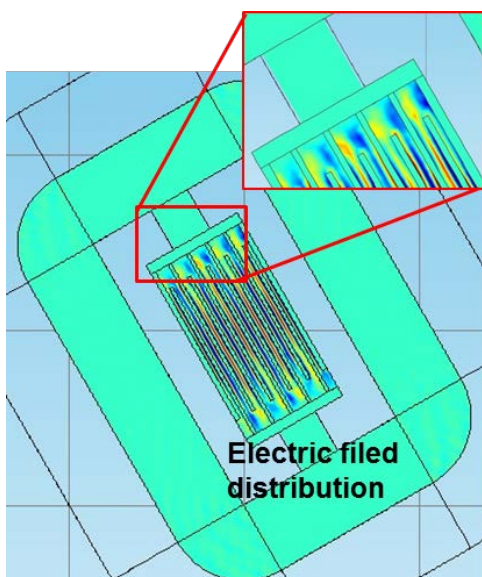
(a2)



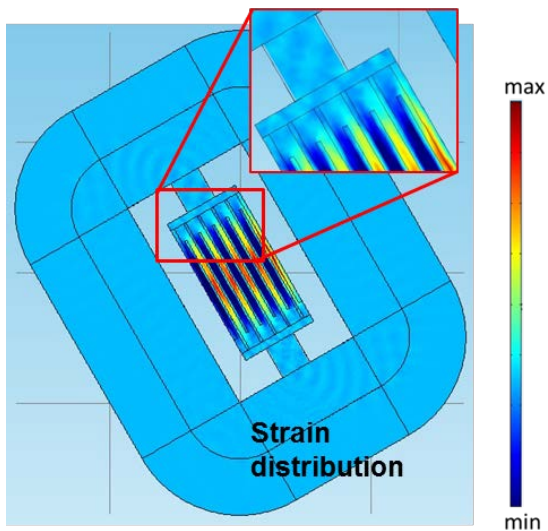
(b1)



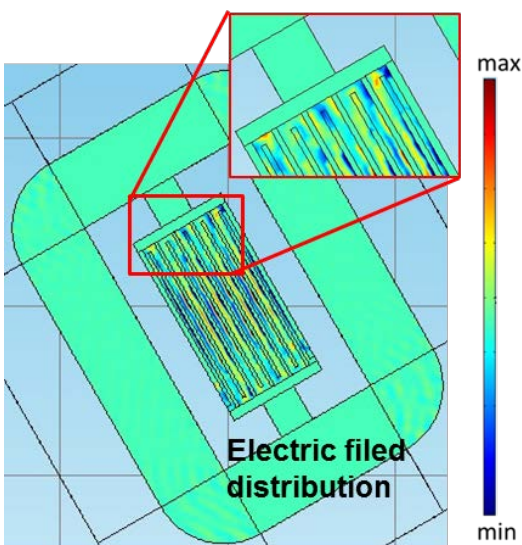
(b2)



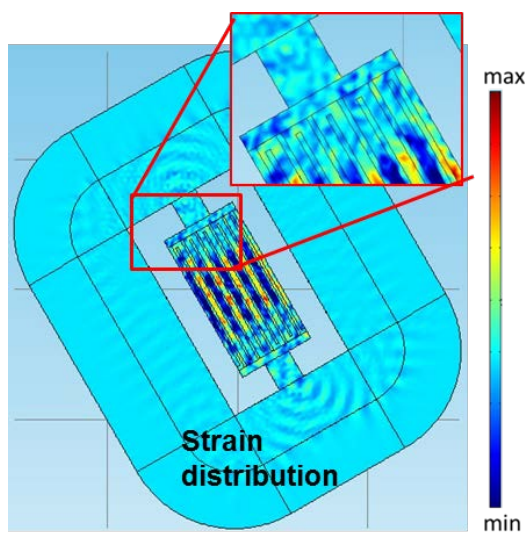
(c1)



(c2)



(d1)



(d2)

Fig.5.7. Electric field distribution in the LN LVRs with (a1) $Wg=1/4\lambda$ (b1) $Wg= 3/4\lambda$ (c1) $Wg= \lambda$ (d1) $Wg= 3/2\lambda$ with the gap region boxed in red zoom in, and Strain distribution in the LN LVRs with (a2) $Wg=1/4\lambda$ (b2) $Wg= 3/4\lambda$ (c2) $Wg= \lambda$ (d2) $Wg= 3/2\lambda$ with the gap region boxed in red zoom in.

Such behavior can be explained by hypothesizing that the energy leaking out of the resonant body in conjunction with the excitation of a transversal wave are the main factors determining the Q_{anc} and looking into the impact of the electrode length in exciting transversal modes. According to acoustic wave theory, the acoustic wave residing in the resonant plate includes the main resonance mode as well as the transverse mode. All these standing waves have to satisfy the following conditions:

$$W = \frac{n}{2} \lambda_x \quad L = \frac{m}{2} \lambda_y \quad (5.8)$$

where n and m are arbitrary positive integers, λ_x and λ_y are the wave length in the main mode propagation direction and corresponding in-plane perpendicular direction, respectively. The resonant frequency of the (n, m) modes can be expressed as the following

$$f_{n,m} = v_0 \sqrt{\left(\frac{n}{2W}\right)^2 + \left(\frac{m}{2L}\right)^2} = \frac{nv_0}{2W} \sqrt{1 + \left(\frac{mW}{nL}\right)^2} \quad (5.9)$$

where V_0 is the wave velocity of the coupled mode. W and L are the pitch width and length of the resonant plate of the LN LVR as labeled in Fig.5.7.

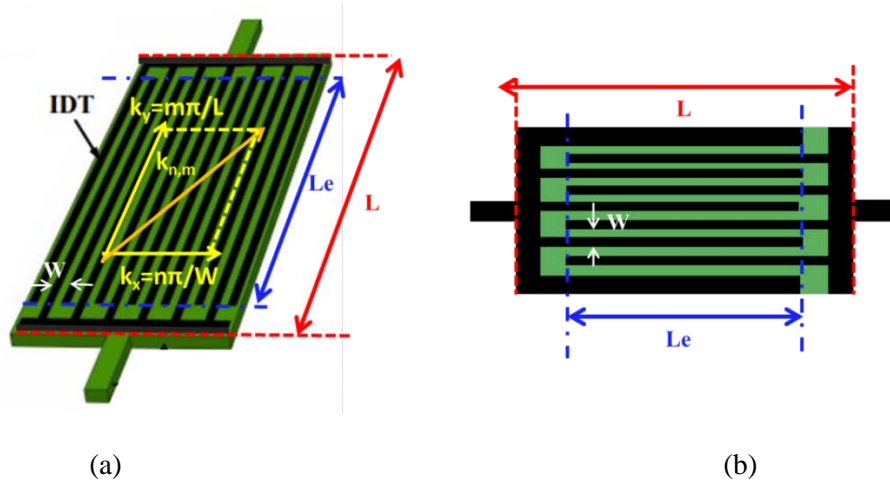


Fig.5.8. 3D mock up view(a) and top view(b) of the LN LVR under study. The characterisitic dimensions are labled and expressed in the same color and wave vector are expressed in yellow.

The $(1, 1)$ mode is defined as the fundamental mode. When m is larger than 1, and n remained 1, the excited $(1,m)$ modes are transverse modes. Observed from eq. (5.9), when L gets larger, the resonant frequencies of the transverse modes move closer to that of the main S_0 mode and verse versa. In either

case, these transverse spurious mode can be moved around by tuning the resonate plate length L so that the separation between each adjacent $f_{1,m}$ and frequency of main S0 mode can be enlarged or reduced.

Adapted from the model in [52], the k_t^2 of these transverse modes can be expressed by the following expression:

$$k_t^2 \approx \frac{\tilde{e}_{11}^2}{\tilde{c}_{11}\tilde{e}_{11}} \frac{(\int_s S_1 \Phi dS)^2}{(\int_s S_1^2 dS)(\int_s \Phi^2 dS)^2} \propto \frac{(\int_{\frac{L-L_e}{2}}^{\frac{L+L_e}{2}} A(x, y) \sin(\frac{m\pi}{L}y) \Phi dy)^2}{(\int_0^L A^2(x, y) \sin^2(\frac{m\pi}{L}y) dy)(\int_{\frac{L-L_e}{2}}^{\frac{L+L_e}{2}} \Phi^2 dy)} \propto \frac{\sin^2(\frac{m\pi}{2} \frac{L_e}{L})}{m^2 \frac{L_e}{L}} \propto \frac{1}{m^2} \quad (5.10)$$

Where S_1 is the strain, Φ is the applied voltage between the electrodes of different polarity; ϵ , c , and e are the permittivity constant, the elastic stiffness constant, and the piezoelectric stress constant, respectively and L_e is the effective finger length as shown in Fig.5.8. When $m = 3$ and $l_e = (2/3) L$, the k_t^2 of the third transverse mode becomes 0, indicating an elimination of this mode. It's also interesting to note that k_t^2 is inversely proportional to the order of the mode, m . The higher the order of the mode, the lower the coupling is.

In the case of gap width tuning with the resonant plate length being fixed, the effective finger length (L_e) varies and hence the coupling of the transverse modes, which can play a dominant role in setting energy leakage from the resonate body.

Moreover, such behavior can be further explained by looking into the origin of anchor loss which is related to a non-null displacement field at the anchors originated by the resonator active region. When the gap is narrow ($Wg \sim 3 \mu m$), the fringing electric field between the IDT tips and the metallized bus of the other polarity is large ($E=U/d$) and generates relatively large mechanical strain propagating toward the anchors, resulting in high energy escaping through the anchors. When the gap is enlarged ($Wg \sim 9 \mu m$), the fringing electric field become sparse and generate smaller mechanical strain propagating toward the anchors, as if a standing wave were generated between the metallized bus and the IDT edge. Hence less energy leaves the resonator body. When the gap is further increased ($Wg \sim 12 \mu m$), energy starts to propagate through the gap region and leave the resonator body. When the gap is very wide ($Wg \sim 18 \mu m$),

a combination of strong transversal modes and poor reflections between the bus and the edge of the active region likely result in a large amount of energy escaping through the anchors.

It is important to note that the large k_t^2 of LN LVRs is not impacted by the modification of the gap size. The k_t^2 extracted from the simulation with both $W_g = 3/4 \lambda$ and $W_g = \lambda$ gave simulated Q s due to anchor loss of 23,255 and 20,483 and k_t^2 greater than 30% for both cases (see Fig.5.9)

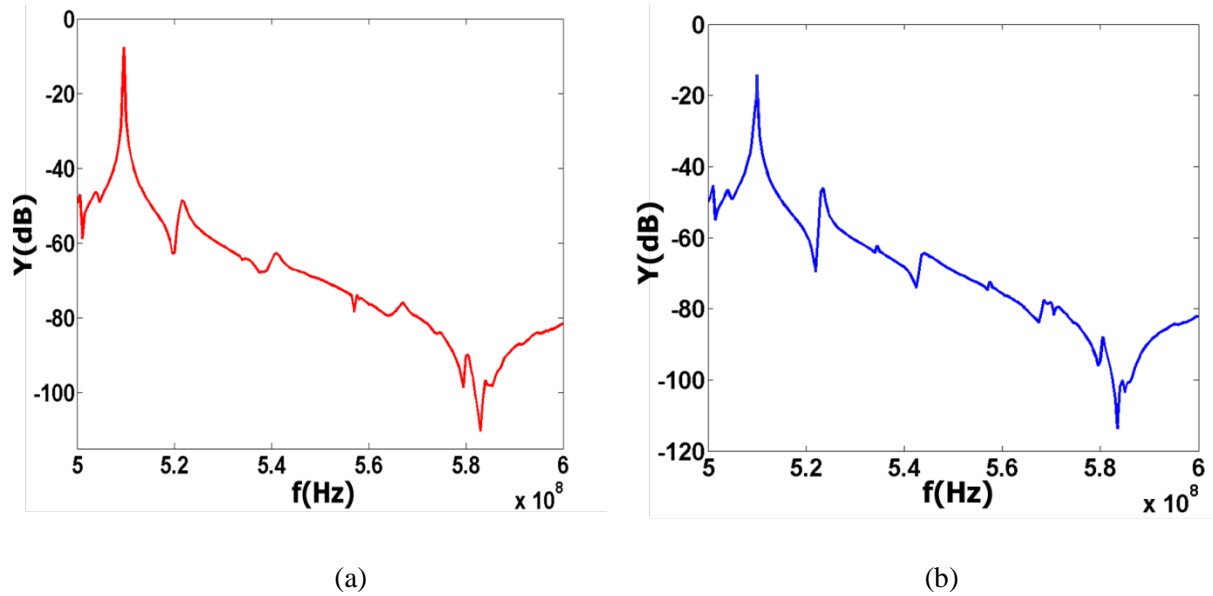


Fig.5.9. Frequency response for LN LVRs with W_g setting to be (a) $3/4 \lambda$ and (b) λ respectively simulated in 3D COMSOL FEM.

The simulation results were validated experimentally by building a series of devices with various W_g as employed in the simulation.

b) Impact of metalized bus width on support losses

As depicted in the previous section, the second portion composing the bus region is what is called the metalized bus (see Fig.5.5). The impact of different metalized bus dimensions on resonator Q was modeled with the previously presented PML method. The gap width is first set to be $3 \mu\text{m}$ to demonstrate the behavior of metalized bus in the case of a non-optimal gap width size. After establishing that is as a secondary role in setting the device, its impact on support losses with optimized values of W_g is reassessed. All other parameters are kept fixed as in the simulations for the gap width.

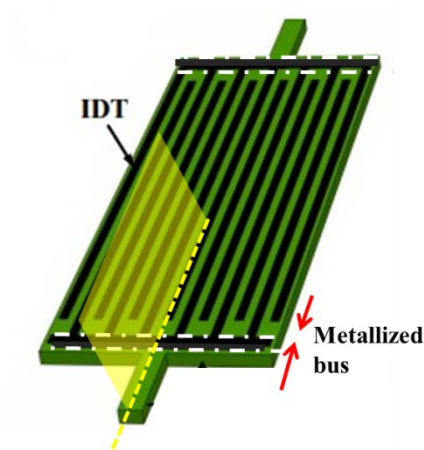


Fig.5.10. 3D mock up view of LN LVR with metallized bus area marked with arrows

When the gap width is set to be $3\text{ }\mu\text{m}$, the metallized bus's width (W_b) was varied as a function of the acoustic wavelength (λ) from $1/2\lambda$ to $3/2\lambda$. $\lambda/8$ increments were used (Fig.5.11). The range for W_b was identified based on the goal of eliminating spurious vibrations and minimizing fabrication challenges associated with very small features. The Q values extracted from COMSOL FEA fluctuate from 1010 to 2040 depending on metallized bus's width. A plot of the Q value is illustrated in Fig.5.11.

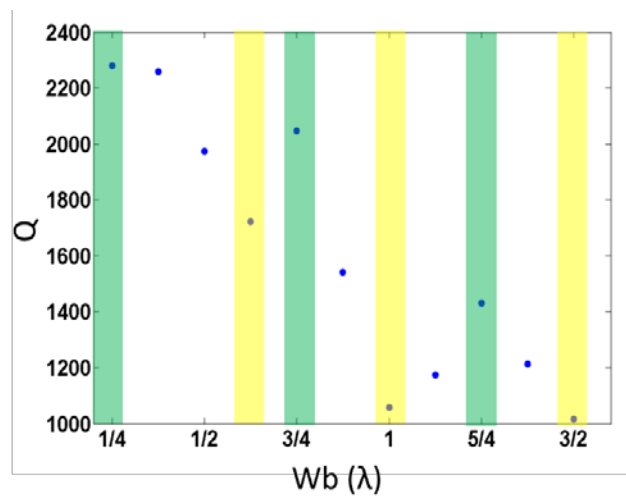


Fig.5.11. Plot of Q due to anchor losses vs. metallized bus width (W_b). Local maximum and minimum values are highlighted in green and yellow respectively.

The simulation results showed similar behavior with the bus optimization simulation results conducted with AlN CMRs in [53]. The simulation indicated that when the optimum anchor geometry is used, anchor losses can be further minimized by designing the bus size so that it either behaves as an acoustic $\lambda/4$ transformers or it could minimize the energy flowing from the active region towards the anchors. Peak values of Q were obtained when metalized bus width is set to be an odd number of $1/4 \lambda$.

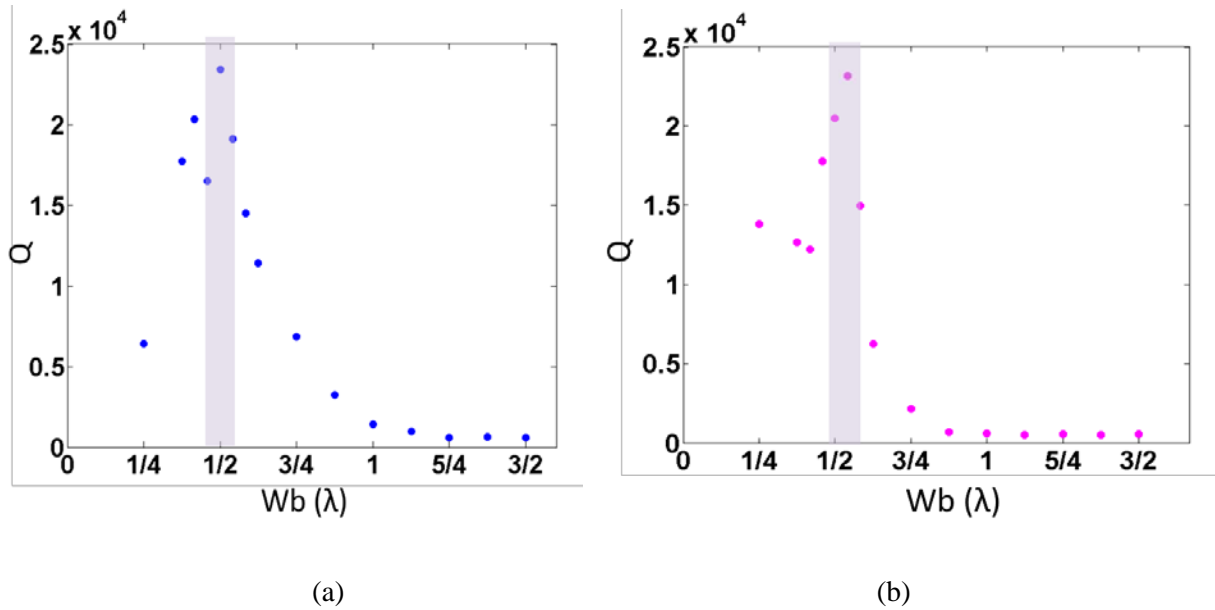


Fig.5.12. Scatter plot of Q due to anchor losses vs. metalized bus width (Wb when gap width is set to be (a) $9 \mu\text{m}$ (b) $12 \mu\text{m}$. Local maximum highlighted in light purple.

From the analysis on gap width, it is clear that much higher Q s could be attained by properly sizing the gap. It is therefore important to establish whether the Wb has any impact on the support losses when the gap width is set to be either $3/4\lambda$ and λ , which gave the highest Q in Fig.5.6. The metalized bus width was swept with COMSOL FEM to ensure that the metalized bus and gap combination ($Wb = 6 \mu\text{m}$, $Wg = 9 \mu\text{m}$) gave the maximum Q . The Q due to anchor losses vs. Wb plot was generated for the two optimized Wg cases respectively and shown in Fig.5.12. The metalized bus's width (Wb) was varied as a function of the acoustic wavelength (λ) from $1/2 \lambda$ to $3/2 \lambda$. $\lambda/8$ increments were used. A refined step amplitude of $1/24 \lambda$ was applied around main peaks to gain a better understanding of the simulated trends.

It is interesting to see how the bus behaves differently in the two cases. In the case in which $W_g = 9 \mu\text{m}$ ($3/4 \lambda$) the bus plus the gap form a mechanical region that is a multiple of $\lambda/4$. In the case in which $W_g = 12 \mu\text{m}$ (λ) the optimum bus size is $6.5 \mu\text{m}$ ($13/24 \lambda$), meaning that another physical phenomenon is likely to determine the device Q . Note that in the case of $W_g = 12 \mu\text{m}$ (λ) the 2nd highest Q value is recorded for $W_b = \lambda/4$, again confirming that the overall size of $W_b + W_g$ does play a role in setting the Q of the resonator as in the case of $W_g = 9 \mu\text{m}$.

5.2.2.2 Impact of anchor dimensions on support losses

From the previous analysis, it appears that the anchor dimensions play a secondary role in setting the Q of these devices. To ensure that it is the case, different anchor dimensions for a fixed vibrating plate size were modeled for both optimized and non-optimized metalized bus - gap pair.

For the case of non-optimized gap width, the gap width is set to be $3 \mu\text{m}$. The anchor's width (W_a) and length (L_a) were varied as a function of the acoustic wavelength (λ) from $5/4 \lambda$ to $9/5 \lambda$ and $11/8 \lambda$ to $19/8 \lambda$, respectively. $\lambda/8$ increments were used (Fig. 5.13). The ranges for both W_a and L_a were identified based on the goal of eliminating spurious vibrations and minimizing fabrication challenges associated with very small features. The Q values extracted from COMSOL FEA vary from 220 to 2400 depending on anchor dimensions. A contour plot of the Q value with the simulated points labelled in green is illustrated in Fig. 5.13.

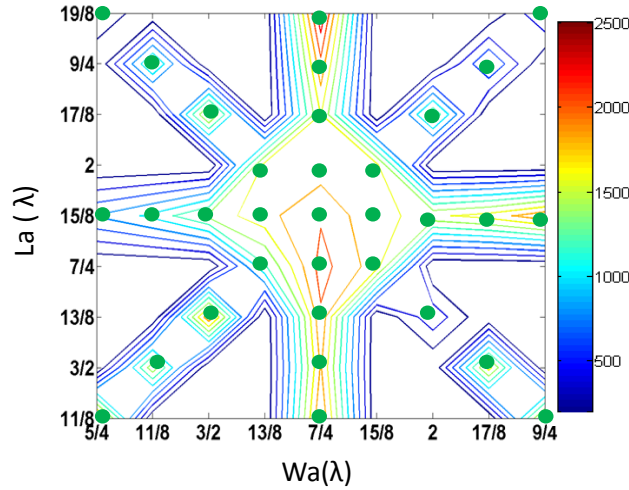


Fig.5.13. Contour plot of Q due to anchor losses vs. anchor geometry (W_a and L_a) with gap width set to $3 \mu\text{m}$. Green dots indicate actual values simulated in 3D COMSOL FEM. Contours are automatically generated by matlab and are used to guide the eye.

As shown in Fig.5.13, the maximum Q is obtained when both W_a and L_a are set to $7/4 \lambda$ simultaneously.

For the case of optimized gap width, the gap width is set to be 9 and 12 μm respectively. The metalized bus width is set to 6 μm according to the results in the previous section. To ensure that the best combination of anchor length and width had been considered for both cases, the anchor's width (W_a) and length (L_a) were swept around the set values used in the previous simulations to quantify their impact on the device Q . The anchor's width (W_a , previously set at $7/4 \lambda$) and length (L_a , previously set at $15/8 \lambda$) were varied as a function of the acoustic wavelength (λ) from $13/8 \lambda$ to $15/8 \lambda$ and $3/2 \lambda$ to 2λ , respectively. $\lambda/8$ increments were used (Fig. 5.14). By sweeping the anchor parameters in COMSOL we found that the Q values vary from 14,000 to 26,000 when the gap width equals 9 μm and 10,000 to 20,000 when the gap width equals 12 μm (W_b was set to $\lambda/2$ in this analysis). The simulations results indicate that once the gap and metalized bus width are optimized, the sizing of the anchors becomes equally critical for anchor loss minimization. A contour plot of the Q value with simulated points labelled in green is illustrated in Fig.5.13. The overall highest Q value was achieved when $W_a = 19.5 \mu\text{m}$, $L_a = 22.5 \mu\text{m}$ and $W_g = 9 \mu\text{m}$.

As for as the anchor sizing is considered, different anchor sizes are required for the two case of W_g and the anchors are not multiple of $\lambda/4$ in the two cases. It is suspected that this is possibly due to differences in the wave velocity between the metalized and non-metalized regions as well as the non-isotropic properties of LN.

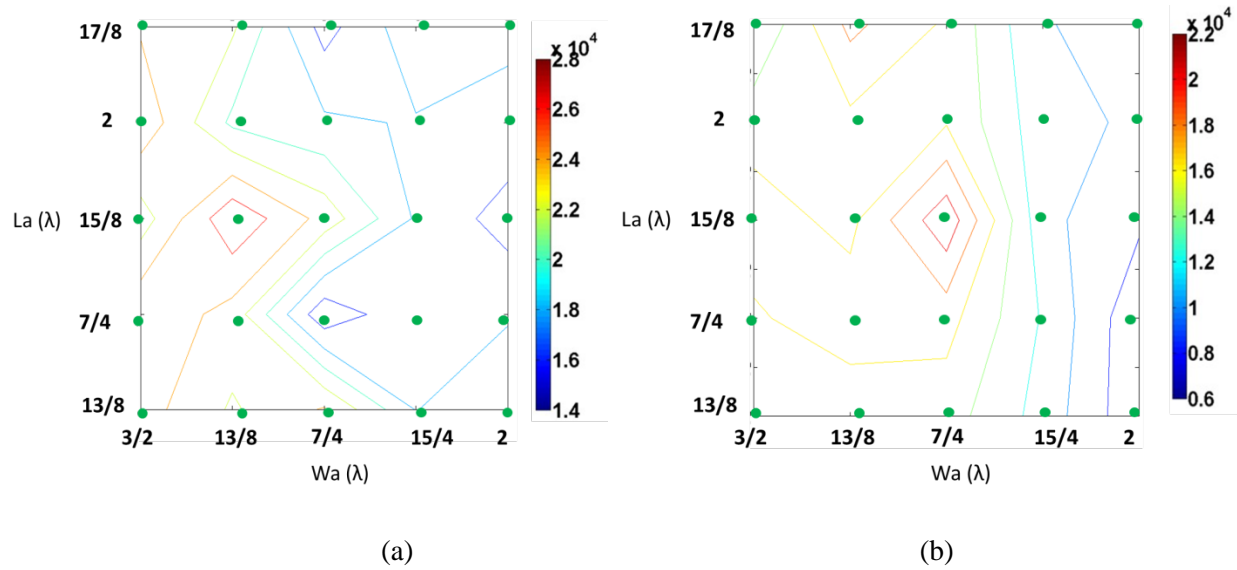


Fig.5.14. Contour plot of Q due to anchor losses vs. anchor geometry (W_a and L_a) with gap width set to (a) $9 \mu\text{m}$ and (b) $12 \mu\text{m}$. Green dots indicate actual values simulated in 3D COMSOL FEM. Contours are automatically generated by matlab and are used to guide the eye.

The geometry of an optimized resonator (for a specific gap value) are shown in Fig. 5.15 and listed in table 5.4 respectively.

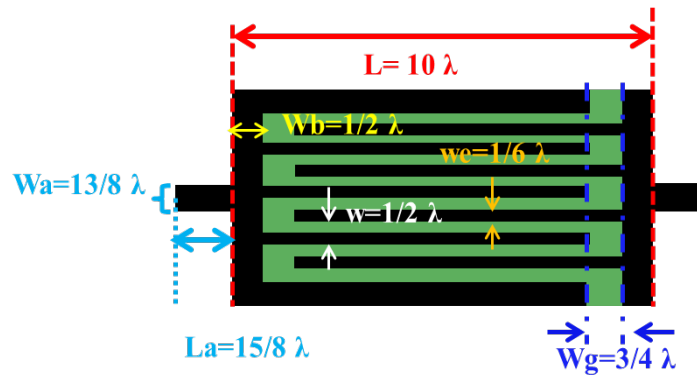


Fig.5.15. top view of the LVR geometry with the optimized dimension labeled as a function of the acoustic wavelength (λ)

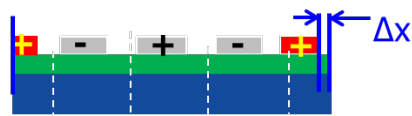
Table.5. 4. Optimized dimensions of the LN LVRs with COMSOL FEM

Quantity	Value
Full plate length (L)	120 μm (10λ)
Full plate width (W)	60 μm (5λ)
Electrode Pitch (w)	6 μm ($1/2 \lambda$)
Electrode width (we)	2 μm ($1/6 \lambda$)
Metalized bus width (Wb)	6 μm ($1/2 \lambda$) ⁴
Gap width (Wg)	9 μm ($3/4 \lambda$)
Anchor width (Wa)	19.5 μm ($13/8 \lambda$)
Anchor length (La)	22.5 μm ($15/8 \lambda$)

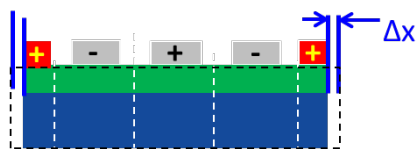
5.2.3 Non-ideality

The impact of fabrication on non-ideality (such as overetching and misalignment see Fig. 5.16) were analyzed for the specific optimized design shown in Table 5.4. Amplitude of over-etching and misalignment was swept from 0.1 μm ($1/120\lambda$) to 0.3 μm ($1/40\lambda$) in increments of 0.1 μm in both simulations. The frequency response of LN LVRs with 9 μm , 10.5 μm and 12 μm gap width subjected to the same amplitude of misalignment up to 0.3 μm ($\lambda/40$) were simulated and Fig.5.17 (a) shows the impact of such misalignment on Q . The analysis shows that LVRs with different gap widths (9 μm , 10.5 μm and 12 μm gap width) exhibit similar sensitivity to misalignment. The slope of the 3 Q vs. misalignment curves in Fig.5.17 (a) are similar except for few points. In the case of gap width set to 10.5 μm , misalignment of 0.1 μm boost the Q around 20% rather than degrading it. The Q for LVRs with 3 different gap widths maintained to be around 60% of original value with misalignment levels below 0.3 μm ($\lambda/40$). Successively, different levels of over-etching were simulated to reveal the robustness of LVR that use different gap widths (Fig.5.17 (b)). As shown in Fig.5.17 (b), the analysis demonstrate that LVR with 9 μm gap width demonstrate the most stable Q once subjected to over-etching. The Q practically changes within 25% with over-etching varying from 0.1 μm ($\lambda/120$) to 0.3 μm ($\lambda/40$). When the gap width of the LN LVR is increased from 9 μm all the way up to 12 μm , Q becomes more and more

sensitive to over-etching. The Q for all the gap widths from 9 μm to 12 μm is minimally affected by over-etching below 0.1 μm ($\lambda/120$).



(a)



(b)

Fig.5.16. (a) Block view for misalignment by Δx (b) Block view for over-etching by Δx

Table.5. 5. Summary of simulated quality factor (Q) for the resonators of all the same design but different gap width subjected to (a) different amplitude of over-etching (b) different amplitude of misalignment

(a)

	Simulated Q value with misalignment (μm)			
Gap width(μm)	0	0.1	0.2	0.3
9	23255	21648	19449	14397
10.5	17965	21725	15605	14084
12	20483	18953	15881	13563

(b)

	Simulated Q value with over-etching (μm)			
Gap width(μm)	0	0.1	0.2	0.3
9	23255	20360	20849	18585
10.5	17965	16571	9215	10090
12	20483	22906	5827	8289

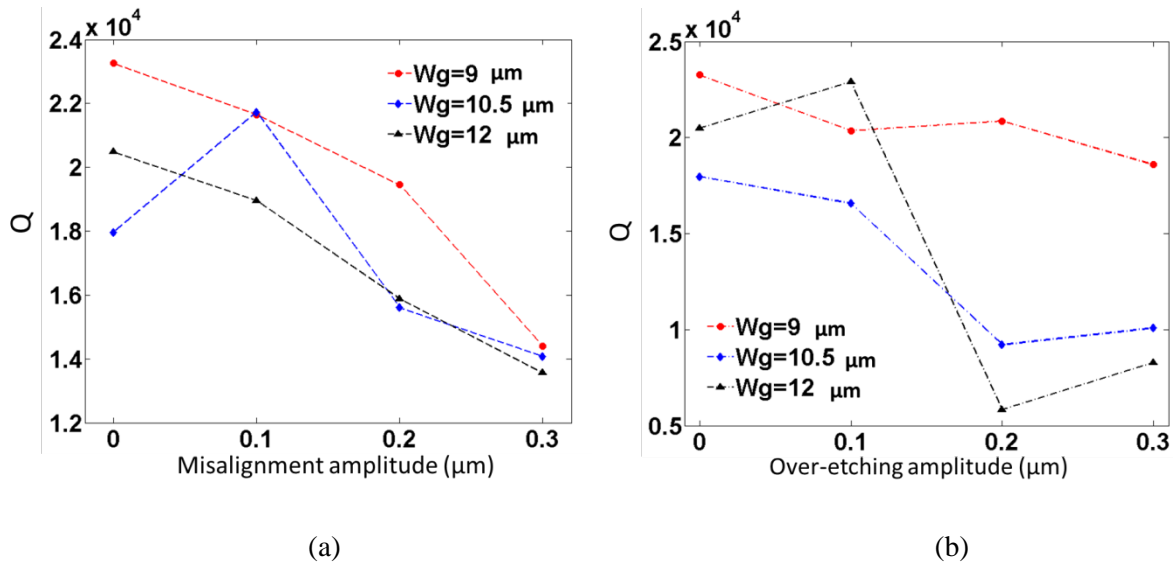
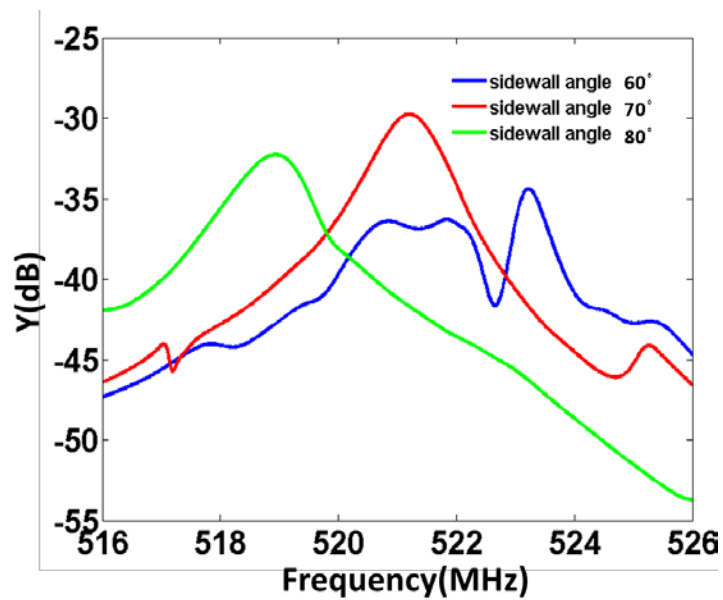
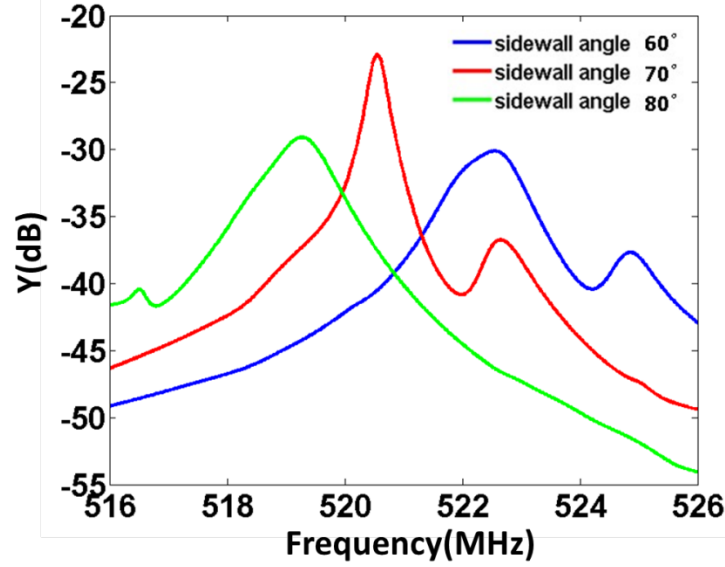


Fig.5.17. Plot of simulated Q value for various gap width(W_g) with different amplitude of (a) misalignment and (b) over-etching

Furthermore, the impact of a non-ideal side wall angles was also explored via FEA (frequency response analysis) on the same resonator geometry. The sidewall angle was varied between 60° and 80° in increments of 10° . Simulation indicated that non-ideal sidewalls would introduce peak splitting and spurs around resonance peak (see Fig.5.18).



(a)



(b)

Fig.5.18. Plot of simulated frequency response around the resonance peak for (a) 9 μm gap width(W_g) and (b) 12 μm gap width(W_g) with different amplitude of non-ideal sidewall angles

5.3 Design of experiment and experimental verification of impact of resonator geometry on Q

The impact of the device geometry on support losses was experimentally verified by fabricating more than 300 devices operating around 500 MHz and incorporating the active reflector design introduced in the previous chapter. We hypothesize that energy losses in LN LVRs operating at 500 MHz can be primarily attributed to anchor losses (Q_{anc}) and thermoelastic dissipation (Q_{ted}) in the electrodes (LN itself shows very little dissipation due to TED as calculated according to [38]) as for the case of AlN CMRs. Based on our findings on air damping and the use of the analytical equations in Table 5.1, we can reduce equation (5.1) to the following:

$$\frac{1}{Q} = \frac{1}{Q_{TED}} + \frac{1}{Q_{anc}} \quad (5.3)$$

With the aim of validating the trends shown by the COMSOL FEA for Q_{anc} we tested the resonators operating at 500 MHz at both room (300 K) and cryogenic (10 K) temperatures. Under the assumption that only TED is impacted by temperature, it is therefore possible to more clearly identify the impact of anchor losses on the resonator Q . In the limit, at extremely low temperature, the Q will be effectively determined by Q_{anc} .

The resonators were fabricated on both full wafer substrates with 1 μm LN thin film (3" dimension) bonded to a LN carrier wafer (4" dimension) through 2 μm SiO_2 from Nano-LN (Fig.5.19) and full wafer substrates with 1 μm LN thin film (4" dimension) bonded to a Si carrier wafer (4" dimension) from NGK (Fig.5.20). The vibrating body of the resonator was formed by a 1 μm -thick LN plate with 100nm-thick Al electrodes (top only). The devices fabricated with two platforms exhibited a series resonance at slightly different frequencies, being 497 MHz for Nano-LN and 543 MHz for NGK ones respectively corresponding to the S_0 mode of vibration displayed by the same LN plate of 60 μm width ($\lambda=12 \mu\text{m}$) and 120 μm length. Active reflectors that resort to 100% metal coverage of the $\lambda/4$ extensions are selected to achieve a considerable improvement of k_t^2 , spurious mode suppression, and robustness to processing including misalignment and over/under-etching (see section 6.3.1).

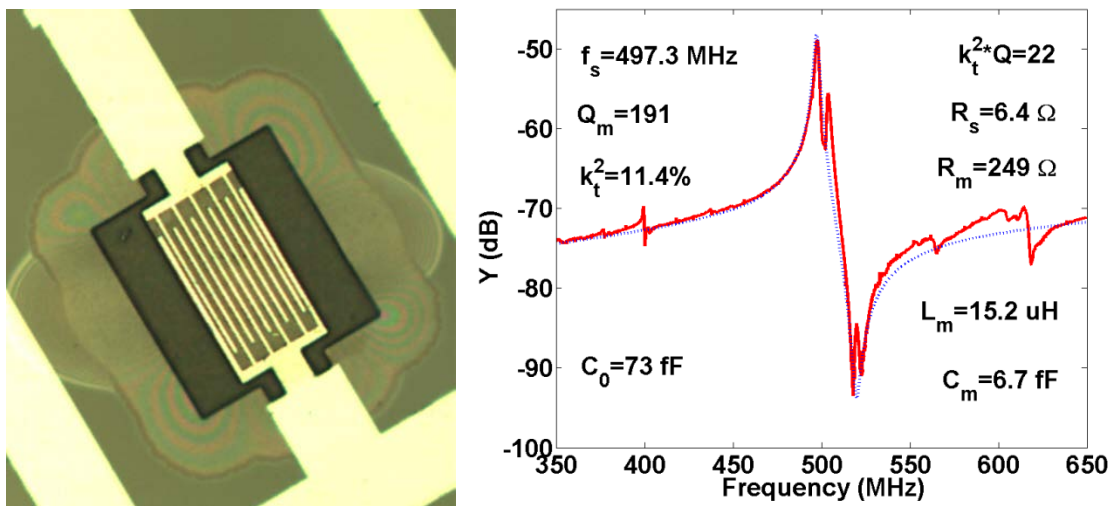


Fig.5.19. Optical image of a 497.3 MHz LN LNR fabricated with Nano-LN sample and the measured and fitted admittance response.

The devices fabricated with the NANO-LN wafer exhibited a misalignment of $0.2\ \mu\text{m}$ in the wave propagation direction and no visible misalignment in the direction perpendicular to wave propagation. Although the acoustic boundaries of the devices fabricated are accurately defined, all the devices demonstrated a low Q of approximately 200 and k_t^2 approaching 10% (much lower than the value predicted by COMSOL FEM). It is suspected to be originated from LN thin film being attacked by VHF during release step since other researchers have shown high Q in a similar sample from the same vendor by using a different release process [54]. The experimental Q vs. designed geometrical dimensions' variation are extracted and demonstrated in experimental results sections in detail but are not used to evaluate the impact of anchor loss on devices' overall Q due to the low Q value obtained and the minimum differentiation of Q for different designs.

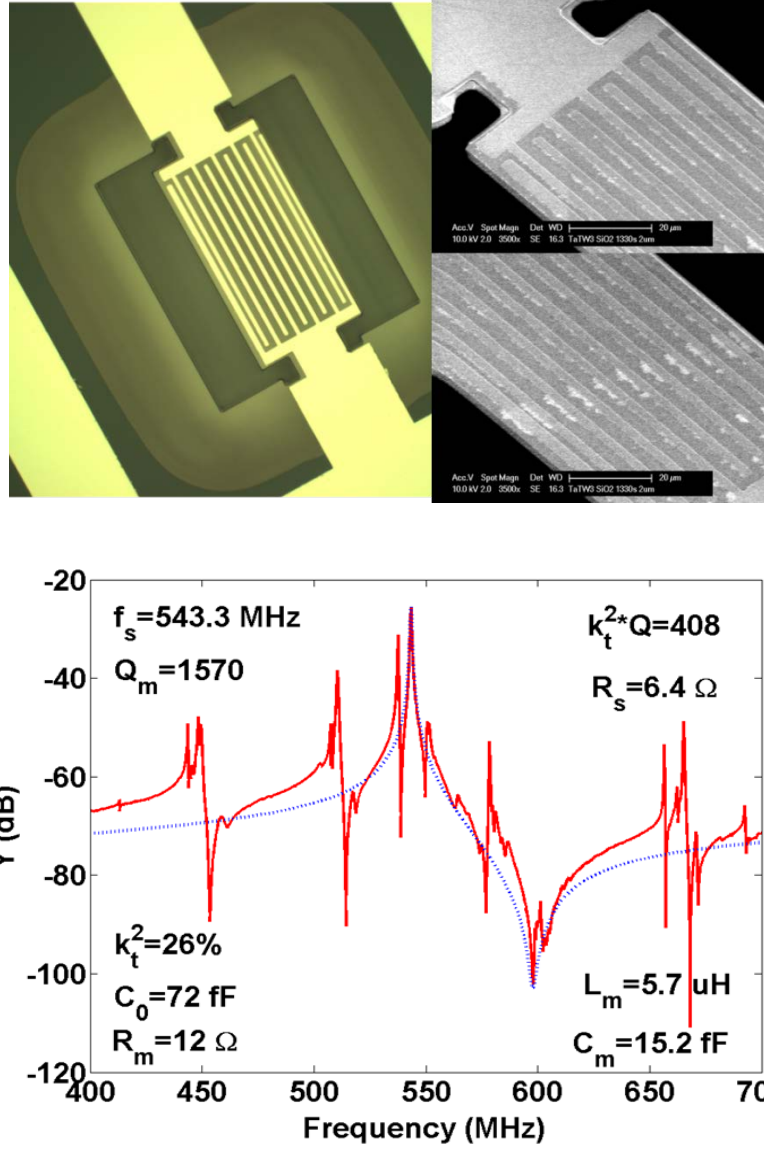


Fig.5.20. Optical image of the 543 MHz LN LNR, and zoomed in view of the anchor and IDT part in SEM fabricated with NGK sample and the measured and fitted admittance response

The devices fabricated with the NGK wafer exhibited an average misalignment of $0.8 \mu\text{m}$ in conjunction with an under-etching of $0.8 \mu\text{m}$ in both directions. The exact magnitude of misalignment and under-etching varies from one device to the other due to a small rotation error. Despite the relative large misalignment and under-etching, all the devices demonstrated Q varying from 400 to 1500 and k_t^2 of approximately 25%. Therefore, the experimental Q vs. designed geometrical dimensions' variation are

extracted and used to evaluate the impact of anchor loss on devices' overall Q and validate the resonator design optimization in order to minimize anchor loss.

Note that in the following sections, only the unloaded Q of the resonators (Q_u) are compared so as to exclude the impact of electrical loading (Q_{elec}). Q_u was obtained by eliminating the impact of electrical losses in the pads and metal electrodes through characterization and calculation of the resistance of electrode material on the chip. Note that electrical losses in the pads can be made arbitrarily small by increasing the metal thickness. Metal electrode losses cannot be reduced in this way (as electrode thickness generally plays a role in setting the resonator Q), but can be made considerably small by properly designing the resonator.

a) Experiment 1: Q as a function anchor, bus, and gap dimensions at 300 K

The impact of anchor losses in determining the overall value of Q is studied by collecting experimental data over a total of 318 LN LVRs working at 500 MHz from one of the chips fabricated with LN/SiO₂/LN stack (2nd generation devices) and one of the chips fabricated with LN/Si stack (3rd generation devices). For the fixed frequency and LN plate geometry (60x120 μm^2), 6 different metal covered bus widths (W_b) (4.5 μm , 6 μm , 7.5 μm , 9 μm , 10.5 μm and 12 μm) as well as 8 different (W_g) gap widths (3 μm and 6 μm to 15 μm in the increment of 1.5 μm) were implemented respectively to validate the simulation trend in Fig.5.7 and Fig.5.11. 12 different combinations of the anchors' width (W_a) and length (L_a) (same anchor design as represented by green dots in Fig.5.7 and Fig.5.11) were implemented to verify the simulation in Fig.5.14 for optimized gap width being 9 μm and 12 μm respectively.

All these configurations were tested on 2 different chips belonging to full wafer substrates with 1 μm LN thin film (3" dimension) bonded to a LN carrier wafer (4" dimension) through 2 μm SiO₂ from Nano-LN and full wafer substrates with 1 μm LN thin film (4" dimension) bonded to a Si carrier wafer (4" dimension) from NGK respectively. Effectively, 6 repetitions (3 for each chip) were measured for each layout to ensure a minimum level of statistics for each device. To extract the electrical response

(admittance) of the resonators a VNA was used and the values of Q_m were directly calculated as the ratio $f_r/\Delta f_{-3dB}$. To remove the impact of electrical loading (Q_{elec}) we compared the unloaded Q_s of the resonators (Q_u) that were calculated as:

$$Q_u = \frac{Q_m}{1 - \frac{R_s}{R_m + R_s}} \quad (5.4)$$

where R_m is the equivalent motional resistance and R_s is the series resistance which is calculated using equation (5.5). $R_m + R_s$ is extracted experimentally at resonance as the inverse of the admittance value at resonance frequency while R_s is calculated with the following expression according to [55]:

$$R_s = R_{pad} + R_e = R_{pad} + \frac{4}{3} \frac{\rho_e}{n} \frac{L}{W_e h_e} \quad (5.5)$$

where n is the number of fingers. ρ_e , W_e , L and h_e are the sheet resistance, width, length and thickness of the electrodes, respectively.

b) Experiment 2: Q dependence on temperature

To determine the Q dependence on temperature we performed a test on 3 equivalent resonators of optimized design (as listed in table 5.4) working at 500 MHz from one of the chips fabricated with LN/Si stack (3rd generation devices).

The experiments were performed on a cryogen-free micro-manipulated probe station (model CRX-VF Lakeshore) that allowed us to lower the temperature down to 10.5 K and study the resonator response at that temperature and at 300 K. The chamber pressure was maintained at 28 nTorr during low temperature (10.5 K) experiments.

Table 5.6 reports the Q_u recorded from 3 identical devices with optimized configuration (summarized in table 5.4) at 10 K and 300 K.

Table.5. 6. Measured Q_u from a sample of 3 equivalent resonators of the optimized design around 540 MHz at two temperatures: 10.5 and 300 K.

Equivalent optimized device	Q_u measured 300 K	Q_u measured 10.5 K
1	2317	5844
2	2438	8235
3	2279	1599 (Peak splitting observed)

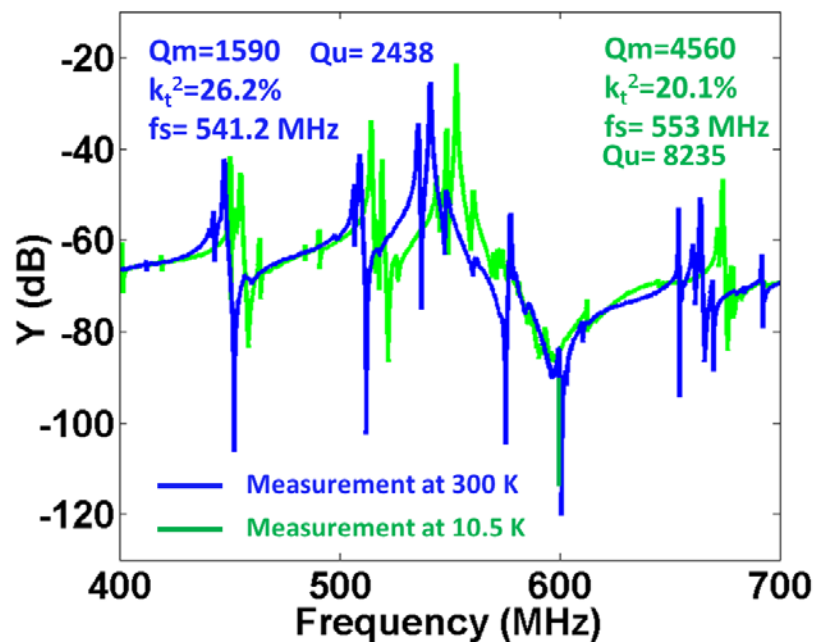
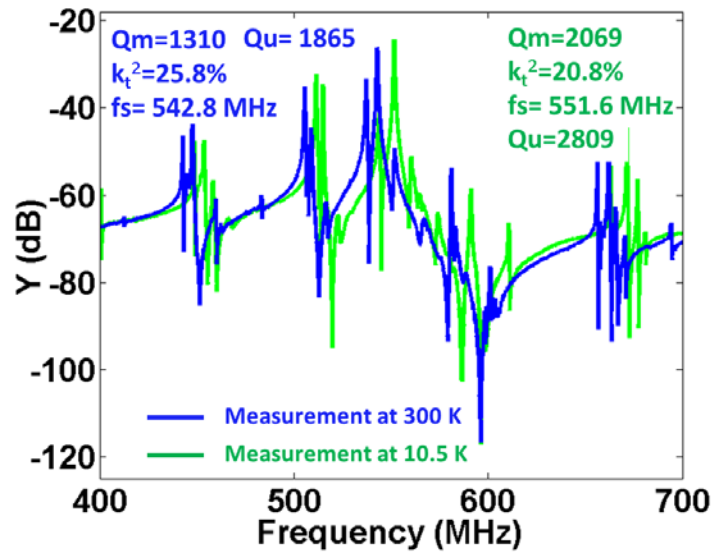


Fig.5.21. Comparison of the measured admittance responses of the S0 mode of the optimized designed LN LVR demonstrating the highest Q (10 120 μm long fingers of design Type A1) measured at room temperature, ambient air and 10.5 K, 28 nTorr.

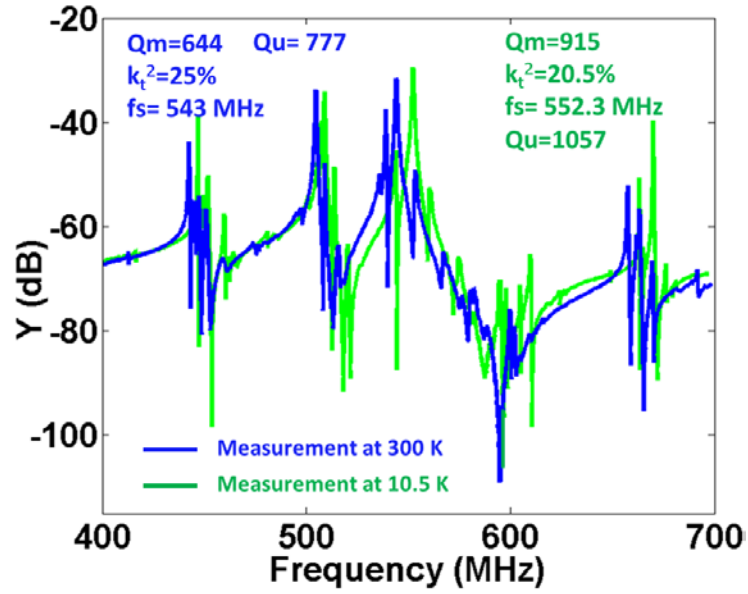
The experiments have validated our hypothesis that Q of resonators operating at 500 MHz is partially affected (at ambient conditions) by anchor losses (Q_{anc}) and an additional damping mechanism of thermodynamic nature likely related to thermoelastic dissipation (TED) (Q_{ted}).

As it is shown in Fig.5.21, the optimized designed LN LVR demonstrated more than 3X variations of Q_u with temperature. This variation essentially indicates that for the optimized designed LN LVR, the energy lost through the anchors at 300 K, is smaller than the amount dissipated through another mechanism of thermoelastic nature.).

As it is shown in Fig.5.22, the non-optimized designed LN LVR with gap width set to $6\text{ }\mu\text{m}$ demonstrated less than 60% variations of Q_u with temperature and the one with gap width set to $3\text{ }\mu\text{m}$ demonstrated less than 50% variations of Q_u with temperature. The variation in Q is significantly lower when compared to the one shown Fig.5.21. This experiment indicates that the energy loss due to anchors associated with the non-optimized designed of LN LVR is large, as in theory anchor losses should exhibit very limited temperature dependence. These results essentially prove that anchor losses are limiting the Q at room temperature if the support and device geometry is not properly designed, but can be made small when the resonator geometry has been optimized. Nonetheless, anchors still have an impact in setting the device Q at room temperature even in optimized geometries and hence similar trends to the one simulated by FEA can be revealed experimentally at room temperature. Such trends would more closely match the FEA if all measurements had been performed at cryogenic temperature.



(a)



(b)

Fig.5.22. Comparison of the measured admittance responses of the S0 mode of the non-optimized designed LN LVR with gap width(W_g) set to (a) $6\ \mu\text{m}$ and (b) $3\ \mu\text{m}$ (both are $10\ 120\ \mu\text{m}$ long fingers of design Type A1) measured at room temperature, ambient air and 10.5 K, 28 nTorr.

5.3.1 Experimental results

The sheet resistance value of the sputtered AlSiCu used as the top electrode for the LN LVRs was extracted by measuring the test structure of sheet resistance patterned on the LN surface. Linear regression was used to fit the measurement of the resistance of 8, 12, 16 and 20 $500\ \mu\text{m}$ long, 100nm thick and $10\ \mu\text{m}$ wide lines. Resistivity value is calculated according to the equation 5.6.

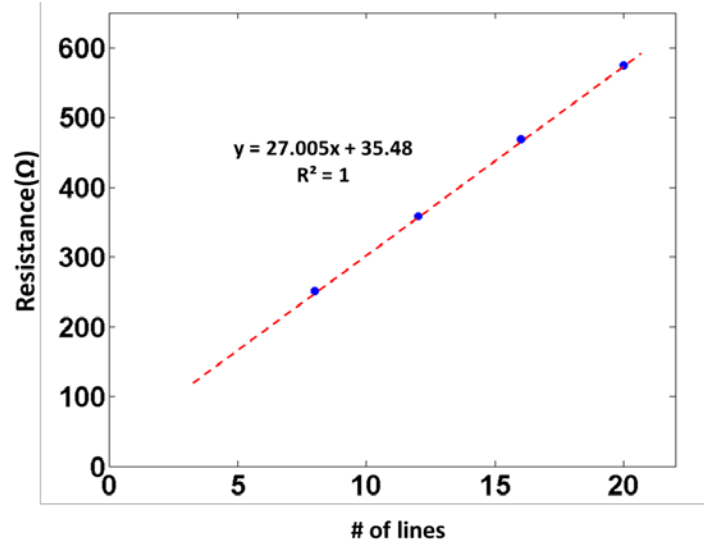


Fig.5.23. Linear fitting for aluminum line resistance measured from test structures of different lengths

$$\rho_e = R_{1-line} \frac{A_l}{L_l} = R_{1-line} \frac{W_l h_l}{L_l} \quad (5.6)$$

Where ρ_e , W_l , L_l and h_l are the resistivity, width, length and thickness of the lines in the test structure, respectively. The R_{1-line} value was 27 Ω based on the fitting of the measurement. The resistivity calculated was $5.4 \times 10^{-8} \Omega m$.

The resistance of the pads and the routing (R_{pad}) is separately measured on 3 independent test structures of the same dimension (see table) and the average is found to be 3.06 Ω .

Table.5. 7. Summary of measurement of R_{pad}

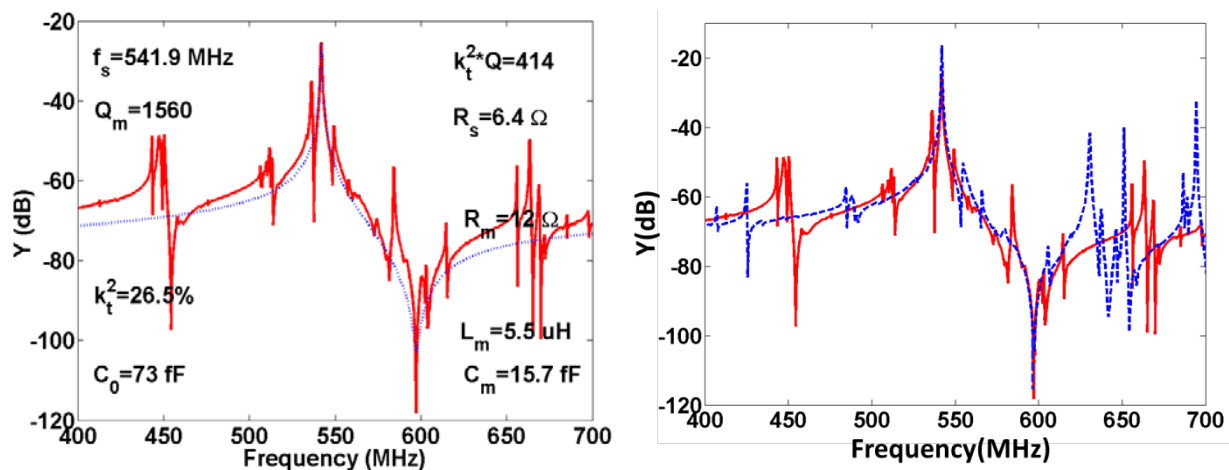
Frame resistance 1(Ω)	Frame resistance 2(Ω)	Frame resistance 3(Ω)	Frame resistance AVE(Ω)
3.06	2.99	3.145	3.06

The R_s value for different resonator configurations can be calculated according to Equation 5.5 and used to extract Q_u for the different devices.

Furthermore, since the devices fabricated with NGK sample demonstrated a considerable misalignment together with an under-etching, the impact of such combination of non-ideality on k_t^2 and

spurious mode was evaluated with COMSOL FEM. The LN LVR demonstrating the best performance (highest FOM) (Fig.5.24 (a)) was imaged and measured. Misalignment of $0.6\ \mu\text{m}$ together with an under-etching of $0.6\ \mu\text{m}$ in both directions was recorded in the fabricated devices. The frequency response of the device with the same magnitude of misalignment and under-etching applied was simulated and compared with experimental response as shown in Fig.5.24 (b). The COMSOL simulated response was shifted up by 42.1 MHz to fit the measured response (the reason for such shift in frequency is not well understood, but it is likely related to different material properties). The k_t^2 predicted by COMSOL matched well with experimental results. It is clear that not all spurious modes have been captured by the 3D simulation. Further analysis and more accurate definition of the boundary conditions as well as material properties is required to study all the spurious modes present in these highly misaligned and under-etched devices.

Besides, as detailed in section 5.2.3, the presence of misalignment greatly degrades device Q . Such deleterious effect grows as the amplitude of misalignment increases. The Q extracted from the COMSOL FEM analysis (conducted using PML boundaries) for the same device shown in Fig. 5.24 is 3,861, which is greatly degraded compared to the Q extracted for the ideal case shown in 5.2.3 (note that the frequency sweep of this specific simulation was done in increments of 0.2 MHz, which might have also subdued the value of the simulated Q). Therefore, it is believed that a higher Q will be achievable with more accurate definition of the boundaries of the designed LN LVRs during fabrication.



(a) (b)

Fig.5.24. (a) The measured and fitted admittance response of a standalone LN LVR vibrating at 500 MHz (10 μm long electrodes and, 6 μm pitch with 2 μm metal strip, placed at -60° to the z axis in X-cut plane) of active reflector design with 100% coverage. (b) The comparison of the measured (in red) and 3D COMSOL simulated responses (in dashed blue) (misalignment of 0.6 μm and over etching of 0.6 μm) for the same devices are shown in the zoomed-in plots on the right. COMSOL simulated responses was shifted 42.1 MHz up to fit the measured response.

5.3.1.1 Gap optimization

The impact of gap width in determining the anchor losses is studied by collecting experimental data over a total of 48 LN LVRs from Nano-LN and NGK sample respectively. For the fixed frequency and LN plate geometry (60x120 μm^2), 8 different (Wg) gap widths (3 μm and 6 μm to 15 μm in the increment of 1.5 μm) were implemented respectively to validate the simulation trend in Fig.5.11. A VNA was used to record their electrical response (admittance) and their loaded Q_m were extracted as the ratio f_r/f_{-3dB} . To remove the impact of electrical loading we compared the unloaded Q_s of the resonators (Q_u) that were computed by using equation (5.4).

As for the Nano-LN sample, the results are shown in Fig.5.25 without comparison to the FEM curve as little variations were found.

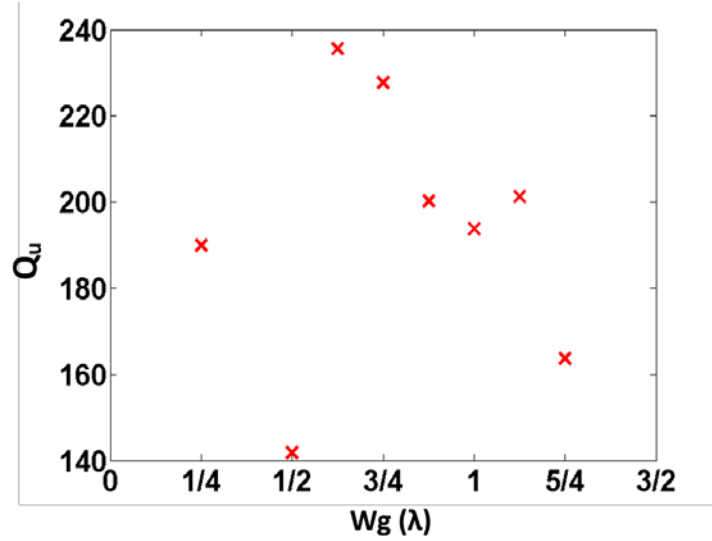


Fig.5.25. Average experimental measurements of Q vs. gap width with $Wb=6\ \mu\text{m}$.

As for the NGK sample, the statistics of data collected are listed in table 5.8 and the average Q value are plot in Fig.5.26 overlapped with COMSOL simulation for comparison. The experimental Q_u vs. gap width trend shows a good match with COMSOL simulation results. The Q_u averaged for $Wg=10.5\ \mu\text{m}$ is a little bit lower than the predicted value in the trend indicating that COMSOL simulation for this design point might be off. Table 5.8 shows the summary of measured quality factor (Q) for the resonators of all the same design but different gap width under test. In terms of Q_u , the maximum value (Q_u^{MAX}) is found to be 4 times larger than the minimum value (Q_u^{MIN}) across the sample and occurs at the same gap width predicted by COMSOL FEM.

This trend essentially indicates that for the LN LVR (Wg non-optimized) operating at 500MHz, the level of energy loss due to the anchors is relatively large, and gap width plays an important role in determining the Q_{anc} .

Table.5. 8. Summary of unloaded quality factor (Q_u) from experimental data for different gap width

Wg (μm)	Max.	Min.	Ave.
3	1135	777	956
6	1865	497	1176
9	2383	1398	1813

10.5	968	968	968
12	2270	1243	1703
13.5	1985	1238	1508
15	1112	1112	1112

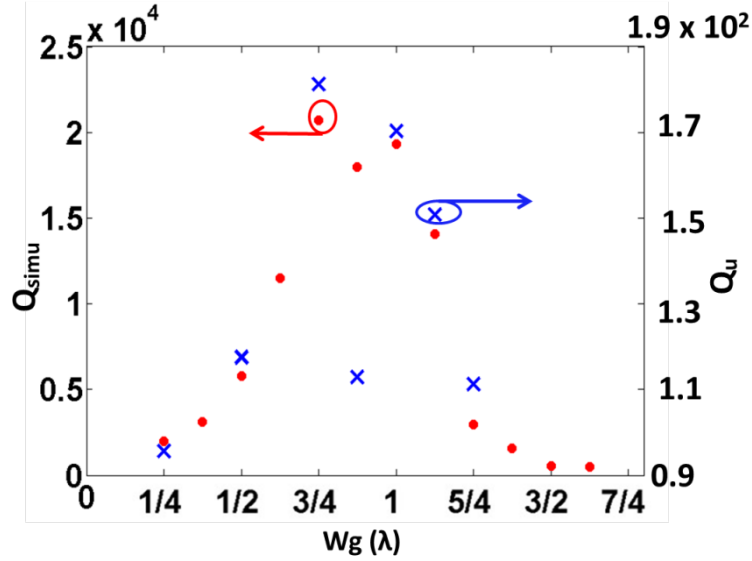
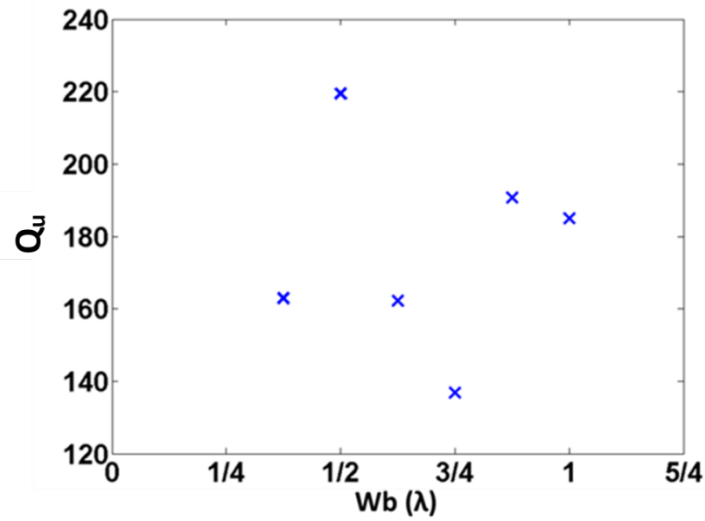


Fig.5.26. Average experimental measurements validated COMSOL simulation on Q due to anchor losses vs. gap width.

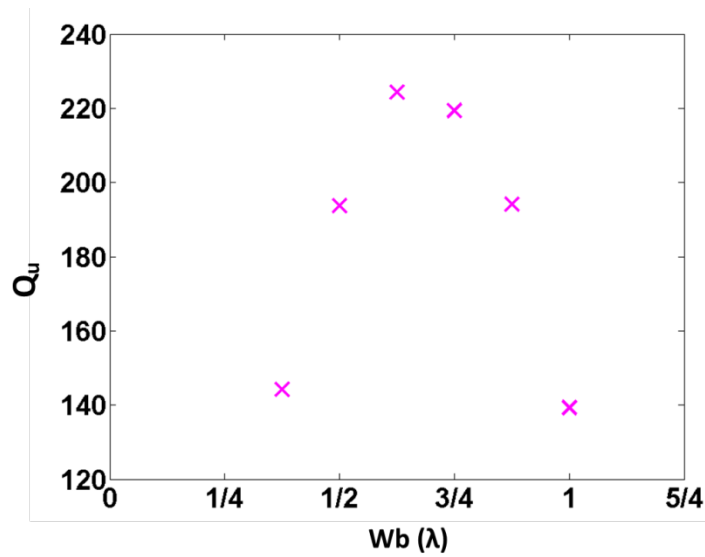
5.3.1.2 Metalized bus optimization

The impact of metalized bus in determining the anchor losses is studied by collecting experimental data over a total of 72 LN LVRs from Nano-LN and NGK samples, respectively. For the fixed frequency and LN plate geometry ($60 \times 120 \mu\text{m}^2$), 6 different metal covered bus widths (W_b) ($4.5 \mu\text{m}$, $6 \mu\text{m}$, $7.5 \mu\text{m}$, $9 \mu\text{m}$, $10.5 \mu\text{m}$ and $12 \mu\text{m}$) were implemented respectively to validate the simulation trend in Fig.5.11. A VNA was used to record their electrical response (admittance) and their loaded Q_m were extracted as the ratio f_r/f_{-3dB} . To remove the impact of electrical loading we compared the unloaded Q s of the resonators (Q_u) that were computed by using equation (5.4).

As for the Nano-LN sample, the collected values of Q are shown in Fig.5.27. The results demonstrate that very little variations exist as a function of the bus size, hence no conclusions can be drawn on what impacts Q in these devices.



(a)



(b)

Fig.5.27. Average experimental measurements of Q_u vs. metlazed bus width with (a) $Wg = 9 \mu m$ and (b) $Wg = 12 \mu m$.

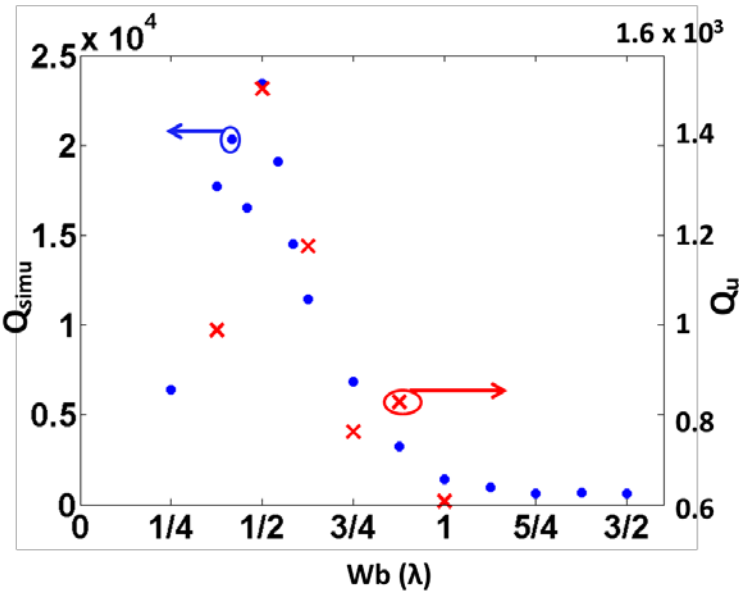
As for the NGK sample, the collected data are listed in table 5.9 and the average Q values are plot in Fig.5.28 (a1) and (b1) overlapped with COMSOL simulation for comparison (gap widths were fixed at values giving maximum Q in simulations). The experimental Q_u vs. gap width trend matches with COMSOL simulation results in both cases. The recorded maximum Q_u for $W_g=12\text{ }\mu\text{m}$ occurs when $W_b=7\text{ }\mu\text{m}$ rather than $6.5\text{ }\mu\text{m}$ as simulated. It is suspected that this is due the non-idealities introduced by misalignment and etching. In terms of Q_u , the maximum value (Q_u^{MAX}) is found to be 4 times larger than the minimum value (Q_u^{MIN}) for the case of $W_g=9\text{ }\mu\text{m}$. As for the case of $W_g=12\text{ }\mu\text{m}$, the maximum value (Q_u^{MAX}) is found to be more than twice the minimum value (Q_u^{MIN}). The average k_t^2 vs W_b are plot in Fig.5.28 (a2) and (b2) for both gap widths respectively. The average k_t^2 fluctuate within $\pm 5\%$ for different metalized bus widths in both cases, indicating that and the device k_t^2 can be maintained to a high value independently of Q .

Table.5. 9. Summary of unloaded quality factor (Q_u) from experimental data for the resonators of all the same design but different metalized bus with(a) $W_g=9\text{ }\mu\text{m}$

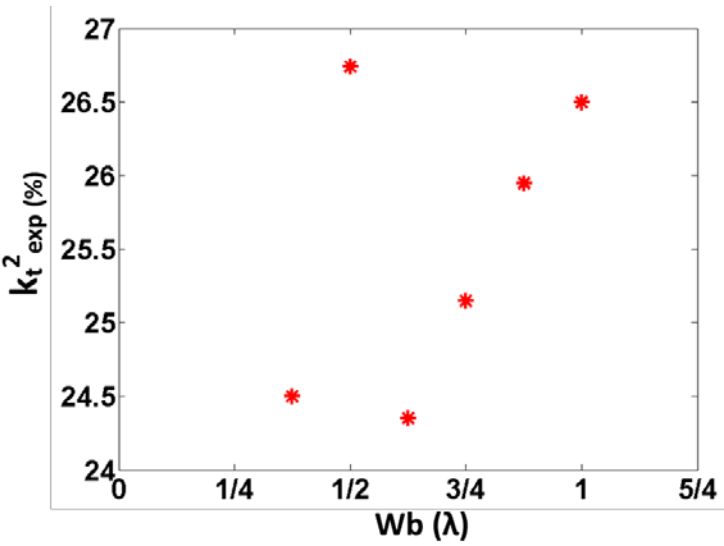
Wb (μm)	Max.	Min.	Ave.
4.5	1300	464	958
6	2191	867	1526
7.5	1427	865	1176
9	910	730	763
10.5	1101	699	829
12	728	487	608

(b) $W_g=12\text{ }\mu\text{m}$

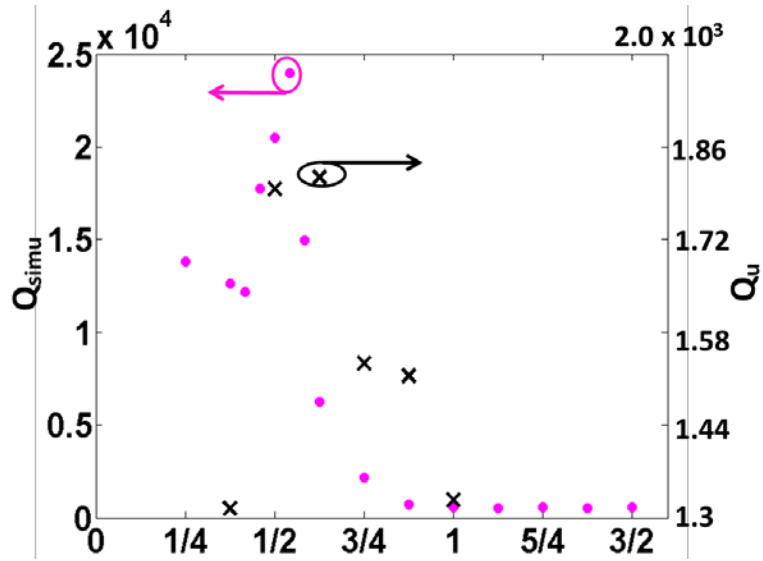
Wb (μm)	Max.	Min.	Ave.
4.5	1469	1165	1317
6	2441	1202	1892
7.5	2176	1750	1912
9	1676	1479	1578
10.5	1585	1525	1555
12	1338	1325	1331



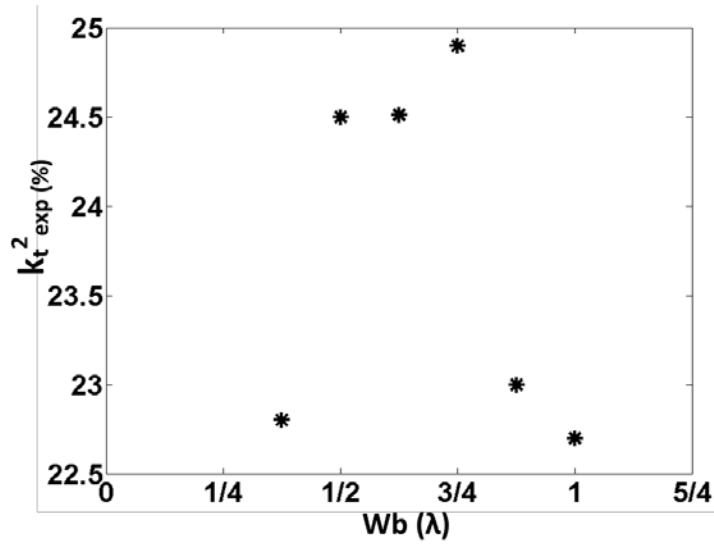
(a1)



(a2)



(b1)



(b2)

Fig.5.28. Average experimental measurements validated COMSOL simulation on Q_u due to anchor losses and k_t^2 vs. metalized bus width with (a) $Wg=9\ \mu\text{m}$ and (b) $Wg=12\ \mu\text{m}$.

These trends indicate that for the LN LVR operating at 500MHz, the level of energy loss due to the anchors can be further optimized when the gap width is properly designed. The width of the metalized bus plays a secondary role in determining the Q_{anc} .

5.3.1.3 Anchor geometric optimization

A 2-D design space as illustrated in Fig.5.14 is constructed to demonstrate the impact of anchor's width (W_a) and length (L_a) on the device Q .

Experimental data were collected for a total of 72 devices from NGK sample. 3 identical devices (located next to each other and belonging to the same chip) were used to collect statistics for each anchor's geometry. A VNA was used to record their electrical response (admittance) and their loaded Q s were extracted as the ratio f_r/f_{-3dB} . To remove the impact of electrical loading we compared the unloaded Q s of the resonators (Q_u) that were computed by using equation (5.4).

The collected data are listed in table 5.10 and the average Q_u values are plot in Fig.5.29 (a1) and (b1) for both gap widths rendering maximum Q . COMSOL simulation with the corresponding area circled in red are shown in Fig.5.29 (a2) and (b2) (as explained in detail in 5.2.2.2) for comparison. As shown in Fig.5.29, variations in anchor's width (W_a) and length (L_a) introduced relatively small changes in the measured quality factor (Q_u). These trends indicate that for the LN LVR operating at 500MHz, the level of energy loss due to the anchors is less affected by the geometry of the anchor. The gap width and width of the metalized bus plays a more important role in determining the Q_{anc} .

Besides, the occurrence of maximum and minimum from experiments for $W_g=9\text{ }\mu\text{m}$ matches simulation results in Fig.5.14(a) better than the case for $W_g=12\text{ }\mu\text{m}$ which is likely due to the better stability of Q demonstrated by LVR with $9\text{ }\mu\text{m}$ gap once subjected to non-ideal situation as described in 5.2.3.

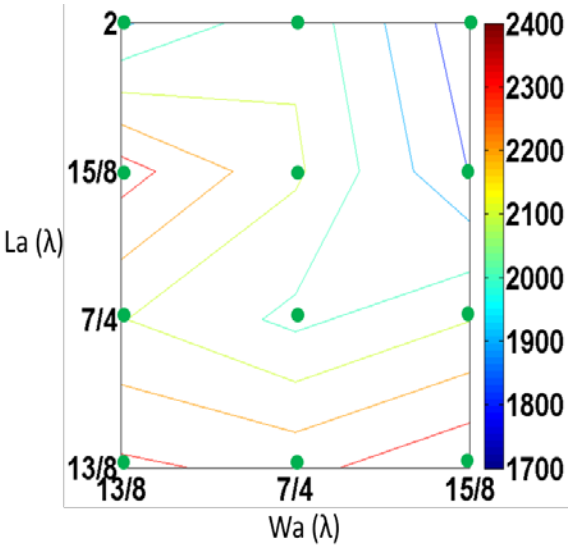
Table.5. 10. Summary of unloaded quality factor (Q_u) from experimental data for the resonators of all the same design but different anchor's width (W_a), length (L_a) with(a) $W_g=9\text{ }\mu\text{m}$

$W_a\text{ (}\mu\text{m)}$	$L_a\text{ (}\mu\text{m)}$	Max.	Min.	Ave.
19.5	19.5	2392	2247	2320
21	19.5	2270	2270	2270
22.5	19.5	2415	2361	2388
19.5	21	2238	1979	2105

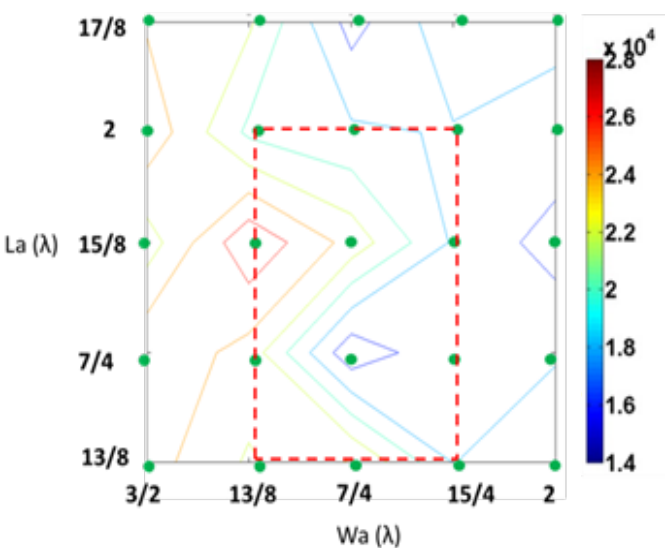
21	21	2441	1236	1976
22.5	21	2377	1719	2095
19.5	22.5	2438	2279	2345
21	22.5	2372	1849	2119
22.5	22.5	2383	1212	1797
19.5	24	2069	1927	1883
21	24	2407	1501	2076
22.5	24	2065	1195	1732

(b) $W_g=12\text{ }\mu\text{m}$

Wa (μm)	La (μm)	Max.	Min.	Ave.
19.5	19.5	1460	1460	1460
21	19.5	1896	1436	1666
22.5	19.5	2225	1143	1684
19.5	21	1424	956	1190
21	21	2292	2292	2292
22.5	21	1572	950	1261
19.5	22.5	1753	1411	1582
21	22.5	1260	820	1079
22.5	22.5	1357	1317	1337
19.5	24	1870	1870	1870
21	24	2241	2238	2240
22.5	24	1768	1110	1362



(a1)



(a2)

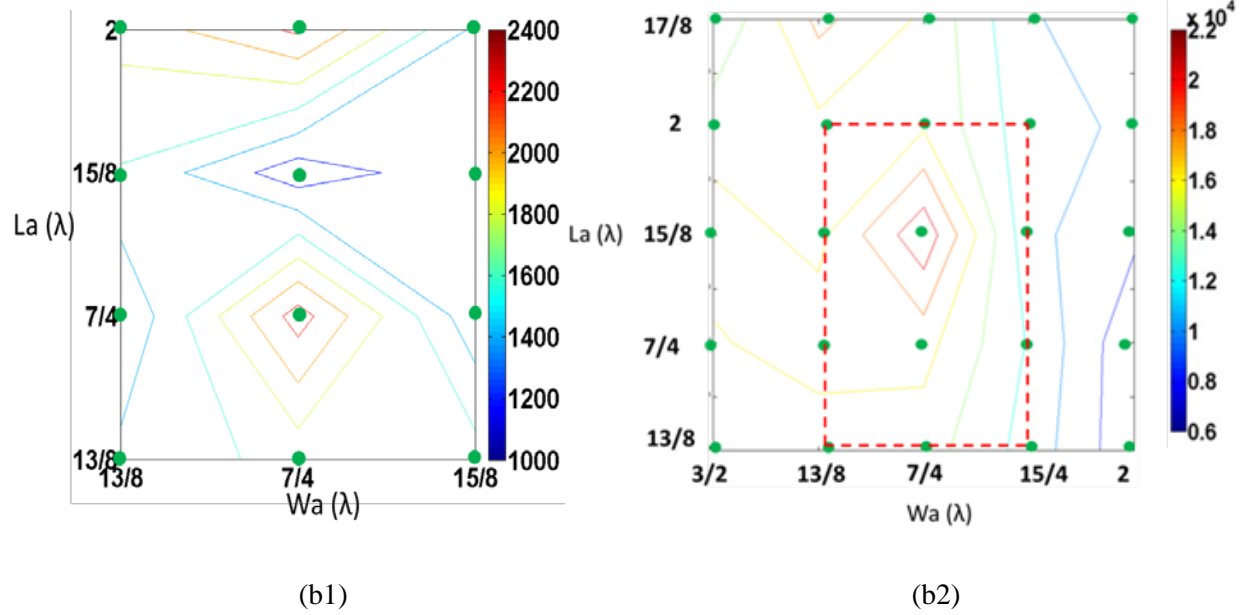


Fig.5.29. Contour plot of Q due to anchor losses vs. anchor geometry (W_a and L_a) with gap width set to (a) $9 \mu\text{m}$ and (b) $12 \mu\text{m}$. (a1) and (b1) are plot according to Q_u from experimental data and (a2) and (b2) are plot according to COMSOL FEA results. Green dots indicate actual values measured. Contours are automatically generated by matlab and are used to guide the eye.

6. Spurious mode suppression and robustness to processing

LN LVRs have exhibited extraordinary high k_t^2 ($> 15\%$) and Q s around 1,000[5][27][56]. Because of the high k_t^2 , it is extremely complicated to control the various modes of vibration and ensure that a single mode is excited. Process variations also render any of the techniques previously implemented for confining energy in a single mode [27][28] ineffective. This section reports on the design and demonstration of active reflectors for suppressing a certain class of spurious modes and simultaneously maintaining high electromechanical coupling (k_t^2) in LVRs based on X-cut ion-sliced LN thin film on SiO_2 (Fig.1.6).

6.1 Active reflectors for high performance LN LVRs

In chapter 4, we introduce the active reflector design as a method to achieve high k_t^2 . In this chapter, we further analyze the active reflector design as a method to suppress spurious modes even in the presence of misalignment and over/under-etching errors while simultaneously maintaining a high k_t^2 . Similarly, the new design is demonstrated in a LN on SiO_2 technology platform (on a silicon substrate) that simultaneously address the issue of large temperature coefficient of frequency exhibited by stand-alone LN devices (see Chapter 7 for TCF compensation). The LN and SiO_2 thicknesses were set to 500 nm and 800 nm respectively, as employed in Chapter 4, to compensate large temperature coefficient of frequency exhibited by stand-alone LN devices to be around -20 ppm/ $^\circ\text{C}$. The methodology is explained in detail in Chapter 7.

By adding electroded quarter wavelength ($\lambda/4$) regions at the two ends of the resonant plate, active reflectors (since an electrical signal is applied to them) are formed to improve the device performance. In Chapter 4 the impact of active reflector coverage on k_t^2 was reported (see Fig. 4.2). Although a 33% covered active reflector yields the highest k_t^2 , once misalignment ($0.5 \mu\text{m}$ ($\lambda/24$) in the simulation) due to processing is factored in, devices with 100% covered active reflector demonstrate the most stable k_t^2 and complete suppression of spurious vibrations.

The sensitivity of device performance (k_t^2 and spurious vibrations) to metal coverage ratio and polarity (signal or ground) of $\lambda/4$ active reflectors when misalignment and over/under etching are present was analyzed via FEA (frequency response analysis). All simulations were conducted with LN LVRs (60 μm wide x 80 μm long resonate plate) composed of 10 fingers with 30% main finger coverage resonating at 500 MHz. Q was assumed to be 1000 in all the simulations. Active reflector metal coverage was swept from 1/12 to 1 in increments of 1/12. The analysis shows that for LVR with 100% covered active reflectors demonstrate the most stable k_t^2 and complete suppression of spurs once subjected to misalignment. Different levels of misalignment were simulated to reveal the robustness of LVRs that use 100% covered active reflectors (see Fig.6.1 a). The analysis shows that for LVR with 100% covered active reflectors, the k_t^2 is unaffected by misalignment under 0.5 μm ($\lambda/24$). Two spurs at two sides of the resonance peak increased in magnitude as the misalignment exceeded 0.3 μm ($\lambda/40$) while in-band response is completely free from spurs. Simulated frequency response of LN LVRs with 50% covered active reflectors and 100% covered active reflectors subjected to the same amplitude of misalignment 0.5 μm ($\lambda/24$) are compared in Fig.6.1 (b) and (c). Successively, different levels of over-etching were simulated to reveal the robustness of LVR that use 100% covered active reflectors (see Fig.6.2 (a)). The analysis shows that for LVR with 100% covered active reflectors, the k_t^2 is practically unaffected by over-etching as long as it is kept below 0.6 μm ($\lambda/20$). Over-etching below 0.1 μm ($\lambda/120$) barely introduces spurious modes. When over-etching becomes larger than 0.5 μm ($\lambda/24$), spurs close to the main resonance peak occur. Additionally, spurs grow seriously once combined with misalignment (Fig. 6.2 (b)). The FEA shows that 100% coverage and polarity opposite to adjacent $\lambda/2$ electrode optimize the overall device performance. The simulation results were validated experimentally by building a matrix of devices with different parameters (Table 4.1).

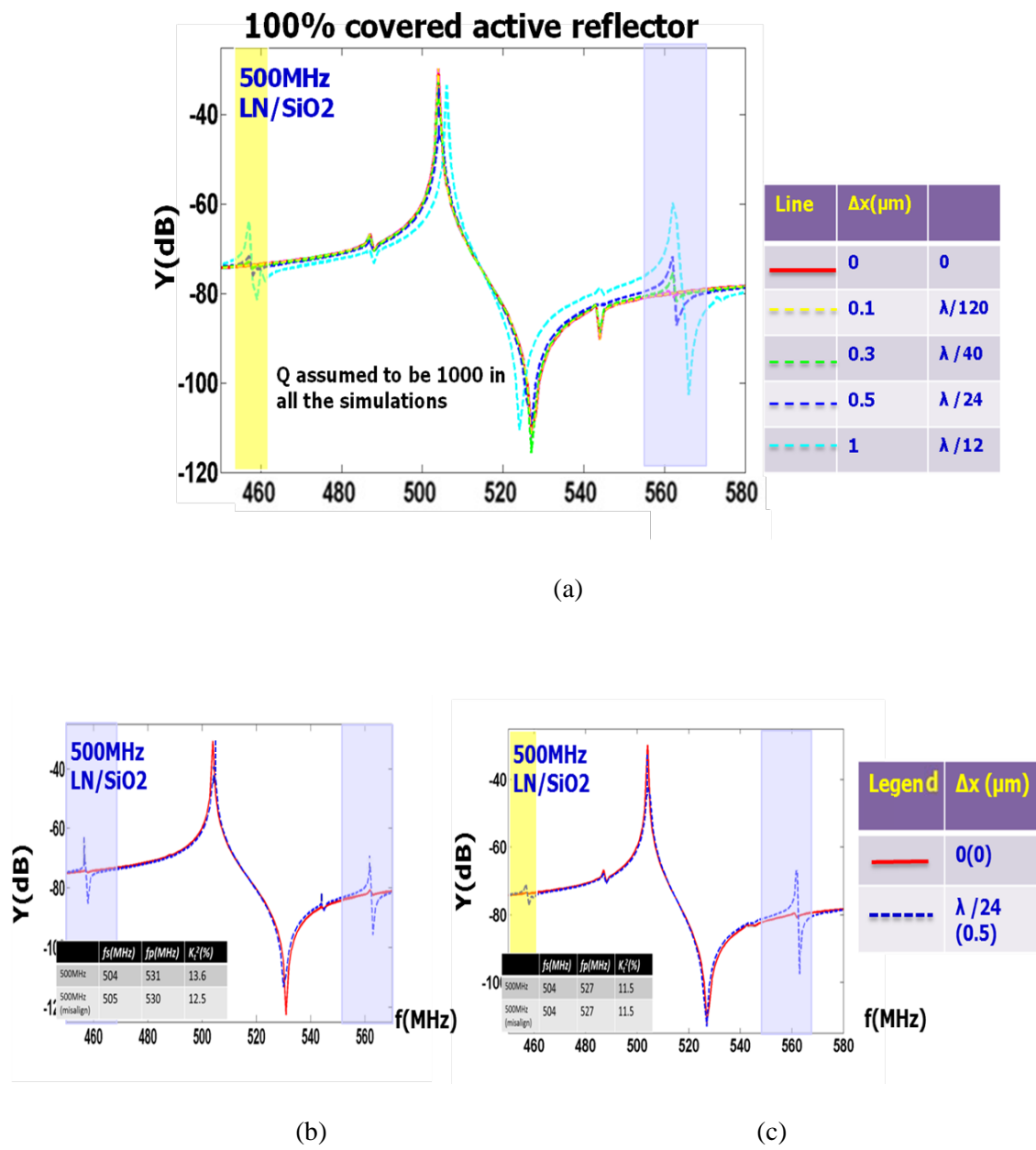


Fig.6.1. (a) Simulated frequency response of 100% covered active reflectors design subjected to the different level of misalignment and a comparison of the simulated frequency response of (b) 50% covered active reflectors design vs. (c) 100% covered active reflectors design once subjected to the same level of misalignment $0.5 \mu\text{m}$ ($\lambda/24$)

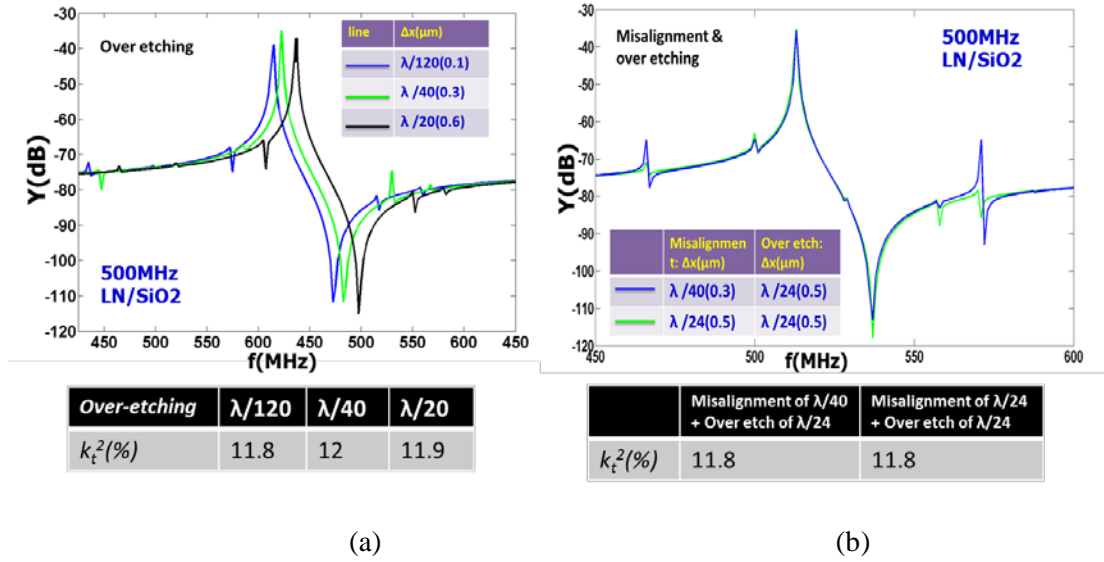


Fig.6.2. (a) Simulated frequency response of 100% covered active reflectors design subjected to the different level of overetching (b) Simulated frequency response of 100% covered active reflectors design subjected to the a combination of misalignment and overetching

Optimized active reflectors that resort to 100% metal coverage of the $\lambda/4$ extensions (Fig. 4.1c) enable: (i) a considerable improvement of k_t^2 , (ii) spurious mode suppression, robustness to processing (iii) misalignment and (iv) over/under-etching. 2X improvement in k_t^2 and complete suppression of in-band spurious vibrations were attained with respect to the conventional design (Fig. 4.1a) despite 0.5 μm misalignment and more than 0.5 μm overetch in the fabrication process.

6.2 Experimental Results

6.2.1 Fully covered active reflector design

A SEM image of one of the fabricated devices (LN LVRS of 100% covered active reflectors design) is shown in Fig. 6.4. The designed S0 mode is present in the admittance response of devices placed at all orientations, and is dominant (highest Q) when the devices are placed at all orientations except from -50° , -60° and -70° to $+z$ axis. The average value of the measured k_t^2 (Fig.6.5) displayed the same trend of the simulated results, but showed values that deviated up to 50% of the predicted one for certain orientations. The reason of this discrepancy might be that k_t^2 is affected by processing as x-y

misalignment errors have a different impact on devices with different orientations. Experimental data also confirm that a maximum coupling for the S0 mode that exceeds 10 % is obtained for an in-plane rotation of 60° with respect to the +z axis. (See Fig. 6.5)

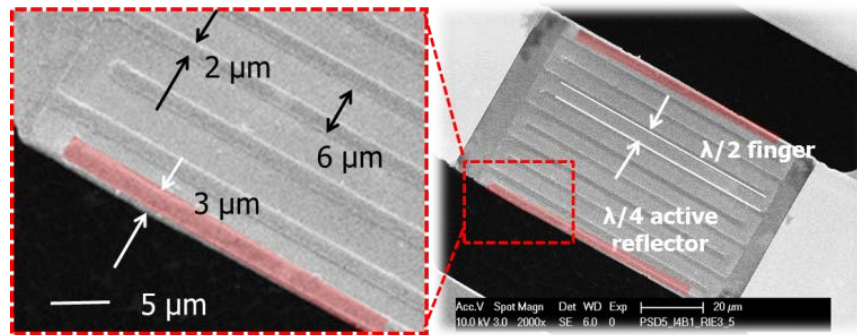


Fig.6.3. SEM of active reflector design(10 80 μm long electrode and 6 μm pitch with 2 μm metal strips) for device type A1. Active reflectors are highlighted in red.

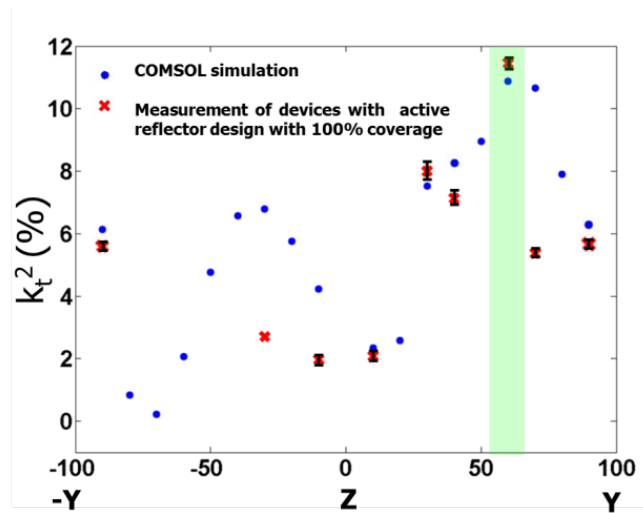


Fig.6.4. The comparison of the averaged measured and simulated k_t^2 for LN on SiO_2 LVRs for various orientations.

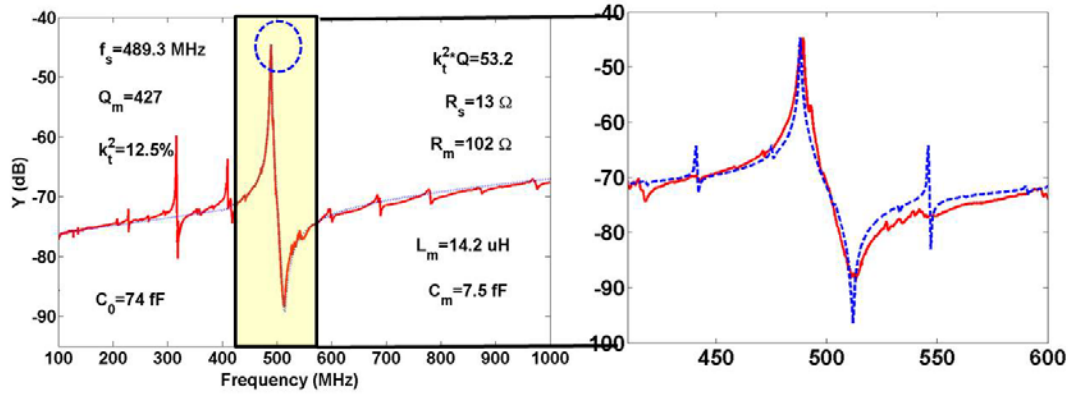


Fig.6.5. The measured and fitted admittance response for LN on SiO₂ LVR placed at 60° to the +z axis (type A1). The comparison of the measured (in red) and 2D COMSOL simulated responses (in dashed blue) (misalignment of 0.5 μm and over etching of 0.5 μm) for the same devices are shown in the zoomed-in plots on the right.

The same designed devices with different metal coverage ratio (0%, 50% and 100%) of $\lambda/4$ active reflectors were fabricated to verify the simulated results to obtain minimum sensitivity to misalignment and over/under etching and maximum k_t^2 in such non-ideal situations. High k_t^2 up to 12.5% was achieved with an LN LVRs placed at 60° to the +z axis (type A1 introduced in table 4.1) with the presence of a considerable misalignment (0.5 μm on average in both x and y directions) and over-etching (0.5 μm on average in both directions) confirming the simulation data (see Fig.6.6). As shown in Fig.6.7, the overlapped frequency response for LN LVRs of conventional design, 50% covered reflector design and 100% covered reflector design subjected to a considerable misalignment (0.5 μm on average in both x and y directions) and over-etching (0.5 μm on average in both directions) are compared indicating that 100% covered reflector design is more robust and significantly subdues spurious modes. The dependence of k_t^2 on active reflector coverage was also studied experimentally. The results of this analysis are reported in Table 6.2. It is important to note that other spurious modes of different nature than the one that are subdued by the active reflectors are still present. These are likely to be transversal mode. These modes are not that evident in Fig. 6.6, primarily because of the overall low Q of the device.

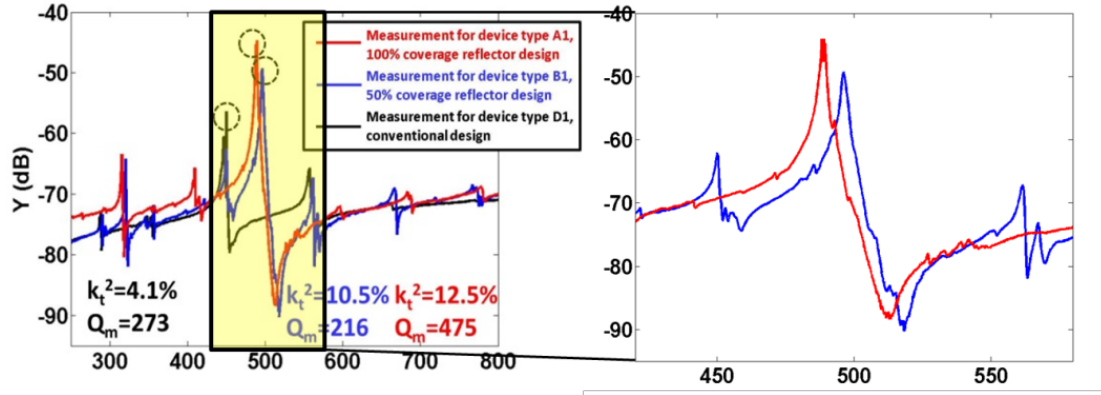


Fig.6.6. The measured responses of LN on SiO₂ LVRs vibrating around 500 MHz (120 μm aperture at -60° to the $+z$ axis) of device types A1, B1 and D1. All devices exhibited the same amount of misalignment (0.5 μm in x and y) and over etching (0.5 μm in both directions). The comparison of the measured responses of device types A1, B1 are shown in the zoomed-in plots on the right.

Table.6. 1. The comparison of the measured and simulated k_t^2 for LN on SiO₂ LVRs (10 80 μm long fingers, with a pitch of 6 μm formed by 4 μm electrode and 1 μm spacing at -60° to the $+z$ axis

Device type (# of measured devices)	Active reflector Metal coverage	COMSOL ideal	COMSOL with 0.5 μm misalignment and 0.5 μm over-etching	Experimentally Extracted k_t^2
A1(5)	100%	11.5%	10.6%	11.3%
B1(6)	50%	13.6%	11%	9.4%
C1(5)	0%	10.7%	10.3%	10.3%

The optimized active reflector design was also applied to the LN on Si technology platform purchased from NGK to demonstrate stand-alone LN devices (see Chapter 5 for more information on device Q) and showcase the ability to attain high k_t^2 in X-cut LN. The measured and fitted admittance response for a standalone LN LVR is shown in Fig. 6.7. A k_t^2 up to 26%, Q_m up to 1570 was obtained with 100% covered active reflector design even in the presence of 0.65 μm misalignment and 0.65 μm under-etch. Observed from the frequency spectrum, some spurious around resonance peak are introduced by the misalignment and under-etching as predicted by COMSOL in Fig.5.23. With better fabrication accuracy, the spurious mode will be greatly mitigated and both k_t^2 and Q are expected to be further enhanced.

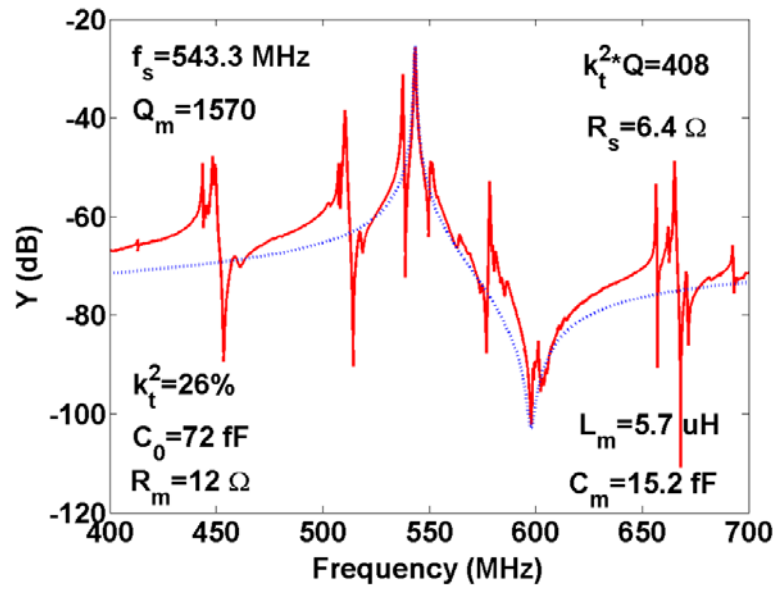


Fig.6.7. The measured and fitted admittance response of a standalone LN LVR vibrating at 500 MHz (10 120 μm long electrodes and, 6 μm pitch with 2 μm metal strip, placed at -60° to the z axis in X -cut plane) of active reflector design with 100% coverage.

7. Engineering the Temperature Coefficient of Frequency (TCF) of high electromechanical coupling LN LVRs

In this chapter, LVRs based on Y-cut ion-sliced LN thin films on SiO₂ are presented to showcase an example of how to compensate the large negative TCF of LN films (see Fig.2.4). Y-cut LN is selected due to the relatively high k_t^2 predicted by COMSOL when a SiO₂ layer used for temperature compensation is inserted in the device stack. The same methodology is applied to design X-cut ion-sliced LN thin films on SiO₂ LVRs in parallel and also validated experimentally. These devices are a promising demonstration of a technology platform that could be exported to other cuts with potentially higher Q s and k_t^2 .

7.1 Definition and analytical model

The shift in the resonance frequency of a LN resonator when subjected to temperature variations is mainly caused by material softening. The resonator TCF is primarily related to the change of the stiffness coefficients with respect to temperature. Thermal expansion, which affects the resonator dimensions and material density, plays a secondary role. In general, the TCF of a resonator whose frequency is expressed in ppm/°C and is defined as:

$$TCF = \frac{1}{f} \frac{\partial f}{\partial T} \quad (7.1)$$

$$TCF = -\frac{1}{w} \frac{\partial w}{\partial T} + \frac{1}{2} \frac{1}{E} \frac{\partial E}{\partial T} - \frac{1}{2} \frac{1}{\rho} \frac{\partial \rho}{\partial T} \quad (7.2)$$

The above equations can be applied to the specific characteristics of the LN LVRs and results in:

$$TCF = \frac{1}{2} [TC_{ij} + (\alpha_v + \alpha_{\perp v} + \alpha_k)] - \alpha_v \quad (7.3)$$

where TC_{ij} refers to the relative temperature dependence of the stiffness constant C_{ij} ; α_v and $\alpha_{\perp v}$ is the thermal expansion coefficient along the wave propagation direction, and perpendicular (in the plane) to

the wave propagation direction, α_k is the thermal expansion coefficients along the y- direction (orthogonal to the plane wave).

Given that LN becomes mechanically soft with an increasing temperature due to negative TC_{ij} , the resonators based on uncompensated Y-cut LN display a rather large and negative TCF of about – 80 ppm/°C. Given thin film SiO_2 is isotropic and has a positive temperature coefficient of Young's modulus, it can be used in the device stack to enable temperature compensation of the LN LVR piezoelectric resonator. For this reason SiO_2 has been widely employed in different types of piezoelectric resonators to demonstrate temperature stable devices [57][58][59][60][61][62].

Analytical calculation for the TCF characteristic in the LN/ SiO_2 composite plate has been conducted for different orientations in the Y-cut plane based on Eq. (7.3) as shown in Fig.7.10 (reported with experimental data). The TC_{ij} and α value employed in the calculations are effective values calculated for the LN/ SiO_2 composite plate given by the following expressions [63][64]:

$$TC_{ij_{eff}} = \frac{\sum_{m=1}^n E_m t_m TC_{ij_m}}{\sum_{m=1}^n E_m t_m} \quad (7.4)$$

$$\alpha_{eff} = \frac{\sum_{m=1}^n E_m t_m \alpha_m}{\sum_{m=1}^n E_m t_m} \quad (7.5)$$

where E_m is the Young's modulus of m_{th} layer, t_m is the thickness of m_{th} layer, TC_{ijm} is the relative temperature dependence of the stiffness constant C_{ij} of m_{th} layer and α_m is the thermal expansion coefficient of m_{th} layer, respectively.

7.2 2D FEM modeling

Given the sample availability from a third party vendor, the thickness of LN thin film was set to 420 nm. We have modelled and analyzed the impact of inserting SiO₂ layers of various thicknesses on devices' TCF with the LN thin film fixed to the given thickness.

The TCF characteristic of the S0 mode in both LN alone and LN/SiO₂ composite plate was modeled by COMSOL multiphysics finite element analysis (FEA). Both piezoelectric and thermal expansion COMSOL moduli are used to describe the behavior of the device. The rotated stiffness and piezoelectric coupling matrix for each orientation in the Y-cut plane are derived from the Z-cut LN matrix [65] using the transformation matrix and bond matrix [66]. The obtained matrices are then input into the device model and used to predict the resonator frequency dependence on temperature. Assuming a linear TCF (a valid assumption since the frequency-temperature dependency measured from actual devices displayed a linear regression coefficient > 0.95 , see Fig.7.8) an eigenfrequency analysis was conducted at two different temperatures (0°C and 100°C in our analysis) so as to derive the temperature induced frequency shift. The material properties used in the simulations are listed in Table 2.1 in Chapter 2. The Al electrodes were not included in the FEM analysis to avoid using a very fine mesh and hence significantly increasing the simulation time. Given the thickness of the oxide and LN layers, the impact of Al is considered to be negligible for the particular stack of this work.

COMSOL FEA was used to explore the dependence of the first order TCF on orientation. The analysis verified that the TCF has a slight dependence on orientation (few ppm/°C). This is to be expected as there is a difference in the values of α and TC_{ij} as we move from x to z direction in the Y-cut LN/SiO₂ composite plate. A comparison of TCF for different orientations from analytical calculation, COMSOL TCF FEA, and experiments will be shown in section 7.4.2 (see Fig.7.9). The simulated TCF values for S0 mode are also listed in Table XIV already compared with experimental data.

It is interesting to note that previous analysis in AlN/SiO₂ compensated lamb wave resonators indicated that the first-order TCF of the S0 mode in composite membranes has a dispersive characteristic

[69][67].The COMSOL TCF FEA performed here also exhibited a similar dispersive behavior for the first-order TCF for a LN thicknesses fixed at 420nm (see Fig.7.1 for confirmation). Nonetheless, the FEA also revealed that, a low first-order TCF ($< \pm 5$ ppm/°C) can be achieved for a broad range of frequencies from 500 to 1000 MHz by setting the SiO₂ thickness to 1 μ m for a given 420 nm thick Y-cut LN thin film. This value is definitely compatible with the manufacturing process of the sample and could be explored in future implementations. The TCF analysis was then validated by using an oxide layer set to be 1600 nm thick given what was available from the vendor of thin film of LN.

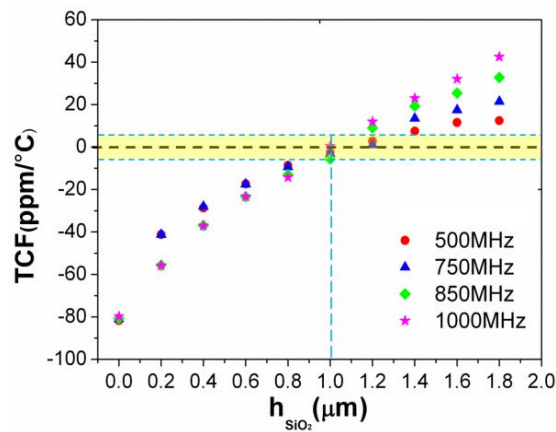


Fig.7.1. Dependence of the first-order TCF on SiO₂ thickness for different frequencies of the main S₀ mode (Y-cut LN LVR with 20° orientation to x-axis and LN film thickness of 420nm). Highlighted area indicates a first-order TCF of ± 5 ppm/°C can be achieved from 500 to 1000 MHz by setting the SiO₂ thickness to 1 μ m for a Y-cut LN thin film thickness of 420 nm.

As discussed in the introduction, research activities on high frequency MEMS resonators have focused on the development of devices for programmable RF front-ends with a particular attention to reconfigurable filters that can cover the current commercial operating bands and potentially offer adaptation to future standards. The need to meet the requirements dictated by wireless standards and simultaneously achieve reconfiguration has pushed researchers to look at devices and materials with higher electromechanical coupling, k_t^2 , which is also the key parameter to maximize in the development of LN LVR with temperature compensation. COMSOL simulations explained in 2.1.2 were conducted for the given composite stack to explore the in plane orientation to achieve maximum k_t^2 for h/λ of 0.16 and 0.25 targeting center frequencies of 460 and 720 MHz (Fig.7.2) respectively. Simulated data suggested that maximum coupling for the S₀ mode in a 420 nm Y-cut ion-sliced LN thin film on 1600 nm SiO₂ is

obtained for an in plane clock wise (CW or positive) and counter clock wise (CCW or negative) rotation of 70° with respect to the x axis, where the angle, θ° , is defined as the angle between the electrode pitch direction and the +x axis.

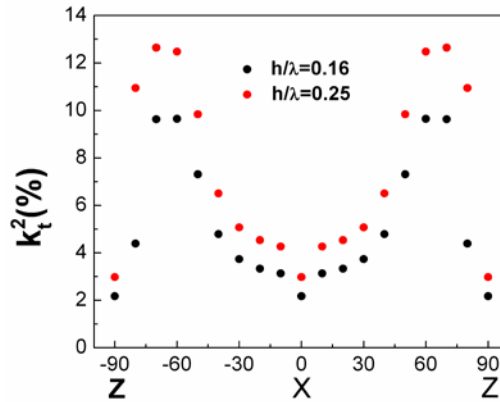


Fig.7.2. Simulated k_t^2 for LN(Y-cut) on SiO_2 LVRs for various orientations and two characteristic h/λ .

Similarly, the same technology platform developed based on Y-cut ion-sliced LN thin films on SiO_2 for the first time was exported to X-cut LN thin film which has a potentially higher k_t^2 as shown in Fig.2.5. The TCF characteristic of the S0 mode in LN(X-cut) / SiO_2 composite plate was modeled by COMSOL multiphysics finite element analysis (FEA). The LN and SiO_2 thicknesses were set to 500 nm and 800 nm respectively to compensate large temperature coefficient of frequency exhibited by stand-alone LN devices as well as maintain a high k_t^2 greater than 10%. Simulation results suggested that (see Fig.7.3) by setting LN(X-cut) and SiO_2 thicknesses to be 500 nm and 800 nm, respectively the large temperature coefficient of frequency exhibited by stand-alone LN devices would be readily compensated to be around $-20 \text{ ppm}/^\circ\text{C}$ (Analysis verified that the TCF has a slight dependence on orientation (few $\text{ppm}/^\circ\text{C}$)).

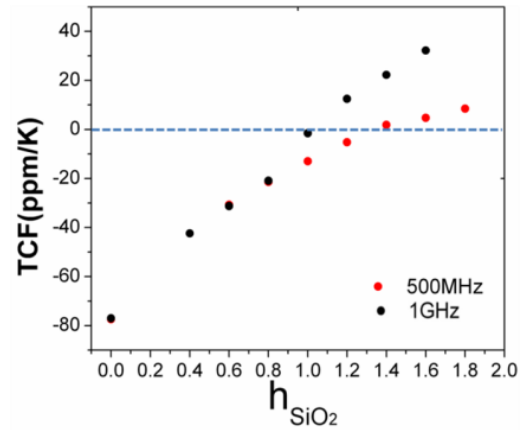


Fig.7.3. Dependence of the first-order TCF on SiO_2 thickness for different frequencies of the main S_0 mode (X-cut LN LVR with 0° orientation to z-axis and LN film thickness of 500nm). Dashed line indicates a first-order TCF of around 0 ppm/ $^\circ C$ can be achieved from 500 to 1000 MHz by setting the SiO_2 thickness to 1.0-1.3 μm for a X-cut LN thin film thickness of 500 nm.

7.3 Design of TCF compensated LN LVRs

As for the Y-cut ion-sliced LN thin film on SiO_2 LVRs, the pitch of the devices' electrode was set to 4 and 3.6 μm respectively to ensure operation around 720 and 800 MHz for the fundamental S_0 mode. The total number of fingers was varied between 10 and 20 and finger lengths of 40 and 80 μm were considered for both pitch width designs (Table 7.1). These variations were made to explore the impact of device size on its performance.

Table.7. 1. Dimensions of the LN/ SiO_2 LVRs

Quantity	Type A	Type B
Top electrode finger number	10 , 20	10, 20
Pitch width[μm]	4	3.6
Electrode aperture [μm]	40, 80	40, 80
Metal line width [μm]	2	1.6
Top Al electrode thickness[nm]	100	100

Devices of orientation varying from -90° to $+90^\circ$ in increments of 10° were fabricated on the same die to verify the dependence of k_t^2 (Fig. 7.2) and TCF on orientation.

Please note that for the designs for Y-cut LN thin film on SiO_2 LVRs described in this chapter, no particular attention was placed in minimizing spurious vibrations and hence properly designing the edge reflectors described in Chapter 6. Therefore, these resonators exhibit undertones and overtones of the main S0 mode.

As for the X-cut ion-sliced LN thin film on SiO_2 LVRs, the pitch of the devices' electrode was set to $6\text{ }\mu\text{m}$ to ensure operation around 500 MHz for the fundamental S0 mode. The total number of fingers was set to 10 and finger lengths of 80 and $120\text{ }\mu\text{m}$ were considered for both pitch width designs. Devices of orientation varying from -90° to $+90^\circ$ in increments of 10° were fabricated on the same die to verify the dependence of k_t^2 (Fig. 4.2) and TCF on orientation.

Please note that for the designs for X-cut LN thin film on SiO_2 LVRs described in this chapter, attention was placed in minimizing spurious vibrations and hence properly designing the edge reflectors described in Chapter 5.

For both designs based on Y-cut and X-cut LN thin film on SiO_2 LVRs no particular attention was placed in maximizing Q and hence not properly designing the geometrical dimensions of the resonator described as described in Chapter 5. Most of the resonators tested for this study exhibit a Q below 1100.

7.4 Experimental results

As for the Y-cut ion-sliced LN thin film on SiO_2 LVRs, devices were fabricated on the same die following the process flow shown in Fig. 7.4 which is a simplified version of the process flow displayed in Chapter 3 (Fig.3.4) for the first generation LN LVRs. For 0° , 70° , 80° and 90° orientation to x axis, no working devices are available for measurement since they cracked after the XeF_2 release due to residual

stress in the composite plate. The integration of a SiO_2 layer with LN on silicon is challenging given the considerable lattice constant and coefficient of temperature expansion (CTE) mismatch between these materials. Because of these various issues, in most cases, the suspended films defined even in this work show significant residual stresses that impact the overall device yield. Rapid thermal annealing, following the methods discussed in Chapter 3, could be used to resolve this issue.

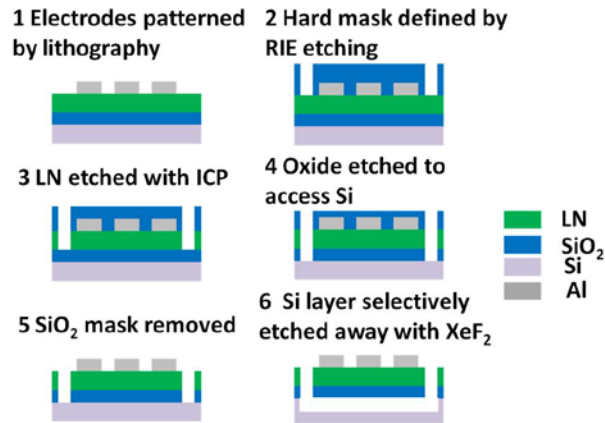


Fig.7.4. Flow chart for the fabrication process of Y-cut ion-sliced LN thin film on SiO_2 MEMS resonators

As for the X-cut ion-sliced LN thin film on SiO_2 LVRs, devices of different orientation were fabricated on the same die following the process flow displayed in Chapter 3 (Fig.3.4) for the first generation LN LVRs. High Q (~ 700) devices of 30° and -60° orientation to x axis were used for TCF measurement since they exhibited clear resonance peak shift when temperature was swept.

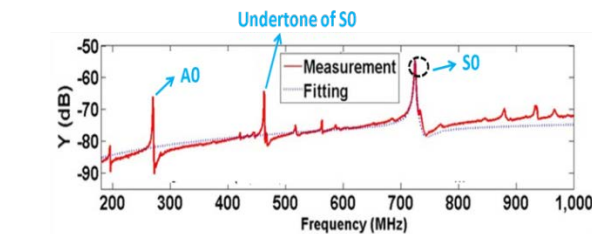
The microfabricated LN/ SiO_2 LVRs were tested in a Cascade RF probe station and the scatter parameters were measured by an Agilent (N5230A) network analyzer after performing a short-open-load calibration and a de-embedding of the parasitic capacitance coming from the pad layout (C_f). A feedback controlled heating unit was employed to modify the device temperature during the measurements.

Note that these resonators belong to 1st generation devices and need to be de-embedded due to the relatively large parasitic capacitance introduced by the SiO_2 layer on silicon substrate as discussed in Chapter 3.

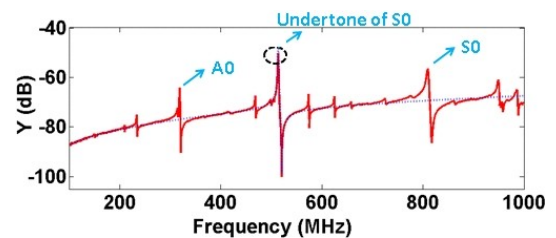
7.4.1 Characterization of electromechanical coupling (k_t^2) and quality factor (Q)

The experimental data were fitted with the MBVD equivalent circuit model to extract the six equivalent circuit parameters shown in Fig. 2.4(c). It is important to note that R_s and R_o are lumped parasitic series and parallel resistances coming from the electrodes and the LN/SiO₂ film. Their extraction by fitting comes with some error. However, since the motional resistance R_m ($\geq 500\Omega$) of the LN/SiO₂ LVRs are much higher than the parasitic series resistance R_s (10~20 Ω), the error ($< 10\Omega$) in the value of the fitted R_s will not cause considerable variations in the extraction of the resonator main parameters (for example, Q).

As for the Y-cut ion-sliced LN thin film on SiO₂ LVRs, the designed S0 mode is present in the admittance response of devices placed at all orientations, and is dominant (highest Q from 160 to 420) when the devices are placed at 40°, 60°, and 80° to x axis. As shown in Fig. 7.5(a), a maximum k_t^2 of 9.1% was measured for a resonator with center frequency of 730 MHz and placed at -60° to the x axis. The average value of the measured k_t^2 (Fig.7.6) for the main S0 mode displayed the same trend of the simulated results, but showed a value that is approximately 3/5 of the predicted one. This discrepancy between theoretical and experimental k_t^2 of the S0 mode might be caused by non-ideal material properties in the thin-film LN and alignment errors in the lithography step. Moreover, the influence of the electrode metallization (IDT structure) was not considered in the theoretical calculations for this work.



(a)



(b)

Fig.7.5. The measured and fitted admittance response of LN on SiO₂ LVR placed at -60° to the x axis. with k_t^2 up to 9% in air (10 80 μm long fingers of design Type A) (b) The measured and fitted admittance response of a LN on SiO₂ LVR placed at -20° to the x axis, with a FOM (Figure of Merit = $k_t^2 * Q$) of 43 (10 80 μm long fingers of design Type B). The fitting parameters are provided for the peaks with black dashed circles. Cf listed in the table below each device response represents the parasitic capacitance coming from the pad layout.

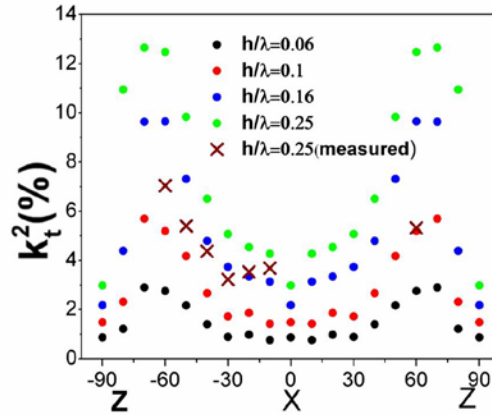


Fig.7.6. The comparison of the averaged measured and simulated k_t^2 for LN on SiO₂ LVRs for various orientations

Devices oriented from 10° to 60° to the x axis also exhibited a resonance from 420 to 460 MHz for devices with pitch of 4 μm formed by 2 μm electrode and 2 μm spacing, and 505 to 550 MHz for devices with pitch of 3.6 μm formed by 2.6 μm electrode and 1 μm spacing. The center frequency varies over 10% depending on devices' orientation. This resonance can be classified as an undertone of the main S0 mode since its wavelength, λ , is around 3/2 the value of the main S0 mode (see Fig.7.6) and has the same phase velocity of the main S0 mode. In particular, resonators oriented from 10° to 30° with respect to x axis displayed S0 undertone vibrations with high Q and k_t^2 . A Q higher than 1320 was observed on a LVR with a center frequency of 419.3 MHz placed at -30° to the x axis (Fig.7.5 (b)). A maximum k_t^2 of 6.2% was measured for a resonator with center frequency of 511.8MHz placed at 20° to the x axis (10 80 μm long fingers of design type A). A FOM (Figure of Merit = $k_t^2 * Q$) as high as 43 was obtained for a LVR having a 20° orientation to x axis. A0 mode vibrations were also seen in the spectrum of all resonators (see Fig.2.2). A1 mode with a high phase velocity has also been observed for specific orientations.

A summary of the obtained experimental results for the S0 mode and its undertone is reported in Table 7.2.

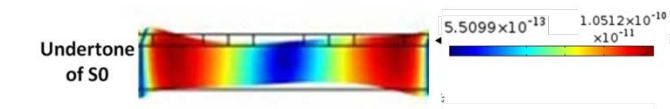


Fig.7.7. Undertone of S0 modes that was identified in the experimental response of the LN/SiO₂ LVRs

Table.7. 2. Summary of experimental results for the resonators fabricated on the same die: electromechanical coupling (k_t^2), quality factor (Q) and center frequency (fs) of each measurement are reported. All the averages (aver) listed are obtained from measurement of 2-6 devices depending on the yield for each orientation. The number of samples for each angle is indicated in parenthesis in the first column. The devices share the same layout for the pads (i.e. the resonator is rotated with respect to the pads), hence only 2 values of the parasitic capacitance had to be extracted. From -10° to -30°, the Cf vaule is extracted to be 85 fF, from -40° to -60 ° and + 60 ° (given the LN in plane symmetry), Cf is 90fF.

(a) Main S0 mode, 10 finger devices of type A

Orientation to X axis(# of samples measured)	ELECTROMECHANICAL COUPLING k_t^2 (%)			QUALITY FACTOR Q			RESONANT FREQUENCY fs (MHz)
	max	min	aver	max	min	aver	aver
-60° (5)	9.1	4.22	7.04	289	234	297	724.1
-50° (2)	5.4	5.4	5.4	132	132	132	723.4
-40° (3)	6.12	1	4.37	845	122	462	724.7
-30° (2)	3.23	3.23	3.23	177	177	177	726.1
-20° (6)	4.43	2.63	3.53	253	253	253	731.7
-10° (5)	5.47	1.89	3.68	461	458	459	730.6
60° (2)	5.8	4.82	5.32	288	288	288	724.4

(b) Undertone of S0 mode, 10 finger devices of type A

Orientation to X axis(# of samples measured)	ELECTROMECHANICAL COUPLING k_t^2 (%)			QUALITY FACTOR Q			RESONANT FREQUENCY fs (MHz)
	max	min	aver	max	min	aver	aver
-30°(2)	2.53	1.77	2.15	1324	417	871	443.8
-20°(6)	6.3	2.02	4.16	353	127	240	465.1
-10°(5)	8.2	1.89	5.19	206	102	153	459

(c) Undertone of S0 mode, 10 finger devices of type B

Orientation to X axis(# of samples measured)	ELECTROMECHANICAL COUPLING k_t^2 (%)			QUALITY FACTOR Q			RESONANT FREQUENCY fs (MHz)
	max	min	aver	max	min	aver	aver
-30°(2)	3.82	1.64	2.73	615	356	486	513.5
-20°(3)	3.29	2.69	3.13	1305	425	757	510.7
-10°(3)	6.83	1.64	4.44	276	164	232	507.3

7.4.2 TCF from measurement

To determine the frequency-temperature characteristic of the LN/SiO₂ LVRs, the resonator response was monitored in the temperature range from 25 to 115 °C. The temperature was varied in 10 °C increments and a temperature stabilization step of 15 minutes was included before taking any measurement at each temperature. The devices were temperature cycled over the full temperature range, *i.e.* swept up and down to observe possible hysteresis as occasionally seen in AlN/SiO₂ resonators [68]. The relative frequency shift with temperature in both directions was verified to be the same. The S_{11} parameters of the resonators were measured three times at each 10 °C step and averaged before recording them.

As for the Y-cut ion-sliced LN thin film on SiO₂ LVRs, The resonant frequency from the measured resonator response was plotted with respect to temperature and fitted by linear regression to a first order equation to extract the device TCF (see Fig.7.9). The measured TCF for devices operating in the main S₀ mode around 720 MHz and in the undertone of S₀ mode around 450 MHz are reported in Table 7.3 for different orientations with respect to the x axis. For certain orientations to x axis, the TCF could not be accurately extracted because of the rather low Q (<200) exhibited by the device.

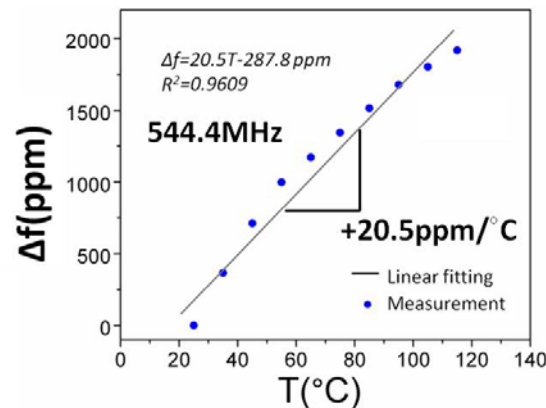


Fig.7.8. The relative frequency shift with temperature measured and fitted with linear regression technique for a resonator vibrating at 544.4 MHz. The 2nd order TCF of $-157.4 \text{ ppb}/^{\circ}\text{C}^2$ was extracted from 2nd order polynomial fitting. This value is the highest recorded for all tested devices. Most devices showed lower 2nd order TCF of about $1/4$ of the one measured for this device.

As shown in Table 7.3, the COMSOL modeled values of TCF matched the measured ones. The small differences ($\sim \pm 10\%$) are likely introduced by uncertainties in the simulation parameters and the exclusion of the electrode effects on TCF in the FEA. Different elastic, piezoelectric [59] [69] [70], and permittivity matrix coefficients [71] as well as temperature coefficients of stiffness [72] [58] have been reported for LN. The parameters listed in [15] were used in our analysis to ensure that all mechanical, electrical and thermal parameters would come from the same source. Additionally, the thermal characteristics of the thermally grown oxide layer are not known and equivalent bulk properties were used. Finally, although all resonators were fabricated on the same sample, the thickness of the films forming the resonator (AlSiCu, LN and SiO₂) was not uniform across the die. Uncertainties in film thicknesses influence the accuracy of the predicted TCFs.

Additionally, a plot of the TCF calculated from Eq. 10 for devices with and without 1600 nm of SiO₂ compensation is presented in Fig.7.10. For the orientation from -20° to -60° to x axis, the TCF from analytical calculations, COMSOL TCF FEA and experiments are compared (Fig.7.10 (b)). The value of the simulated and measured TCF for the main S0 mode displayed the same trend of the analytical results and suggested that minimum TCF for the S0 mode in a 420 nm Y-cut ion-sliced LN thin films on 1600 nm SiO₂ is obtained for an in plane counter clock wise (CCW or negative) rotation of 30° with respect to the x axis.

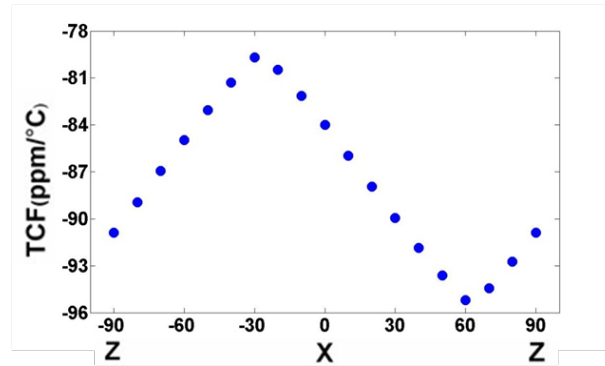
Table.7. 3. Comparison of TCF (ppm/°C) of LN/SiO₂ LVRs at various orientations. TCF of the main S0 mode and undertone are shown. TCF is directly measured and extracted from non-linear analysis. For the main S0 mode the TCF was also calculated by FEM in COMSOL.

(a) Undertone of S0 mode, 10 fingers devices of type A

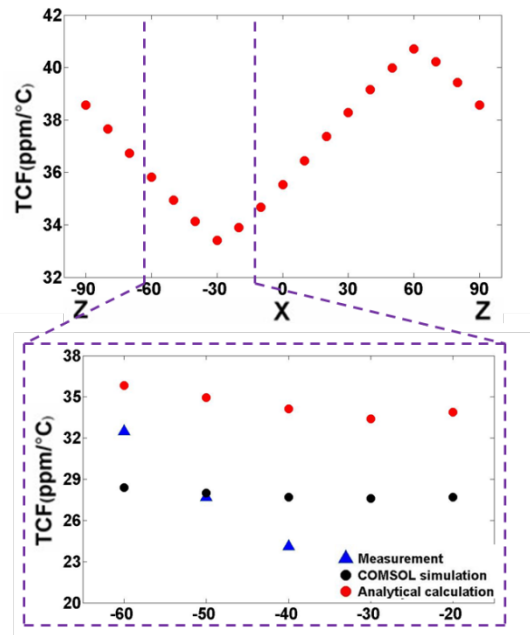
Orientation to X axis	TCF Direct Measurement	TCF Extracted from Non-Linear Analysis
20°	20.4	18.8
-10°	17	-
-20°	15.3	17.1
-30°	18	17.9
-40°	15.4	15.5

(b) Main S0 mode, 10 fingers devices of type A

Orientation to X axis	TCF Direct Measurement	TCF from COMSOL FEM
-20°	-	27.7
-30°	-	27.6
-40°	24.1	27
-50°	27.7	28
-60°	32.5	28.4



(a)



(b)

Fig.7.9. (a) Analytically calculated TCF dependency on orientations of main S_0 mode for Y-cut LN LVRs (b) Analytically calculated TCF dependency on orientations of main S_0 mode for LN/SiO₂ LVRs and zoomed in view for -20° to -60° to x axis. For these orientations the TCF from analytical calculation, COMSOL TCF FEA and experiments are plot for comparison. (Note that for certain orientations to x axis, the TCF could not be accurately extracted because of the rather low Q (<200) exhibited by the device.)

The X-cut ion-sliced LN thin film on SiO₂ LVRs were tested in the same manner in order to extract the device TCF (see Fig.7.11).

The measured TCF for devices operating in the main S0 mode around 510.47 MHz and 449.16 MHz orientated at $+30^\circ$ to the $+z$ axis and at -60° to the $+z$ axis respectively are $-3.9 \text{ ppm}/^\circ\text{C}$ and $-4.68 \text{ ppm}/^\circ\text{C}$, showcasing that it is possible to correctly temperature-compensate these devices. Moreover, the experimental results turn out to be in line with the simulation results shown in Fig.7.3. By setting LN(X-cut) and SiO_2 thicknesses to be 500 nm and 800 nm respectively, the large temperature coefficient of frequency exhibited by stand-alone LN devices is readily compensated to be around $-20 \text{ ppm}/^\circ\text{C} \pm 10 \text{ ppm}/^\circ\text{C}$ (since the $-20 \text{ ppm}/^\circ\text{C}$ is extracted from COMSOL FEA for X-cut LN LVR with 0° orientation to z -axis and analysis verified that the TCF has a slight dependence on orientation (few $\text{ppm}/^\circ\text{C}$)).

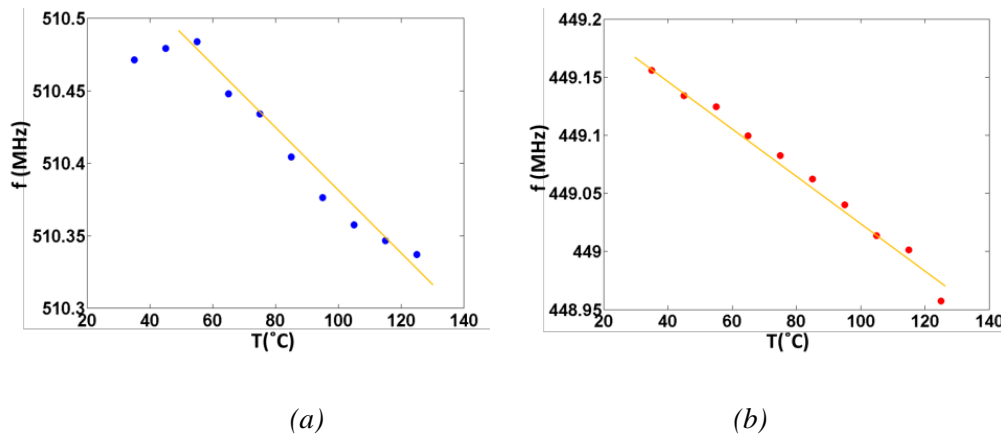


Fig.7.10. The frequency shift with temperature measured and fitted with linear regression technique for a) resonator vibrating at S0 mode of 510.47 MHz (80 μm aperture at $+30^\circ$ to the $+z$ axis of device types A1), b) resonator vibrating at at S0 mode of 449.16 MHz (80 μm aperture at -60° to the $+z$ axis of device types B3)

7.4.3 Non-linearity analysis and TCF extraction from non-linear model

The nonlinear behavior and power handling capability of the Y-cut LN on SiO_2 LVRs were experimentally investigated by measuring the admittance response at various input power levels. As previously demonstrated for AlN CMRs [73], we hypothesize that self-heating is the main source of non-linearity in this kind of laterally vibrating micromechanical resonators. Self-heating can be used to extract the device TCF by monitoring the shift of the resonance peak as a function of the applied input power.

Self-heating experiments [71] were conducted on the Y-cut LN/SiO₂ LVRs reported in this paper. The input power was swept from -10 to +10 dBm in increments of 2 dBm. A characteristic Amplitude-frequency (A-f) response evolution for a resonator oriented at 50° to +x axis is shown in Fig. 7.11. The nature of the nonlinearities, which shows bending of the resonator admittance peak towards higher frequencies (equivalent stiffening of the resonator), is a clear evidence of a positive TCF. This supports our hypothesis that self-heating is the source of non-linearity.

Applying the same analysis developed in [74] for AlN CMRs to Y-cut LN/SiO₂ LVRs, it is possible to model the thermal non-linearity in the resonator and use it to extract the resonator TCF.

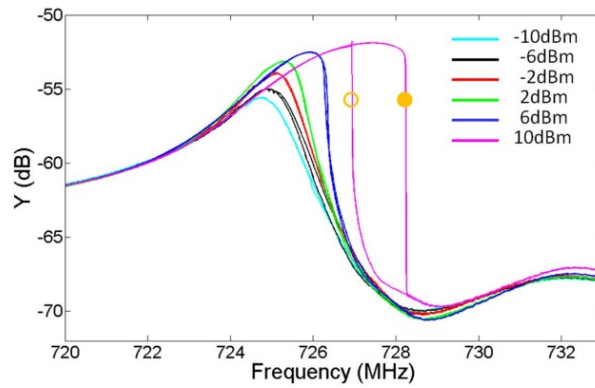


Fig.7.11. A-f curves of a 724.1MHz resonator. VNA forward and backward frequency sweep, 1601 points, IF BW = 1 kHz were performed for Prf from -10 to +10 dBm. For 10 dBm, the device exhibits hysteresis and the forward sweep is identified by the filled dotted curve whereas the backward sweep is indicated by the hollow dotted line.

Based on the model in [70], the resonator temperature is described by the following equation:

$$T = \frac{(R_m + R_s)\omega_0^2 q_{RMS}^2 L_t}{2 \sum \kappa_i T_{Ri} W_i} + T_{out} \quad (7.6)$$

where κ_i is the material stack thermal conductivity, and L_t , W_t , and T_{Ri} represent the geometrical dimensions of the anchors of the resonator (see Fig.7.12) through which the heat escapes. T_{out} refers to the reference temperature of the ambient environment, and T the effective temperature of the resonator undergoing vibration. q , is the charge flowing through the resonator, and ω is the input frequency. The effective TCF can then be derived as:

$$TCF = \frac{\Delta f}{T - T_{out}} = \frac{2\Delta f \sum \kappa_i T_{Ri} W_i}{(R_m + R_s)\omega_0^2 q_{RMS}^2 L_t} \quad (7.7)$$

where Δf is the relative frequency shift recorded experimentally.

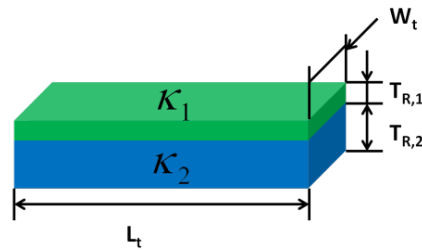


Fig.7.12. Geometrical dimensions of the anchors of the resonator

Using Eq. (7.4) and the geometrical parameters of the resonators and material properties from [71], [75] and [76], the TCF of Y-cut LN/SiO₂ LVRs was extracted from the self-heating measurements. For certain orientations to the x axis, the TCF could not be extracted from the self-heating measurements because of the rather low Q (<200) exhibited by these devices. Table 7.3 lists the extracted TCF values and compares them to the direct measurements and prediction from COMSOL FEA. The agreement between these data further confirms our hypothesis that self-heating is the source of non-linearity in these devices

8. Conclusions

8.1 Summary

This dissertation presented design, analysis, fabrication and experimental results for a new class of LN piezoelectric micromechanical resonators. These devices have their center frequency determined by the in-plane dimensions of the structure and are excited into vibrations mainly by the equivalent d_{11} piezoelectric coefficient. Because of this feature, they belong to the contour mode resonators family and they represent the only available class of micromechanical resonators that have been able to combine high k_t^2 , high Q in air, low motional resistance, low TCF after compensation and multiple frequencies on a single chip. Their performance sets the pathway for a new generation of reconfigurable communication systems.

LN technology platforms for RF MEMS based on LN/Si composite stack was selected and validated experimentally through trials and errors. Simultaneously, this selected platform resolve problems associated with parasitic capacitances present in the LN/SiO₂/Si sample stack used in the 1st generation devices and provide the potential to improve the fabrication accuracy and efficiency by adopting a new process flow based on LN/Si stack in 4" wafer scale. A scalable microfabrication process for LN microstructures was developed based on the selected platform at Carnegie Mellon University for the first time. This fabrication process involves direct bonding, selective etching and XeF₂ releasing. The process is low temperature (TMAX < 400 °C) and mainly uses standard CMOS-based fabrication steps, therefore offering the opportunity for synthesizing an RF transceiver heterogeneously integrated with CMOS electronics. This new fabrication process is compatible with stepper and demonstrates LN LVRs of high electromechanical coupling, high quality factors and reduced feedthrough capacitance between the input and output stages (15 fF vs. 150 fF for the LN on silicon through SiO₂).

In addition, efforts invested in improving the devices' performance in terms k_t^2 , Q and spurious mode suppression as well as robustness to process variation were presented. Active reflector design as well as electrode metal coverage optimization was developed to maximize the k_t^2 of LVRs based on X-cut

LN thin film. In order to enhance the Q , studies were conducted, to understand the energy loss mechanisms that affect the Q of the LVRs based on X-cut LN. Anchor loss analysis was guided by FEM and validated by experiments. The results showcase that significant Q enhancement can be achieved by properly sizing the gap region between the bus and the electrode edges. Besides, methods to suppress the spurious mode including 100% covered active reflector were introduced and verified to effectively help confining the energy into the main mode of resonance.

Last but not least, the temperature stability of the LN LVRs was studied and a method to reduce the device TCF by introducing SiO_2 in the device stack was demonstrated. This approach was shown to work with both Y and X-cut based devices. It was shown through modeling that low TCF devices operating at different frequencies can be built on the same substrate.

In summary this first prototypes of LVRs based on LN thin films hold great potentials for enabling a new wide bandwidth, reconfigurable and temperature stable RF filtering platform.

8.2 Future Research Directions

The research work presented in this dissertation has set the pathway for the development of a new class of vibrating microstructures that can perform multiple processing functions in the frequency domain by permitting the fabrication of different frequency resonators on the same silicon chip. Such devices hold great potentials for enabling a new wide bandwidth, reconfigurable and temperature stable RF filtering platform. A direct extension of this research consists in i) exploring the use of TFE LN resonators which will enable direct matching to $50\ \Omega$ and better control of spurious vibrations and ii) increasing the frequency of operation of the resonators beyond GHz, which would broaden the range of applications for these devices.

The author believes that this dissertation has generated, among many others, two main research paths to develop LN LVRs into systems: 1) a new wide bandwidth, reconfigurable and temperature stable

RF filtering platform performed by LN microstructures and 2) wireless resonant sensor/frequency reference platforms that can be operated with minimum energy consumption.

Appendix A: Lithium Niobate piezoelectric matrices of different in-plane-orientations and cuts MATLAB computation code

```

thita=-90;
pi=3.1415926;
thita=thita*pi/180;

%Z-cut compliancce matrix & piezoelectric matrix
C0=[1.9886e11 0.5467e11 0.6799e11 0.0783e11 0 0;0.5467e11 1.9886e11 0.6799e11
-0.0783e11 0 0;
    0.6799e11 0.6799e11 2.3418e11 0 0 0;0.0783e11 -0.0783e11 0 0.5986e11 0 0;
    0 0 0 0 0.5985e11 0.0783e11; 0 0 0 0 0.0783e11 0.7209e11];
e0=[0 0 0 0 3.83 -2.37;-2.37 2.37 0 3.83 0 0;0.23 0.23 1.80 0 0 0];

%Coordinates transformation matrix
%CW rotation along x axis, for y-cut rotation
a=[1 0 0;0 cos(thita) -sin(thita); 0 sin(thita) cos(thita)];

%Transformation matrix
M=[a(1,1)^2 a(1,2)^2 a(1,3)^2 2*a(1,2)*a(1,3) 2*a(1,3)*a(1,1)
2*a(1,1)*a(1,2);
    a(2,1)^2 a(2,2)^2 a(2,3)^2 2*a(2,2)*a(2,3) 2*a(2,3)*a(2,1)
2*a(2,1)*a(2,2);
    a(3,1)^2 a(3,2)^2 a(3,3)^2 2*a(3,2)*a(3,3) 2*a(3,3)*a(3,1)
2*a(3,1)*a(3,2);
    a(2,1)*a(3,1) a(2,2)*a(3,2) a(2,3)*a(3,3) a(2,2)*a(3,3)+a(2,3)*a(3,2)
a(2,1)*a(3,3)+a(2,3)*a(3,1) a(2,2)*a(3,1)+a(2,1)*a(3,2);
    a(3,1)*a(1,1) a(3,2)*a(1,2) a(3,3)*a(1,3) a(1,2)*a(3,3)+a(1,3)*a(3,2)
a(1,3)*a(3,1)+a(1,1)*a(3,3) a(1,1)*a(3,2)+a(1,2)*a(3,1);
    a(1,1)*a(2,1) a(1,2)*a(2,2) a(1,3)*a(2,3) a(1,2)*a(2,3)+a(1,3)*a(2,2)
a(1,3)*a(2,1)+a(1,1)*a(2,3) a(1,1)*a(2,2)+a(1,2)*a(2,1)];

Mt=transpose(M);
% If the z-cut matrix is ZX plane, then the corresponding Y-cut matrix(YX-
plane)
% should be
Cy=M*C0*Mt
ey=a*e0*Mt
%%%%%%%%%%%%%%%%%%%%%%%%%%%%%%%%%%%%%%%%%%%%%%%%%%%%%%%%%%%%%%%%%%%%%%%%
% To obtain y-cutX 128 degree matrix
thita=-127.86;
% thita=-120;

%positive sign for vector clock-wise rotation; negative sign for vector anti-
clockwise rotation

pi=3.1415926;
thita=thita*pi/180;

```

```

a=[cos(thita) 0 sin(thita); 0 1 0; -sin(thita) 0 cos(thita)];

%Transformation matrix
M=[a(1,1)^2 a(1,2)^2 a(1,3)^2 2*a(1,2)*a(1,3) 2*a(1,3)*a(1,1)
2*a(1,1)*a(1,2);
a(2,1)^2 a(2,2)^2 a(2,3)^2 2*a(2,2)*a(2,3) 2*a(2,3)*a(2,1)
2*a(2,1)*a(2,2);
a(3,1)^2 a(3,2)^2 a(3,3)^2 2*a(3,2)*a(3,3) 2*a(3,3)*a(3,1)
2*a(3,1)*a(3,2);
a(2,1)*a(3,1) a(2,2)*a(3,2) a(2,3)*a(3,3) a(2,2)*a(3,3)+a(2,3)*a(3,2)
a(2,1)*a(3,3)+a(2,3)*a(3,1) a(2,2)*a(3,1)+a(2,1)*a(3,2);
a(3,1)*a(1,1) a(3,2)*a(1,2) a(3,3)*a(1,3) a(1,2)*a(3,3)+a(1,3)*a(3,2)
a(1,3)*a(3,1)+a(1,1)*a(3,3) a(1,1)*a(3,2)+a(1,2)*a(3,1);
a(1,1)*a(2,1) a(1,2)*a(2,2) a(1,3)*a(2,3) a(1,2)*a(2,3)+a(1,3)*a(2,2)
a(1,3)*a(2,1)+a(1,1)*a(2,3) a(1,1)*a(2,2)+a(1,2)*a(2,1)];

Mt=transpose(M);
% If the z-cut matrix is ZX plane, then the corresponding Y-cut matrix(YX-
plane) should be
C=M*Cy*Mt
e=a*ey*Mt

%%%%%%%%%%%%%%%%%%%%%%%%%%%%%%%%%%%%%%%%%%%%%%%%%%%%%%%%%%%%%%%%%%%%%%%%
% To obtain y-cut 127.86 plane thita degree INPLANE rotation matrix
thita=90;
pi=3.1415926;
thita=thita*pi/180;

a=[cos(thita) -sin(thita) 0; sin(thita) cos(thita) 0; 0 0 1];

%Transformation matrix
M=[a(1,1)^2 a(1,2)^2 a(1,3)^2 2*a(1,2)*a(1,3) 2*a(1,3)*a(1,1)
2*a(1,1)*a(1,2);
a(2,1)^2 a(2,2)^2 a(2,3)^2 2*a(2,2)*a(2,3) 2*a(2,3)*a(2,1)
2*a(2,1)*a(2,2);
a(3,1)^2 a(3,2)^2 a(3,3)^2 2*a(3,2)*a(3,3) 2*a(3,3)*a(3,1)
2*a(3,1)*a(3,2);
a(2,1)*a(3,1) a(2,2)*a(3,2) a(2,3)*a(3,3) a(2,2)*a(3,3)+a(2,3)*a(3,2)
a(2,1)*a(3,3)+a(2,3)*a(3,1) a(2,2)*a(3,1)+a(2,1)*a(3,2);
a(3,1)*a(1,1) a(3,2)*a(1,2) a(3,3)*a(1,3) a(1,2)*a(3,3)+a(1,3)*a(3,2)
a(1,3)*a(3,1)+a(1,1)*a(3,3) a(1,1)*a(3,2)+a(1,2)*a(3,1);
a(1,1)*a(2,1) a(1,2)*a(2,2) a(1,3)*a(2,3) a(1,2)*a(2,3)+a(1,3)*a(2,2)
a(1,3)*a(2,1)+a(1,1)*a(2,3) a(1,1)*a(2,2)+a(1,2)*a(2,1)];

Mt=transpose(M);
% If the z-cut matrix is ZX plane, then the corresponding Y-cut matrix(YX-
plane) should be
Cr=M*C*Mt
er=a*e*Mt

```

Appendix B: Lithium Niobate laterally vibrating resonator

MATLAB fitting code

This appendix contains the MATLAB code that was used to fit the linear admittance response of the LN CMRs used in this thesis to the equivalent MBVD model. To eliminate the impact of the in-band spurious modes, which were found to be common for high f_r resonators, this code extracts both purely electrical and equivalent motional parameters by fitting the main resonance peak. Therefore, C_0 and R_0 are extracted from the out-of-band response and Q and $R_M + R_S$ are computed at resonance by means of the following equations:

$$C_0 = \text{mean}\left(\frac{\text{Im}(Y)}{\omega}\right); \quad R_0 = \text{mean}\left(\frac{1}{\text{Re}(Y)}\right); \quad Q = \frac{f_r}{2} \frac{\Delta \angle Y}{\Delta f} \bigg|_{f_r}; \quad R_M + R_S = \frac{1}{Y(f_r)} \quad \text{B.1}$$

where $\angle Y$, $\text{Re}(Y)$, and $\text{Im}(Y)$ represent the phase, real, and imaginary parts of the measured admittance. Then, R_S , which can be estimated through equation (5.5), is an input variable for our code, and the rest of characteristics parameters (k_t^2 , C_M , L_M) are computed from the previously extracted parameters by using equation (2.4-2.6).

```
clear all;
close all;
clc;

[f,dtot]=import_cti_ri('QC1R6_h.cti');
[f1,dt]= import_cti_ri('QC1R7_cph.cti');
% [f1,dt]= import_cti_ri('AR3C24_cph.cti');

w=2*pi*f;
f_MHz=f/1e6;
sample_size=length(f);

Y=(dtot-dt);
Z=1./Y;
% Z=1./Y-10;
```

```

% Y=1./Z-115e-15*j*w;

Ydb=20*log10(abs(Y));

[M_max_dB,Max_Index]=max(Ydb);

%plotting
figure;

plot(f_MHz,Ydb,'r')
xlim([f_MHz(1) f_MHz(end)]);
title('Resonance');
ylabel('Y (dB)');
xlabel('Frequency (MHz)');

hold on;

%Calculating C0
C01=mean(imag(Y(1:100))./w(1:100));
C02=mean(imag(Y(sample_size-100:sample_size))./w(sample_size-
100:sample_size));
C0=(C01*0+C02*10)/10
C0=70e-015;

%Calculating R0
R01=mean(1./real(Y(1:100)));
R02=mean(1./real(Y(sample_size-100:sample_size)));
R0=R02;
R0=150e3;

%Calculating R0p
R0p1=mean(real(1./(Y(1:100))));
R0p2=mean(real(1./(Y(sample_size-100:sample_size))));
R0p=R0p2;
R0p=300;

% Calculating fs and Rm
Zs=1./(Y-1/R0-(1./(1i*w*C0)+R0p).^-1);
Zs_imag=imag(Zs);
[zero_s,res_Index]=min(abs(imag(Zs)));
fs=f(res_Index);
fs=446.7e6;

Ys1=real(Y(res_Index));
Zp=1/Ys1; % R0 parallel Rm
Rm = Zp*R0./(R0-Zp);
Rm=220;
Rs=40;

%%%%%%%%%%%%%%%%%%%%%%%%%%%%%%%%%%%%%%%%%%%%%%%%%%%%%%%%%%%%%%%%%%%%%%%%

% Calculating fp
Zs_new=Zs-Rm;
Ys=1./Zs_new;

```

```

dummy2=res_Index;
Ys_imag=imag(Ys);
[zero_p,anti_res_Index]=min(abs(Ys_imag(dummy2:end)+w(dummy2:end)*C0));
fp=f(anti_res_Index+dummy2);
fp=458.3e6;

%frequencies in rads
ws=fs*2*pi;
wp=fp*2*pi;

[M_max_dB,Max_Index]=max(Ydb);
[M_min_dB,Min_Index_dummy]=min(Ydb(Max_Index:end));
Min_Index=Min_Index_dummy+Max_Index-1;
display_gap=(M_max_dB-M_min_dB)*0.14;
Ymax=Ydb(Max_Index);

%calculating R0,Rs,Cm,Lm,Rm...

r=((fp/fs)^2-1)^(-1);

Cm=(C0)/r;

% Cm=1.36e-015;

Lmt=(Cm*ws^2)^(-1);

Qm=(1/Rm)*(sqrt(Lmt/Cm));

%calculating kt^2

ktsq=pi^2/8*(Cm)/C0;

%plotting
figure;
subplot(2,1,1);
plot(f_MHz,Ydb,'r');
xlim([f_MHz(1) f_MHz(end)]);
title('Frequency Response');
xlabel('Frequency (MHz)');
ylabel('Y (dB)');

Yeq=(1./(Rm+j*w*Lmt-j./(w*Cm)))+(1./(j*w*C0)+R0p).^(-1)+(1./R0);

%%% Introduce Rs: subtract the guessed value of Rs from the previously
%%% fitted Rm

Q_load=(1/(Rm+Rs)).*(sqrt(Lmt./Cm));

Zeq=1./Yeq+Rs

Yeq=1./Zeq;

Yeq_db=20*log10(abs(Yeq));

```

```

hold on;

plot(f_MHz,20*log10(abs(Yeq)), 'b');

text(f_MHz(1)+(f_MHz(end)-f_MHz(1))*0.03,Ymax-0.5*display_gap, strcat('f_s=',
num2str(fs*1e-6), ' MHz'));
text(f_MHz(1)+(f_MHz(end)-f_MHz(1))*0.03,Ymax-2.0*display_gap, strcat('Q_m=',
num2str(round(Qm))));
text(f_MHz(1)+(f_MHz(end)-f_MHz(1))*0.03,Ymax-
3.5*display_gap, strcat('k_t^2=', num2str(ktsq*100), '%'));
text(f_MHz(1)+(f_MHz(end)-f_MHz(1))*0.03,Ymax-5.0*display_gap, strcat('R_0p=',
num2str(round(R0p)), ' \Omega'));
text(f_MHz(1)+(f_MHz(end)-f_MHz(1))*0.03,Ymax-6.5*display_gap, strcat('C_0=',
num2str(C0*1e15), ' fF'));
text(f_MHz(end)-(f_MHz(end)-f_MHz(1))*0.25,Ymax-
0.5*display_gap, strcat('k_t^2*Q=', num2str(ktsq*Qm)));
text(f_MHz(end)-(f_MHz(end)-f_MHz(1))*0.25,Ymax-
2.0*display_gap, strcat('R_s=', num2str(Rs), ' \Omega'));
text(f_MHz(end)-(f_MHz(end)-f_MHz(1))*0.25,Ymax-
3.5*display_gap, strcat('R_m=', num2str(round(Rm)), ' \Omega'));
text(f_MHz(end)-(f_MHz(end)-f_MHz(1))*0.25,Ymax-
5.0*display_gap, strcat('L_m=', num2str(Lmt), ' \Omega'));
text(f_MHz(end)-(f_MHz(end)-f_MHz(1))*0.25,Ymax-
6.5*display_gap, strcat('C_m=', num2str(Cm), ' \Omega'));
hold off;

subplot(2,1,2);
plot(f_MHz,angle(Y)*180/pi, 'r');
xlim([f_MHz(1) f_MHz(end)]);
xlabel('Frequency (MHz)');
ylabel('Y (\circ)');
hold on;
plot(f_MHz,angle(Yeq)*180/pi, 'b');
hold off;
%legend('Measured Response','Fitting Curve','Location','SouthWest');

Lmt
Cm
C0
%Af=0.5MHz
f_MHz(res_Index)
res_Index1=res_Index-32;
res_Index2=res_Index+32;
f1_MHz=f_MHz(res_Index1)
Z(res_Index1)
f2_MHz=f_MHz(res_Index2)
Z(res_Index2)
(f2_MHz-f1_MHz)*1e6

```

Appendix C: Lithium Niobate Laterally Vibrating Resonator

Fabrication Process

This appendix provides with a detailed description of the process steps and recipes followed to fabricate LFE LN LVRs on a Lithium Niobate substrate at the Carnegie Mellon Nanofabrication facilities. Moreover, some additional characterization procedures and complementary measurements are included in order to help with fabrication. In particular, the process flow described here corresponds to a 3-mask manufacturing process whose schematic representation was shown in figure 3.8.

WAFER ID

1. TOP ELECTRODE

- a. WASH WAFER (ACETONE, IPA, DI WATER)
- b. DRY WAFER (SPIN RISE DRIER)
- c. HMDS DEPOSITION (VAPOR PRIME OVEN)

HMDS RECIPE	3
-------------	---
- d. PHOTORESIST DEPOSITION (SPINNER)

PHOTORESIST	AZ 4110
SPINNER RECIPE	3000 rpm, 30 sec
BAKE TIME (90 °C)	20 min
- e. LITHOGRAPHY (STEPPER) - MASK TOP ELECTRODE

EXPOSURE TIME	235 μ sec
FOCUS OFFSET	+0.75
- f. PHOTORESIST DEVELOPMENT

DEVELOPER	AZ DEVELOPER
BEAKER WIDTH (SMALL, LARGE)	SMALL
DEVELOPER VOLUME	80 ml
WATER VOLUME	40 ml

DEVELOPMENT TIME 2 min

- g. INSPECTION OF LITHOGRAPHY (OLYMPUS MICROSCOPE)
DEVELOPMENT (UNDER, OK, OVER)

ADDITIONAL DEVELOPMENT TIME (min)

SAVED IMAGE FILE

- h. INSPECTION OF LITHOGRAPHY (TENCOR PROFILOMETER)

EXPECTED PHOTORESIST THICKNESS 1.1 μm

ACTUAL PHOTORESIST THICKNESS

DIFFERENCE (%)

- i. METAL DEPOSITION (CVC SPUTTERER)

RUN NUMBER

RECIPE lsCrAlSiCu100nm

METALS Cr, AlSiCu

EXPECTED THICKNESSES 10,100 nm

DEPOSITION TIMES 100, 270 sec

DEPOSITION POWERS 100, 250 W

- j. METAL PATTERNING (LIFT-OFF)

SONICATOR TIME (MIN) 5

SOAK TIME (HOURS) 12

- k. VISUAL INSPECTION OF METAL FEATURES (OLYMPUS MICROSCOPE)

CLEAN METAL LINES? (YES OR NO)

ADDITIONAL LIFT-OFF TIME (MIN)

SAVED IMAGE FILE

- l. METAL THICKNESS MEASUREMENT (PROFILOMETER)

CENTER (nm)

EDGE (nm)

UNIFORMITY (%)

m. METAL RESISTIVITY MEASUREMENTS (DC PROBES)

4 LINES (Ω)

8 LINES (Ω)

12 LINES (Ω)

16 LINES (Ω)

20 LINES (Ω)

RESISTIVITY (n Ω m)

n. RESERVED FOR ADDITIONAL INFORMATION

2. SECOND METAL ELECTRODE

a. WASH WAFER (ACETONE, IPA, DI WATER)

b. DRY WAFER (SPIN RISE DRIER)

c. HMDS DEPOSITION (VAPOR PRIME OVEN)

HMDS RECIPE 3

d. PHOTORESIST DEPOSITION (SPINNER)

PHOTORESIST AZ 4110

SPINNER RECIPE 3000 rpm, 30 sec

BAKE TIME (90 °C) 20 min

e. LITHOGRAPHY (STEPPER) - MASK SECOND ELECTRODE

EXPOSURE TIME 235 μ sec

FOCUS OFFSET +0.75

f. PHOTORESIST DEVELOPMENT

DEVELOPER AZ DEVELOPER

BEAKER WIDTH (SMALL, LARGE) SMALL

DEVELOPER VOLUME 80 ml

WATER VOLUME 40 ml

DEVELOPMENT TIME 2 min

g. INSPECTION OF LITHOGRAPHY (OLYMPUS MICROSCOPE)

DEVELOPMENT (UNDER, OK, OVER)

ADDITIONAL DEVELOPMENT TIME (min)

SAVED IMAGE FILE

h. INSPECTION OF LITHOGRAPHY (TENCOR PROFILOMETER)

EXPECTED PHOTORESIST THICKNESS 1.1 μm

ACTUAL PHOTORESIST THICKNESS

DIFFERENCE (%)

i. METAL DEPOSITION (6J SPUTTERER)

INITIAL CHAMBER PRESSURE $<10^{-6}$ T

METALS Au

EXPECTED THICKNESSES 100 nm

DEPOSITION TIMES 240 sec

DEPOSITION POWERS 50 W

BLEED PRESSURE 20 mT

Ar FLOW RATE 65 sccm

j. METAL PATTERNING (LIFT-OFF)

SONICATOR TIME (MIN) 5

SOAK TIME (HOURS) 12

k. VISUAL INSPECTION OF METAL FEATURES (OLYMPUS MICROSCOPE)

CLEAN METAL LINES? (YES OR NO)

ADDITIONAL LIFT-OFF TIME (MIN)

SAVED IMAGE FILE

l. METAL THICKNESS MEASUREMENT (PROFILOMETER)

CENTER (nm)

EDGE (nm)

UNIFORMITY (%)

m. METAL RESISTIVITY MEASUREMENTS (DC PROBES)

4 LINES (Ω)

8 LINES (Ω)

12 LINES (Ω)

16 LINES (Ω)

20 LINES (Ω)

RESISTIVITY ($n\Omega m$)

n. RESERVED FOR ADDITIONAL INFORMATION

3. ALUMINA DEPOSITION

a. WASH WAFER (ACETONE, IPA, DI WATER)

b. DRY WAFER (SPIN RISE DRIER)

c. ALUMINA DEPOSITION (ALD)

DEPOSITION RECIPE ALUMINA_NOTSTABILIZE_150°C

EXPECTED THICKNESSES 30 nm

NUMBER OF CYCLES 300

DEPOSITION TEMPERATURE 150 °C

d. ADDITIONAL INFORMATION COOLING OF ALD PALLETTE FOR 1 HOUR BEFORE
AND AFTER LOADING/UNLOADING SAMPLE

4. LN ETCH

a. WASH WAFER (ACETONE, IPA, DI WATER)

b. DRY WAFER (SPIN RISE DRIER)

c. SiO₂ DEPOSITION (PECVD)

DEPOSITION RECIPE LS_SiO₂_DEP

EXPECTED THICKNESSES 1.6 μm

DEPOSITION TIMES 1100 sec

- DEPOSITION TEMPERATURE 375 °C
- d. METAL DEPOSITION (CVC SPUTTERER)
- RUN NUMBER
- RECIPE LsAlSiCu300nm
- METALS AlSiCu
- EXPECTED THICKNESSES 300 nm
- DEPOSITION TIMES 810 sec
- DEPOSITION POWERS 250 W
- e. PHOTORESIST DEPOSITION (SPINNER)
- PHOTORESIST AZ 4620
- SPINNER RECIPE 3000 rpm, 30 sec
- BAKE TIME (100 °C) 45 MIN
- f. LITHOGRAPHY (STEPPER) - MASK LN ETCH
- EXPOSURE TIME 440 μ sec
- FOCUS OFFSET +0.75
- MARK SHIFT X +0.1 μ m
- MARK SHIFT Y -0.2 μ m
- g. PHOTORESIST DEVELOPMENT
- DEVELOPER AZ DEVELOPER
- BEAKER WIDTH (SMALL, SMALL
LARGE)
- DEVELOPER VOLUME 80 ml
- WATER VOLUME 40 ml
- DEVELOPMENT TIME 2 min
- h. INSPECTION OF LITHOGRAPHY (OLYMPUS MICROSCOPE)
- VERNIER (# OF LINES FROM CENTER)
- MISALIGNMENT (# OF LINES X 0.2 μ m)

UP OR DOWN (NEGATIVE OR POSITIVE)

DEVELOPMENT (UNDER, OK, OVER)

ADDITIONAL DEVELOPMENT TIME (min)

SAVED IMAGE FILE

i. INSPECTION OF LITHOGRAPHY (TENCOR PROFILOMETER)

EXPECTED PHOTORESIST THICKNESS (μm)	5.5
-------------------------------------	-----

ACTUAL PHOTORESIST THICKNESS (μm)

DIFFERENCE (%)

j. SiO₂ ETCHING (RIE)

RUN NUMBER

RECIPE JAZFC

TIME 60 MIN

k. REMOVAL OF PHOTORESIST FROM EDGES AND BACK OF WAFER

1. PERMISSION FROM STAFF TO USE WAFER WITH VERSALINE ETCHER

m. LN ETCHING (PLASMATHERM VERSALINE ETCHER)

RUN NUMBER

RECIPE LN_OXIDEMASK_3

TIME 10 MIN

CHECK He PRESSURE ABOVE 3800 Torr

n. RESERVED FOR ADDITIONAL INFORMATION

5. RELEASE

a. RELEASE WAFER (VHF ETCHER)

RECIPE # 5

NUMBER OF CYCLES 1

- b. INSPECTION (WENTWORTH PROBE STATION)
FEATURES APPEAR RELEASED?
- c. RESERVED FOR ADDITIONAL INFORMATION

REFERENCES:

-
- [1] G. Piazza, P. Stephanou, and A. Pisano, "Piezoelectric aluminum nitride vibrating Contour-Mode MEMS resonators," *J. Microelectromech. Syst.*, vol. 15, no. 6, pp. 1406–1418, Dec. 2006.
 - [2] C.-M. Lin, T.-T. Yen, V. V. Felmetger, M. A. Hopcroft, J. H. Kuypers, and A. P. Pisano, "Thermal compensation for aluminum nitride Lamb wave resonators operating at high temperature," in *Proc. IEEE IFCS*, 2010, pp.14–18.
 - [3] M. Rinaldi, A. Tazzoli, J. Segovia-Fernandez, V. Felmetger, and G. Piazza, "High power and low temperature coefficient of frequency oscillator based on a fully anchored and oxide compensated AlN contour-mode MEMS resonator," in *IEEE 25th Int. MEMS Conf*, pp. 696–699, Feb. 2012.
 - [4] C. Zuo, N. Sinha, J. Van der Spiegel, G. Piazza, "Multi-Frequency Pierce Oscillators Based On Piezoelectric AlN Contour-Mode MEMS Technology", *Journal of MicroElectroMechanical Systems*, vol. 19, no. 3, pp. 570-580, Jun 2010.
 - [5] S. Gong, L. Shi, and G. Piazza, "High electromechanical coupling resonators using ion sliced X-cut LiNbO₃ thin film," *MTT-S*, June, 2012, pp. 1-3.
 - [6] R. T. Smith and F. S. Welsh, "Temperature dependence of the elastic, piezoelectric, and dielectric constants of lithium tantalate and lithium niobate," *Journal of Applied Physics*, vol. 42, no. 6, pp. 2219–2230, May 1971.
 - [7] K.K. Wong, properties of Lithium Niobate, INSPEC, The Institution of Electrical Engineers, London, United Kingdom, 2002
 - [8] J. Bjurstrom, G. Wingqvist, V. Yantchev, and I. Katardjiev, "Temperature compensation of liquid FBAR sensors," *J. Micromech. Microeng.*, vol. 17, pp. 651–658, Mar. 2007.
 - [9] P. Rabiei and P. Gunter, "Sub-micron thin films of lithium niobate single crystals prepared by crystal ion slicing and wafer bonding", 2000 Optical Society of America
 - [10] K.M. Lakin, G.R. Kline and K.T. McCarron, "Thin Film Bulk Acoustic Filters for GPS", *Lnterasonics Symp. Proc.*, pp. 471-476, 1992.
 - [11] K. Hashimoto, "RF Bulk Acoustic Wave Filters for Communications", Artech House, 2009.
 - [12] J.J. Campbell, W.R. Jones "A method for estimating optimal crystal cuts and propagation directions for excitation of piezoelectric surface waves" *IEEE Transactions on Sonics and Ultrasonics*, vol. su-15, no. 4, Oct. 1968
 - [13] I. Kuznetsova, B. Zaitsev, S. Joshi, and I. Borodina, "Investigation of acoustic waves in thin plates of lithium niobate and lithium tantalate," *IEEE Trans. Ultrason., Ferroelect., Freq. Control*, vol. 48, no. 1, pp. 322–328, Jan. 2001.
 - [14] G. H. Hewig, K. Jain, F. O. Sequeda R. Tom and P. Wang "R.F. Sputtering of LiNbO₃ Thin Films" *Thin Solid Films*, 88 (1982) 67-74
 - [15] H. Akazawa and M. Shimada, "Correlation between interfacial structure and c-axis-orientation of LiNbO₃ films grown on Si and SiO₂ by electron cyclotron resonance plasma sputtering," *Journal of Crystal Growth*, vol. 270, no. 34, pp. 560–567, 2004.
 - [16] S. Tan, T. Gilbert, C. a. Hung, T. E. Schlesinger, and M. Migliuolo, "Sputter deposited c-oriented LiNbO₃ thin films on SiO₂," *Journal of Applied Physics*, vol. 79, no. 7, pp. 3548–3553, Apr 1996
 - [17] M. Kadota, T. Ogami, K. Yamamoto, Y. Negoro, and H. Tochishita "High Frequency Lamb Wave Device composed of LiNbO₃ Thin Film" *Proc. IEEE Ultrasonics Symposium* (2008)
 - [18] R. A. Betts and C. W. Pitt, "Growth of thin-film Lithium niobate by molecular beam epitaxy" *Electronics Letters* 10th October 1985 Vol. 21
 - [19] D. Saulys, V. Joshkin, M. Khoudiakov, T. Kuech, A. Ellis, S. Oktyabrsky, and L. McCaughan, "An examination of the surface decomposition chemistry of lithium niobate precursors under high vacuum conditions," *Journal of Crystal Growth*, vol. 217, no. 3, pp. 287–301, 2000Y.

-
- [20] Shibata, K. Kaya, K. Akashi, M. Kanai, T. Kawai, and S. Kawai, "Epitaxial growth and surface acoustic wave properties of lithium niobate films grown by pulsed laser deposition" *Applied Physics* 77 (4), 15 February 1995
 - [21] J.-G. Yoon and K. Kim, "Growth of highly textured LiNbO₃ thin film on Si with MgO buffer layer through the sol-gel process" *Applied Physics Letters* 68 (18), 29 April 1996
 - [22] L. Arizmendi, "Photonic applications of lithium niobate crystals," *physica status solidi (a)*, vol. 201, no. 2, pp. 253–283, 2004
 - [23] Y.B. Park, Bumki Min, Kerry J. Vahala, H. A. Atwater, "Integration of Single-Crystal LiNbO₃ Thin Film on Silicon by Laser Irradiation and Ion Implantation-Induced Layer Transfer" *Advanced Material* 2006, 18, 1533–1536.
 - [24] M. Levy, R. M. Osgood, R. Liu, L. E. Cross, G. S. Cargill, A. Kumar, and H. Bakhru, "Fabrication of single-crystal lithium niobate films by crystal ion slicing," *Applied Physics Letters*, vol. 73, no. 16, pp. 2293
 - [25] B. E. Deal, M. Sklar, A. S. Grove, and E. H. Snow. 1967. Characteristics of the surface-state charge (Q_{ss}) of thermally oxidized silicon. *Journal of the Electrochemical Society* 114, 3, 266–274.
 - [26] L. Shi "Methods for Micromachining of Lithium Niobate for the Synthesis of Suspended High Electromechanical Coupling Resonators", master thesis, University of Pennsylvania
 - [27] R. Wang, S. Bhawe, and K. Bhattacharjee, "Thin-film high k_t²Q, multi-frequency lithium niobate resonators," *IEEE MEMS* 2013, January 20-24, 2013, pp. 165-168.
 - [28] L. Shi and G. Piazza, "Ion-sliced Lithium Niobate on silicon dioxide for engineering the temperature coefficient of frequency of Laterally Vibrating Resonators", *Joint European Frequency and Time Forum & International Frequency Control Symposium (EFTF/IFC)*, 2013, p. 417-420.
 - [29] R. Ruby, P. Bradley, I. Larson, J., Y. Oshmyansky, and D. Figueredo, "Ultra-miniature high-Q filters and duplexers using FBAR technology," in *Solid-State Circuits Conference*, 2001. *Digest of Technical Papers. ISSCC. 2001 IEEE International*, pp. 120-121, 438, 2001.
 - [30] Kimura, T.; Kadota, M.; Ida, Y.; "High Q SAW resonator using upper-electrodes on grooved-electrodes in LiTaO₃" *2010 IEEE MTT-S International*, vol., no., pp.1740-1743, 23-28 May 2010.
 - [31] G. Piazza, P.J. Stephanou, and A.P. Pisano, "One and two port piezoelectric higher order contour-mode MEMS resonators for mechanical signal processing", *Solid-State Electronics*, 51(11), p. 1596-1608, 2007.
 - [32] M. Weinberg¹, R. Candler, S. Chandorkar, J. Varsanik, T. Kenny, A. Duwell, "Energy Loss in MEMS Resonators and the on Inertial and RF Devices", in *Proc. IEEE Transducers*, June 2009, pp 688-695.
 - [33] G. D. Cole, I. Wilson-Rae, K. Werbach, M. R. Vanner, and M. Aspelmeyer, "Phonon-tunnelling dissipation in mechanical resonators," *Nat. Commun.*, vol. 2, p. 231, Mar. 2011.
 - [34] J. A. Judge, D. M. Photiadis, J. F. Vignola, B. H. Houston, and J. Jarzynski, "Attachment loss of micromechanical and nanomechanical resonators in the limits of thick and thin support structures," *J. Appl. Phys.*, vol. 101, no. 1, p. 013521, Jan. 2007.
 - [35] Z. Hao, A. Erbil, and F. Ayazi, "An analytical model for support loss in micromachined beam resonators with in-plane flexural vibrations," *Sens. Actuators Phys.*, vol. 109, no. 1–2, pp. 156–164, Dec. 2003.
 - [36] J. Segovia, and G. Piazza, "Damping in 1 Ghz laterally-vibrating composite piezoelectric resonators" *IEEE MEMS* 2015, January 18-22
 - [37] A. Frangi, M. Cremonesi, A. Jaakkola, T. Puensala, "On the optimization of piezoelectrically actuated MEMS resonator", in *Proc. IEEE Ultrasonics*. Oct. 2012, pp 1043-1046.
 - [38] A. B. Pippard, "Ultrasonic attenuation in metals" *Phil. Mag.*, 1955, vol. 46, pp 1104 -1114.
 - [39] A.R. Huston and D.L. White. , "Elastic wave propagation in piezoelectric semiconductors" *J. Appl. Phys.* 1962, vol. 33 ,pp.40
 - [40] C. Zuniga, M. Rinaldi and G. Piazza, "Reduced viscous damping in High Frequency Piezoelectric Resonant Nanochannels for Sensing in Fluids", in *Proc. IEEE MEMS*, Jan. 2011, pp. 960-963

-
- [41] A. Akheiser. "On the Absorption of Sound in Solids," J.Phys. USSR, 1 1939, pp. 277.
 - [42] A.V. Granato, K. Lücke, "Application of dislocation theory to internal friction phenomena at high frequencies", J. Appl. Phys., 27, 1956, pp. 583
 - [43] K. Hashimoto, RF Bulk Acoustic Wave Filters for Communications. Artech House, 2009.
 - [44] C.-M. Lin, V. Yantchev, J. Zou, Y.-Y. Chen, and A. P. Pisano, "Micromachined One-Port Aluminum Nitride Lamb Wave Resonators Utilizing the Lowest-Order Symmetric Mode," J. Microelectromechanical Syst., vol. 23, no. 1, pp. 78–91, Feb. 2014.
 - [45] K. M. Lakin, "Electrode Resistance Effects in Interdigital Transducers," IEEE Trans. Microw. Theory Tech., vol. 22, no. 4, pp. 418–424, Apr. 1974.
 - [46] COMSOL Multiphysics Reference Manual
 - [47] C. Cassella, S. Navab, B. W. Soon, and G. Piazza, "Quality factor dependence on the inactive regions in AlN contour-mode resonators," Journal of Microelectromechanical Systems, to be published, 2015.
 - [48] L. Wu, M. Akgul, Z. Ren, Y. Lin, W.-C. Li, and C. T.-C. Nguyen, "Hollow stems for higher micromechanical disk resonator quality factor", in Proc. IEEE Intl. Ultrason. Symp., Orlando, FL, Oct. 2011, pp. 1964–1967.
 - [49] W. Pang, H. Zhang, S. Whangbo, and E.S. Kim, "High Q film bulk acoustic resonator from 2.4 to 5.1 GHz," in Proc. IEEE Int. Conf. Micro Electro Mech. Syst., Maastricht, Netherlands, Jan. 2004, pp. 805–808.
 - [50] B. P. Harrington and R. Abdolvand, "In-plane acoustic reflectors for reducing effective anchor loss in lateral-extensional MEMS resonators," J. Micromech. Microeng., vol. 21, 085021, Aug. 2011.
 - [51] C. Cassella, J. S. Fernandez, M. Cremonesi, A. Frangi, and G. Piazza, "Reduction of anchor losses by etched slots in aluminum nitride contour mode resonators," in Proc. Eur. Freq. Time Forum & IEEE Int. Freq. Contr. Symp., Prague, Czech, 2013, pp. 926–929.
 - [52] H. Zhang, J. Liang, X. Zhou, H. Zhang, D. Zhang, and W. Pang "Transverse Mode Spurious Resonance Suppression in Lamb Wave MEMS Resonators: Theory, Modeling, and Experiment" IEEE Transactions on electron devices, vol. 62, no. 9, Sept. 2015
 - [53] C.-M. Lin, J.-C. Hsu, D. G. Senesky, and A. P. Pisano, "Anchor loss reduction in AlN Lamb wave resonators using phononic crystal strip tethers", in Proc. IEEE Int. Freq. Contr. Symp., Taipei, Taiwan, 2014, pp. 371–375.
 - [54] Y. Song and S. Gong, "Elimination of spurious modes in SH0 Lithium Niobate laterally vibrating resonators," IEEE Electron Devices Letter, vol.36, no.11, pp.1198-1201, Nov. 2015
 - [55] B. Drafts, "Acoustic wave technology sensors," IEEE Trans. Microw. Theory Tech., vol. 49, pp. 795–802, Apr. 2001.
 - [56] S. Gong, and G. Piazza, "Design and Analysis of Lithium Niobate based High Electromechanical Coupling RF-MEMS Resonators for Wideband Filtering," Microwave Theory and Techniques, IEEE Transaction on, vol. 61, no.1, pp.403-414, Jan. 2013.
 - [57] C.-M. Lin, T.-T. Yen, V. V. Felmetzger, M. A. Hopcroft, J. H. Kuypers, and A. P. Pisano, "Thermal compensation for aluminum nitride Lamb wave resonators operating at high temperature," in Proc. IEEE IFCS, 2010, pp.14–18.
 - [58] S.Ohta, K. Nakamura, A.Do, and Y. Ishida, "Temperature characteristics of solidly mounted piezoelectric thin film resonators," in Proc. IEEE Int. Ultrasonics Symp., 2003, pp. 2011–2015.
 - [59] J. Bjurstrom, G. Wingqvist, V. Yantchev, and I. Katardjiev, "Temperature compensation of liquid FBAR sensors," J. Micromech. Microeng., vol. 17, pp. 651–658, Mar. 2007
 - [60] H. Yu, W. Pang, H. Zhang, and E. S. Kim, "Ultra temperature stable bulk- acoustic-wave resonators with SiO2 compensation layer," IEEE Trans. Ultrason. Ferroelectr. Freq. Control, vol. 54, pp.2102–2109, Oct. 2007.
 - [61] W. Pang, R. C. Ruby, R. Parker, P. W. Fisher, M. A. Unkrich, and J. D. Larson III, "A temperature-stable film bulk acoustic wave oscillator," IEEE Electron Device Lett., vol. 29, pp. 315–318, Apr.2008.

-
- [62] R. Melamud, B. Kim, S. A. Chandorkar, M. A. Hopcroft, M. Agarwal, C. M. Jha, and T. W. Kenny, "Temperature-compensated high-stability silicon resonators," *Appl. Phys. Lett.*, vol. 90, art. no. 244107, Jun. 2007.
 - [63] P.J. Stephanou, G. Piazza, C.D. White, M.B.J. Wijesundara, A.P. Pisano "Piezoelectric aluminum nitride MEMS annular dual contour mode filter," *Sens. Actuators A* 134:152–160, June 2007.
 - [64] J. H. Kuypers, C.-M. Lin, G. Vigevari, and A. P. Pisano, "Intrinsic temperature compensation of aluminum nitride Lamb wave resonators for multiple-frequency references," in *Proc. IEEE Intl. Freq. Control Symp.*, 2008, pp. 240–249.
 - [65] R. T. Smith and F. S. Welsh, "Temperature dependence of the elastic, piezoelectric, and dielectric constants of lithium tantalate and lithium niobate," *Journal of Applied Physics*, vol. 42, no. 6, pp. 2219–2230, May 1971.
 - [66] B. A. Auld, *Acoustic Fields and Waves in Solids*. Krieger Publishing Company, 1990
 - [67] C.-M. Lin, T.-T. Yen, Y.-J. Lai, V. V. Felmetzger, M. A. Hopcroft, J. H. Kuypers, and A. P. Pisano, "Temperature-compensated aluminum nitride Lamb wave resonators," *IEEE Trans. Ultrason. Ferroelectr. Freq. Control*, vol. 57, pp. 524–532, Mar. 2010
 - [68] G. Wingqvist, L. Arapan, V. Yantchev, and I. Katardjiev, "A micromachined thermally compensated thin film Lamb wave resonator for frequency control and sensing applications," *J. Micromech. Microeng.*, vol. 19, art. no. 035018, Mar. 2009.
 - [69] R.S. Weis and T.K. Gaylord "Lithium Niobate: summary of the physical properties and crystal structure" *Applied Physics*. A37, 191-203 1985
 - [70] G. Kovacs, M. Anhorn, H. Engan, G. Visintini, and C. Ruppel, "Improved material constants for LiNbO₃ and LiTaO₃," in *Ultrasonics Symposium, 1990. Proceedings., IEEE 1990*, Dec 1990, pp. 435–438
 - [71] T. Yamaha, N. Niizeki, H. Toyoda "Piezoelectric and elastic properties of Lithium Niobate single crystals" *Japanese Journal of Applied Physics*, vol 6, no. 2, Feb., 1967
 - [72] P. Nicolay, O. Elmazria, B. Assouar, F. Sarry, and L. Lebrizoul, "Theoretical and experimental study of the differential thermal expansion effect on the TCD of layered SAW temperature sensors," in *Proc. IEEE Intl. Ultrason. Symp.*, 2007, pp. 272–275.
 - [73] A. Tazzoli, M. Rinaldi, and G. Piazza, "Experimental Investigation of Thermally Induced Nonlinearities in Aluminum Nitride Contour-Mode MEMS Resonators", *IEEE Electron Device Letters*, vol. 33, no. 5, May 2012.
 - [74] Segovia-Fernandez, J.; Piazza, G., "Thermal Nonlinearities in Contour Mode AlN Resonators," *J. Microelectromechanical Systems*, vol. no. 99, pp. 1, 1, 0 doi:10.1109/JMEMS.2013.225242
 - [75] T. Yamane, N. Nagai, S.-I. Katayama, and M. Todoki, "Measurement of thermal conductivity of silicon dioxide thin films using a 3 ω method," *J. Applied Phys.*, vol. 91, pp. 9772–9776, 2002.
 - [76] Parker, et al., "Flash Method of Determining Thermal Diffusivity, Heat Capacity, and Thermal Conductivity," *Journal of Applied Physics*, Vol. 32, 1961, pp. 1679